Formation and Detachment of Leading Edge Vortices on Unsteady Airfoils

Vom Fachbereich Maschinenbau
an der Technischen Universität Darmstadt
zur
Erlangung des Grades eines Doktor-Ingenieurs (Dr.-Ing.)
genehmigte

D i s s e r t a t i o n

vorgelegt von

Dipl.-Ing. Alexander Guido Martin Widmann

aus Frankfurt am Main

Berichterstatter:	Prof. Dr.-Ing. C. Tropea
Mitberichterstatter:	Prof. Dr.-Ing. L. David
Tag der Einreichung:	15.04.2015
Tag der mündlichen Prüfung:	15.07.2015

Darmstadt 2015, D17

Abstract

The unsteady velocity field around a pitching and plunging airfoil has been investigated whereby two different mechanisms leading to the detachment of leading edge vortices, which form at the suction side of the airfoil during a motion cycle, were of central interest. One of these mechanisms is analogous to the classical vortex shedding mechanisms behind bluff bodies. The second mechanism is independent of any geometrical length and occurs as a result of the viscous/inviscid interaction between the leading edge vortex and the boundary layer on the airfoil. The mass transferred from the shear layer at the leading edge for one motion period was hypothesized to determine, which detachment mechanism limits LEV growth. A non-dimensional parameter κ, describing the covering ratio of the LEV and the airfoil chord, has been introduced to predict for which flow parameters a detachment between both mechanism occurs. A decomposition of κ yields a dependency on the Reynolds number, the reduced frequency and the shear layer parameters.
Time-resolved particle image velocimetry was used to obtain two-dimensional velocity fields and direct force measurements were performed. The flow fields were analyzed be means of vortex identification methods, topological arguments and the finite time Lyapunov-exponent. The results show, that the commonly used set of non-dimensional parameters is not sufficient to completely describe the vortex detachment behavior, since it neglects the shear layer properties. Instead, the conducted experiments reveal, that the leading edge shape determining the shear layer curvature has a recognizable impact an the lift and the circulation created by an unsteady profile. It was found, that a critical chord length exists, above which the bluff body detachment mechanism is replaced by a mechanisms related to viscous/inviscid interactions between secondary flow structures and the shear layer. The formation these secondary structures is found to be limited to a low Reynolds-number regime. While at low reduced frequencies, the airfoil chord length is characteristic for LEV detachment, the airfoil kinematics determine the instant of LEV detachment at higher reduced frequencies. The results show, that the LEV detachment behavior is much more complex than previously assumed. Its dependency might be reduced to the chord as a characteristic parameter in the typical flight regime with moderate reduced frequencies and sufficiently high Reynolds numbers, but involves many more parameters if the airfoil kinematics leave this typical

Abstract

flight regime.

Kurzzusammenfassung

Die instationären Geschwindigkeitsfelder um ein aerodynamisches Profil in Hub- und Nickbwegegung wurden im Hinblick auf das Ablöseverhalten der Vorderkantenwirbel untersucht, die sich wärend eines Bewegungszyklus auf der Saugseite bilden. Dabei wurden zwei unterschiedliche Ablösemechanismen unterschieden, wobei sich der erste Mechanismus analog zur bekannten Wirbelablösung hinter stumpfen Körpern verhält. Der zweite Mechanismus ist das Resultat einer viskos/inviskosen Interaktion zwischen dem Vorderkantenwirbel und der Grenzschicht auf der Oberfläche des Profils und ist damit unabhänig von einer charakteristischen geometrischen Länge. Als bestimmend dafür, welcher Mechanismus zuerst greift, wurde die Menge Fluid angenommen, die während eines Bewegungsperiode des aerodynamischen Profils von der Scherschicht in den Vorderkantenwirbel gespeist wird. Ein dimensionsloser Parameter κ wird eingeführt, der das Bedeckungsverhältnis der Profilsehne mit dem Vorderkantenwirbel beschreibt und vorhersagt, unter welchen Bedingungen eine Transition zwischen beiden Mechanismen eintritt. Eine Zerlegung von κ offenbart seine direkte Abhängigkeit von der reduzierten Frequenz, der Reynolds-Zahl und den Scherschichteigenschaften.
Zweidimensionale zeitaufgelöste Geschwindigkeitsfelder wurden mit Hilfe von Particle Image Velocimetry aufgenommen und direkte Kraftmessungen durchgeführt. Die Auswertung der Geschwindigkeitsfelder wurde anhand von Wirbelidenfikationsschemata, Strömungstopologie und der Berechnung des finite time Lyapunov-Exponenten vorgenommen. Die Ergebnisse zeigen, dass die im Allgemeinen genutzte Gruppe entdimensionierter Parameter nicht ausreicht, um das Wirbelablöseverhalten vollständig zu beschreiben, weil die Scherschichteigenschaften unberücksichtigt bleiben. Die Experimente lassen allerdings erkennen, dass die Scherschichtkrümmung, die von der Vorderkantenform bestimmt wird, einen messbaren Einfluss auf den Auftrieb und die Zirkulation hat, die von einem instationären Profil erzeugt werden. Es zeigte sich, dass eine kritische Sehnenlänge existiert, oberhalb derer der aus der Wirbelablösung stumpfer Körper bekannte Mechanismus mit dem viskos/inviskosen Mechanismus ersetzt wird. Dieser beruht auf der Bildung sekundärer Wirbelstrukturen, die sich nahe der Vorderkante bilden und mit der Scherschicht interagieren. Die Bildung dieser Strukturen ist auf den Bereich kleiner Reynolds-Zahlen beschränkt. Während bei kleinen reduzierten Frequenzen die Sehnenlänge des Prfoils noch charakter-

istisch für das Ablöseverhalten ist, bestimmt die Kinematik des Profils den Zeitpunkt der Wirbelablösung bei hohen reduzierten Frequenzen. Daraus lässt sich schliessen, dass das Ablöseverhalten eines Vorderkantenwirbels komplexer ist als bisher angenommen. Im Parameterbereich des typischen Schlagflugs (mit vergleichsweise hohen Reynolds-Zahlen und moderaten reduzierten Frequenzen) kann zwar die Sehnenlänge als problemcharakteristisch gelten, mit zunehmenden Abweichungen der Parameter von diesem Flugzustand treten mehr Einflussfaktoren auf.

Acknowledgements

This project was kindly supported by the Deutsche Forschungsgesellschaft (DFG).

Above all, I would like to express my gratitude for my advisor Professor Dr.-Ing. Cameron Tropea. The great amount of trust during all my work and the freedom and time to development some ideas is not something to be taken for granted. During the years as his assistant I had the opportunity to learn a lot and improve my scientific skills by far. I often was surprised by the confidence, with which he assigned me the seemingly most difficult tasks. His reliance in my abilities exceeded mine by far and gave me the opportunity to develop my self-confidence and sense of responsibility.
I am also very grateful to thank Prof. Dr.-Ing. Laurent David from the University of Poitiers for his immediate readiness to co-referee my thesis. His field of work fits perfectly and I am glad to learn something from his great expertise.
I also want thank all the distinguished people, who kindly accompanied me over the last years and gave me valuable feedback and ideas. During the discussions, Dr. David Rival and Dr. Jochen Kriegseis taught me great deal and shared their knowledge. Dr. Jacques Boree gave me valuable hints suggested new analysis methods I did not even think of. I also want to thank Dr. Holger Babinsky and Dr. Michael Ol for the opportunity to participate in the RTO AVT-202 research group and witness their stunning expertise. Additionally, I am obliged to Dr.-Ing. Sven Grundmann, who always had an open ear for my problems and provided the most valuable advice. Dr. Hubert Marschall really helped me to understand the foundations of flow topology and provided support concerning all kinds of theoretical questions. The discussions with him were enlightening. Dipl. Math. M. Sc. Imdat Maden showed an enormous amount of patience and granted huge support in order to implement my ideas into the numerical simulations. I thank Dr. Ahmed Naguib for many constructive suggestions, especially for helping me put my scattered thoughts in a proper order. Smooth, swift and uncomplicated administrative processes and support were ensured by Petra Fuhrmann, Stephanie Lath and Birgit Neuthe. Thanks to them I was able to concentrate on my project.
Dipl.-Ing. Matthias Quade helped me without any complaints with all kinds of IT problems, especially a reliable triggering is a product of his inventiveness. All experimental research depends on the mechanical realiza-

tion, therefore I want to thank the whole work shop under the supervision of Ilona Kaufhold. Their readiness to help even on short term and their hard and diligent work contributed immensely to the overall success.
I am also grateful for the contributions of the following students to the re-design of the wind tunnel or the experimental rig, the data analysis, the measurements or the numerics: Abdelmonem Bousbia, Oussama Choucair, Daniel Freudenhammer and Martin Zimmer, Niels Göran Blume, Helge Eichhorn, Jens Hambach, Felix Loosmann, Tobias Ritter, Maximilian Schäffner, Manuel Wilhelm, Felix Fischer, Pascal Schaub, Lian Liu (University of Toronto), Jan Tracht, Philipp Rosendahl, Julian Gesche, Martin Behnsch and Dennis Kütemeier. I learned a lot by their diligence and curiosity.
I would have not been able to finish this project without the support of my great colleagues in Griesheim. They always had a helping hand or provided support and distraction in difficult times. Among them are: Dr. Alexander Duchmann, Dr. Lars Opfer, Dr. Andreas Reeh, Dr. Thomas Bachmann, Armin Kurz, Florian Wassermann, Martin Bruschewski, Daniel Freudenhammer and Bernhard Simon. Moreover, I want to thank Ulrike Cordes for accompanying me to Lampertheim. I am also obliged towards our laser, who found it in his heart to last long enough for my measurements without breaking.
Finally, I need to express my gratitude for my parents, who supported me all these years. But above all, I want to thank my wife Anna and my son Oskar for their love during the most exciting period of my life.

Contents

List of Figures

List of Tables

Nomenclature

Latin letters

Symbol	Unit	Description
a_0	$\frac{1}{m}$	shear layer curvature
A	m^2	vortex area
c	m	chord length
c_M	$[-]$	sectional moment coefficient, $\frac{2M}{\rho U_\infty^2 c^2}$
c_N	$[-]$	sectional normal force coefficient, $\frac{2N}{\rho U_\infty^2 c}$
C	$[-]$	vortex generator constant
d	m	airfoil thickness
D	m	diameter
f	$\frac{1}{s}$	frequency
f	$[-]$	non-dimensional factor
F	N	force
g	$\frac{m}{s^2}$	gravity acceleration
g	$[-]$	genus of a topological domain
Δh	m	plunge amplitude
$h(t/T)$	m	plunging position
$\dot{h}$	$\frac{m}{s}$	plunging velocity
h_{WT}	m	wind-tunnel height
i	$[-]$	Poincare-Bendixon index of a critical point
I	$\frac{kgm}{s}$	impulse
I	$[-]$	imaginary part
J	$[\frac{kgm^2}{s^2}]$	energy
k	$[-]$	number of problem related units
k	$[-]$	reduced frequency
k	$\frac{m}{s^2}$	volume force
k^*	$[-]$	fractional vortex convection rate
l	m	length scale
L	m	piston stroke length
$\dot{m}$	$\frac{kg}{s}$	mass flow
M	Nm	sectional aerodynamic moment
n	$[-]$	number of physical parameters

N	N	sectional normal force
N	$[-]$	nodal point
N	$[-]$	number of samples
r	m	vortex radius
R	$[-]$	real part
Re	$[-]$	Reynolds number
S	m^2	integration area
S	$[-]$	saddle point
S	$\frac{1}{s}$	symmetric vorticity tensor
S'	$[-]$	half-saddle point
St	$[-]$	Strouhal number
t	s	time
T	s	airfoil motion period
T^*	$[-]$	vortex formation time, $\frac{L}{D}$
Tu	$[-]$	turbulence level
U_∞	$\frac{m}{s}$	free stream velocity
$U_\perp$	$\frac{m}{s}$	velocity perpendicular to the airfoil
U_p	$\frac{m}{s}$	piston velocity
U	$\frac{m}{s}$	streamwise velocity
V	$\frac{m}{s}$	normal velocity
W	$\frac{m}{s}$	spanwise velocity
x	m	streamwise direction
y	m	normal direction
z	m	spanwise direction
X_{SP}	m	chordwise position of LEV reattachment point

Greek letters

Symbol	Unit	Description
$\alpha_{eff}(t/T)$	$^\circ$	effective angle of attack
$\alpha_{geo}(t/T)$	$^\circ$	geometrical angle of attack
$\alpha_{plunge}(t/T)$	$^\circ$	angle of attack caused by plunging motion
Γ_1	$[-]$	vortex identification scalar
Γ_2	$[-]$	galilean invariant vortex identification scalar
Γ	$\frac{m^2}{s}$	circulation
Γ^{LEV}	$\frac{m^2}{s}$	leading edge vortex circulation
$\Gamma^{Eruption}$	$\frac{m^2}{s}$	secondary vortex circulation
Γ^{TEV}	$\frac{m^2}{s}$	trailing edge vortex circulation
Γ^-	$\frac{m^2}{s}$	clockwise circulation in all vortical structures
δ_{SL}	m	shear layer thickness
Δ	$[-]$	difference
η	$\frac{kg}{ms}$	dynamic viscosity
Θ	$^\circ$	geometrical leading edge angle
κ	$[-]$	vortex / airfoil covering ratio
λ	$[-]$	eigenvalue
λ	m	wave length
λ^*	$\frac{kg}{ms}$	first Lame constant
ν	$\frac{m^2}{s}$	kinematic visocity
π	$[-]$	circle constant
ρ	$\frac{kg}{m^3}$	fluid density
σ	$[-]$	finite time Lyapunov exponent
σ	$[-]$	standard deviation
χ	$[-]$	Euler-characteristic of a topological flow domain
ω	$\frac{1}{s}$	vorticity
Ω	$\frac{1}{s}$	antisymmetric vorticity tensor

Subscripts

Symbol	Description
$1, 2, 3...$	running index
$1, 1$	upstream / downstream linear actuator
acq	acquisition
$char$	characteristic
$crit$	critical
i	individual sample
max	maximal
min	minimal
$shed$	vortex shedding
$trans$	transitional value
$vort$	vortical
WT	wind tunnel

Superscripts

Symbol	Description
$-$	clockwise vorticity
$+$	counter-clockwise vorticity

Abbreviations

Symbol	Description
CTA	constant temperature anemometer
DBD	dielectric barrier discharge actuator
$DEHS$	Di-Ethyl-Hexyl-Sebacat
FOV	field of view
$FTLE$	finite time Lyapunov exponent
IA	interrogation area
LDA	laser-Doppler anemometry
LEV	leading edge vortex
MAV	micro air vehicle
$Nd:YLF$	neodymium-doped yttrium lithium fluoride
PBI	Poincare-Bendixon index
PIV	particle image velocimetry

1 Introduction

Today the fundamentals steady aerodynamics are well-known and for most applications well understood. A younger branch of research deals with unsteady aerodynamic phenomena, which in contrast are not fully understood. One example of unsteady phenomena can be observed in the flow around an airfoil, when it experiences a sudden change in angle of attack. Typical examples are the flapping wings of an insect, a bird, a Micro Air Vehicle (MAV) or revolving blades as found in helicopters or wind turbines. According to Ol *et al.* (2009) the appearance of the vortical flow features causes deviations from the well-known static lift curve and a lift hysteresis develops over a flapping cycle of the wing. These effects are caused by the so-called dynamic stall phenomenon and have been described by McCroskey (1982). Dynamic stall is accompanied, according to Leishman (2008), by the formation and shedding of vortices, which exhibit a large impact of the flow behavior and the force history. Polhamus (1966), (1971) shows that these vortices produce a region of low-pressure on the suction side of a wing and exert a strong suction force as long as they grow over the wing section and are attached to the wing (a similar effect in the form of a suction region at the leading edge of a steady airfoil is described by Katz and Plotkin (1991)). During its growth phase a vortex executes a strong force on a wing, its detachment leads, according to Jones and Babinsky (2010), to a sudden drop in the instantaneous forces. The growth and evolution of leading edge vortices (LEVs) are thereby of primary interest in the field of unsteady aerodynamics. According to Sarkar and Venkatraman (2008) these vortices originate from a flow separation near the leading edge, which grows due to unsteady flow conditions and subsequently evolves into a distinct vortex.
The effects described above may occur in diverse fields of application, especially in flapping flight aerodynamics: In insect flight, in the advancing miniaturization of Micro Air vehicles (MAVs), in the flow around helicopter blades and in the operation of (rotary) wind turbines or flapping energy harvesting devices. In all of these devices the wake is dominated by

shedding vortices. According to Young *et al.* (2014) these fields may be subdivided into two groups. The first group comprises energy harvesting devices, which extract energy by decreasing the net impulse of the oncoming flow. In this case the wake is similar to the well-known von Karman type, the shed vortices arrange themselves in a manner such that a dent develops in the averaged wake velocity profile. The second group are the lift or thrust producing devices, which expend energy into the oncoming flow to propel themselves. According to Platzer *et al.* (2001) this can be achieved by reversing the von Karman vortex street and altering the wake velocity profile in such a way that a net jet forms behind the unsteady airfoil. Anderson *et al.* (1998) attribute this formation of a reversed von Karman vortex street to the formation and shedding time of LEVs: Increases in efficiency and force production are attributed to the formation and interaction of LEVs and trailing edge vortices (TEVs).
The relevance of the development and detachment of vortices for the above mentioned fields of application are briefly described below:

- Flapping flight: At low flight velocities the performance of steady airfoils is low, as explained by Lissaman (1983). Shyy *et al.* (2010) show that the performance of flapping flyers at low flight velocities is superior to fixed wing flyers, which can be attributed to the formation of LEVs which tend to form especially at low flight velocities when the boundary layer is prone to flow separation. Dickinson and Götz (1993), Ellington *et al.* (1996) or Platzer *et al.* (2008) show how these mechanisms are used by insects to fly efficiently or to generate high lift coefficients. The importance of LEVs during insect flight maneuvers was recognized by Ellington *et al.* (1996) and demonstrated by Rival *et al.* (2011), Azuma and Watanabe (1988) or Maybury and Lehmann (2004). Tayor *et al.* (2003) and Nudds *et al.* (2004) demonstrate that the efficiency of flapping flight depends strongly on the wing non-dimensional heaving amplitude. They show that for a wide variety of flapping flyers this non-dimensional heaving amplitude is concentrated in a narrow dimensionless band. In that respect the manipulation of the growth and shedding time of the LEVs is crucial. Rival *et al.* (2008) demonstrate in that context how the LEV circulation may be manipulated by changing the airfoil kinematics. Prangemeier *et al.* (2010) show how the occurrence of a trailing edge

vortex (TEV) may be suppressed by a quick pitching motion during the end of the downstroke in order to prevent a loss in lift.

- Micro Air Vehicles: As the miniaturization of MAVs progress and their flight speeds decrease, fixed wing configurations are according to Shyy *et al.* (2008), not apt to attain the necessary lift. Their efficiency needs to be increased in order to carry larger and heavier energy storage devices, which are necessary for an increased net loading and flight duration. Therefore new concepts similar to insect flight with flapping or rotating wings utilizing unsteady effects, have to be applied. For a useful manipulation of the vortex in technical devices, a precise knowledge about the vortex behavior is needed.

- Flapping energy harvesting devices: In classical wind energy harvesting devices the flow around the blades should remain attached, if they should work at high efficiency levels. In contrast to that flapping flight energy harvesting devices try to exploit the above mentioned unsteady effects (which make animal locomotion so efficient) by means of a pitching and plunging airfoil. These devices are especially efficient for low Reynolds number applications. The energy extraction in this kind of device relies on the typical flutter mechanisms in two-degrees of freedom (pitching and plunging motion) aero-elastic wing system, as explained by Young *et al.* (2014). The phasing between pitching and plunging motion determines the form of the wake and therefore determines whether energy is extracted from the flow or thrust is generated. The feathering limit according to Kinsey and Dumas (2008) determines the boundary between the two operation modes in terms of pitching and plunging phase shift. The further a flapping energy harvesting device operates in the energy extraction region, the larger the effective angle of attack becomes. The flow then tends to separate and form LEVs, which dominate the flow. It has been shown by Young *et al.* (2014) that the development of an LEV is a requirement for high power extraction and efficiency, because it induces a region of low pressure on the airfoils suction side. The pitch angle determines the direction, in which the large suction force points and therefore determines the airfoil's operation mode. The interplay

of pitch angle and LEV evolution state are then therefore crucial for efficient power generation.

- Delta wings: At the leading edges of delta wings vortex sheets roll up at a large angle of attack and form vortices. Due to their rotational motion these vortices are accompanied by a low pressure region on the suction side of the delta wing. This suction force has a large contribution to the overall lift as explained by Maltby (1968) or Gursul (2012). If these vortices can be stabilized, higher lift values can be achieved. Gursul *et al.* (2005) give a number of examples, how LEVs over a delta wing may be manipulated in order to increase their stability; among them are suction and blowing of air or plasma actuators. Such flow manipulation requires a precise knowledge about the mechanisms, which limit the growth of the LEVs or lead to their detachment. The techniques mentioned indicate by which means LEVs in flapping flight may be manipulated.

While LEV formation has favorable effects at low air speeds concerning efficiency or lift augmentation in the above mentioned examples, and are sought to be utilized technically, they may be detrimental or disadvantageous for the examples listed below. LEVs may cause vibrations in wings or blades, deteriorate incoming flow conditions, cause noise or unwanted peak loads.

- Wind turbines: Unsteady effects like gusts can alter the oncoming flow conditions of wind turbine blades, changing the effective angle of attack. For increased angles of attack these effects may cause the flow to separate from the blade surface and form vortices, which results in load peaks. The flow separation deteriorates the wind turbine performance and the load peaks cause large instantaneous root bending moments of the turbine blades, which promote fatigue, ultimately leading to failure of the wind turbine. A decambering mechanism of the turbine blade can reduce these peak loads and homogenize the extracted power and increase the life time of a wind turbine. For the design of such an active or passive decambering mechanism the knowledge about the vortex development and the prediction of the unsteady load is crucial. Load prediction models by Larsen *et al.* (2007) for example, typically rely on empirical data and do not take

the physical mechanisms determining the LEV formation and detachment into account.

- Helicopter blades: What distinguishes helicopter rotor blades and wind turbines from flapping flyers or energy harvesting devices is their comparatively high flow velocities, which hinders separation of the flow from the airfoil surface. Due to the rapid changes in the effective angle of attack unsteady effects, including the formation of vortices, can be observed; typical examples are given in the book by Leishman (2008). Although the additional gain in the lift force attributed to the LEV formation is advantageous, problems arise when these vortices detach from the wings and move into the blade wake. This detachment is accompanied by a sudden drop in the lift force and fluctuations in the drag. Vibrations are introduced into the rotor blades and the detached vortices interact with the following blades. For the design of helicopter rotors the knowledge of the aerodynamic loading is crucial. The formation and detachment of vortices complicate the estimation and prediction of the aerodynamic load. According to Leishman (2008) empirical and semi-empirical models have been developed to predict the blades load. The most popular among them is the Leishman-Beddoes model, described by Leishman and Beddoes (1989). Usually these models are based on determining certain coefficients from global blade or rotor measurements rather than on physical mechanisms. In addition, the noise emitted from helicopters can be attributed to the periodic formation and detachment of vortices.

These examples show the impact of vortex dynamics on technical systems under unsteady aerodynamic conditions. The relevant range of Reynolds numbers in which unsteady effects have a strong impact on the aerodynamics reaches from very low Reynolds numbers ($Re \approx 10^3$ for insects and MAVs) to high Reynolds numbers ($Re \approx 10^6$ for helicopters). Of special interest in all cases is the prediction of the maximal size of the developing vortices in terms of their maximal achievable circulation, the prediction of their growth rate and the prediction of their detachment timing. Crucial for such a prediction is the knowledge about the physical mechanisms responsible for the growth and detachment under different aerodynamic conditions. Such knowledge about the physical mechanisms is the requirement

for the manipulation of vortices to prolong their growth and enhance their maximal achievable circulation in order to increase the instantaneous aerodynamic forces and the development of improved models for the unsteady wing load prediction. The aims of this thesis can therefore be summarized as follows:

- Obtain a better understanding of the physical mechanisms limiting LEV size and circulation
- Identify the mechanisms leading to LEV detachment
- Find the characteristic parameters for these mechanisms
- Identify the influence of isolated parameters on LEV formation
- Develop methods for the manipulation or prolongation of the growth of LEVs, if the detachment mechanisms are sufficiently understood

2 Background

This chapter provides background information and details of previous studies on the subject of leading edge vortices. The phenomenon of dynamic stall is briefly explained, the non-dimensional numbers facilitating experimental similarity are introduced and the concept of optimal vortex formation is explained. The concept of flow topology is introduced in order to better understand the fluid mechanical processes, which lead to the formation and detachment of vortices. A short overview of the vortex detachment mechanisms in the literature and their characteristic parameters is given. Based on these mechanisms hypotheses concerning the underlying fluid dynamics are formulated and possible methods for the manipulation of LEVs are given.

2.1 Non-dimensional numbers for unsteady aerodynamics

To transfer the unsteady aerodynamic phenomena from the examples of application given in chapter 1 into a laboratory frame, usually a combined pitching and plunging motion is imposed on the airfoil in order to realize the temporally varying boundary conditions, which represent the unsteady flow conditions. The physical parameters governing unsteady aerodynamics are the incoming flow velocity U_∞, the density ρ and dynamic viscosity η of the fluid, the chord length of the moving airfoil c, the plunge height of the wing h, and the wing beat frequency f with a corresponding stroke period of $T = \frac{1}{f}$. According to the Buckingham-Pi-Theorem (1914) a number of p non-dimensional parameters can be constructed from a number of n physical parameters with a number of k units: $p = n - k$.
For the present case $n = 6$ and $k = 3$ and three non-dimensional parameters are sufficient to describe the flow around an unsteady airfoil. The most common choice of these parameters are the Reynolds number Re based

on the airfoil chord, the Strouhal number St and the reduced frequency k for given airfoil kinematics. The Reynolds number $Re = \frac{cU_\infty}{\nu}$ (with $\nu = \frac{\eta}{\rho}$) represents the ratio of inertial to viscous forces acting on the flow around the wing. The Strouhal number $St = \frac{2f\Delta h}{U_\infty} = \frac{2\Delta h}{TU_\infty}$ represents the ratio of the convectively covered distance by the incoming flow during one stroke period TU_∞ and the airfoil plunging height $2h$ normal to the incoming flow. The reduced frequency $k = \frac{\pi fc}{U_\infty} = \frac{\pi c}{TU_\infty}$ represents the convectively covered distance by the incoming flow during one stroke period TU_∞ and the aligned airfoil chord c. The non-dimensional numbers for a typical airfoil in combined pitching and plunging are visualized in figure 2.1. $\dot{h}(t/T)$ indicates the plunging velocity of the airfoil, $\alpha_{geo}(t/T)$ the geometrical angle of attack, α_{plunge} the angle of attack induced by the lateral velocity $\dot{h}(t/T)$, and $\alpha_{eff}(t/T) = \alpha_{geo}(t/T) + \alpha_{plunge}(t/T)$ the effective angle of attack.

The material properties of air for the determination of the non-dimensional numbers are taken from Kothandaramn and Subramanyan (2007). The fourth parameter governing the aerodynamic behavior of an airfoil is the history of the effective angle of attack $\alpha_{eff}(t)$. The airfoil experiences an angle of incidence of the oncoming flow if the oncoming velocity vector shows a tilt with respect to the airfoil chord. A change in the effective angle of attack can therefore be achieved by pitching the airfoil about a fixed point or creating a velocity component perpendicular to the airfoil's chord by a plunging motion of the airfoil. With increasing angle of attack the LEV development and the aerodynamic hysteresis effects are pronounced according to Leishman (1990).
According to Baik *et al.* (2012) the Strouhal number predominantly determines the aerodynamic forces produced during a stroke cycle and according to Triantafyllou *et al.* (2004) St determines the efficiency, while k according to Baik *et al.* (2012) determines the maximal size of the LEVs and the global flow topology and represents the unsteadiness of the flow according to McCroskey (1982).
Because these three parameters are defined by the chord length and the plunging height, they are only suitable for capturing physical mechanisms of the same scale, therefore they can only represent the global flow topology and not necessary viscous flow effects arising at disparent scales.

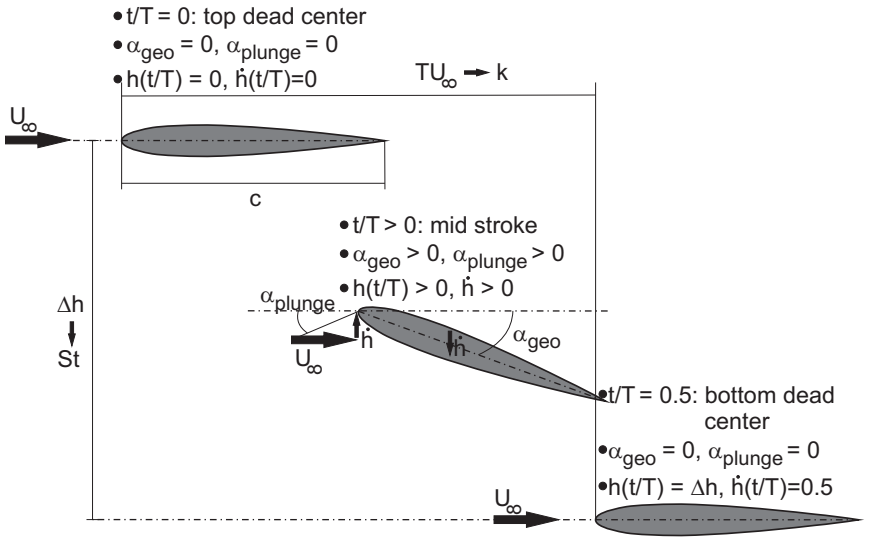

Figure 2.1: Combined pitching and plunging airfoil motion with the dimensional parameters chord length c, free stream velocity U_∞, plunging height Δh, plunging velocity $\dot{h}$ and motion period T and the non-dimensional numbers Reynolds number Re, reduced frequency k, Strouhal number St and angle of attack history α_{eff} representing the motion cycle

2.2 Dynamic stall and its impact on the force history

Dynamic stall occurs, if during the downstroke of an unsteady airfoil the incoming flow exceeds a certain angle of attack. The oncoming flow experiences almost instantaneously a rising pressure gradient over the airfoil with a change of the effective angle of attack, because the global flow field adjusts to the varied flow conditions with the speed of sound. Because the boundary layer flow at the airfoil surface is dominated by viscous effects, it reacts much slower to the changes imposed by the oncoming flow (Cebeci *et al.* (2004)), which causes the flow to separate from the airfoil's surface and forms a separation bubble. With an increasing effective

angle of attack this bubble grows further and develops into a vortex, as described by Sarkar and Venkatraman (2008). Between the temporal lag of instantaneous changes in global flow field and the delayed boundary-layer reaction, the instantaneous lift can be augmented well beyond steady lift. This augmentation can be maintained until the near-wall flow adjusts to the altered flow conditions. This development manifests itself as a growing leading edge vortex as reported by Rival and Tropea (2010) or Read *et al.* (2003). As soon as the LEV growth stops and the LEV detaches from the airfoil surface, a strong drop in lift can be observed. The flow over the whole airfoil is separated, the airfoil is stalled. The phenomena of LEV growth and subsequent detachment become apparent in a distortion of the distinct lift curve for steady airfoils into a strong hysteresis. Figure 2.2 (taken from Carr *et al.* (1988)) schematically shows the lift curve of an unsteady airfoil for a complete stroke cycle. The correlation between the stage in vortex formation and instantaneous lift is emphasized.

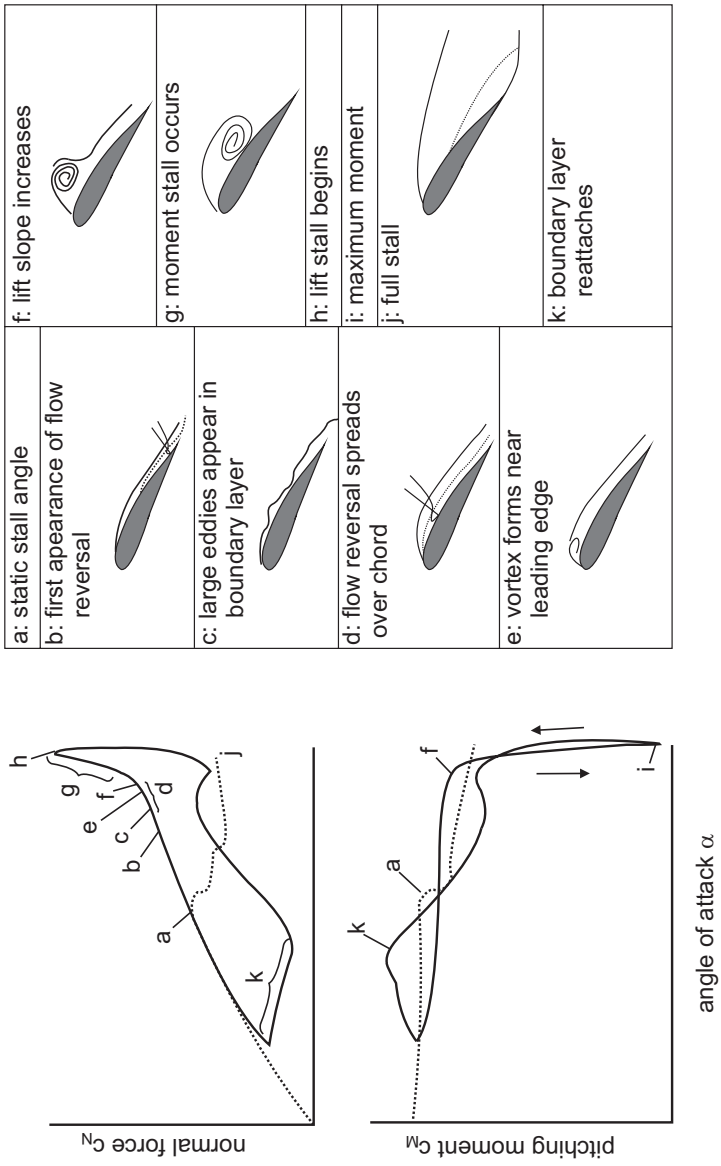

Figure 2.2: Correlation of the instantaneous normal force coefficient c_N, the instantaneous moment coefficient c_M and the development of vortical structures over the surface of an oscillating aerodynamic profile (adapted from Carr (1977).)

The dashed line in figure 2.2 shows the lift and moment curve for a stationary airfoil, the solid line for an unsteady airfoil. Early in the stroke cycle (before the static stall angle is exceeded) the lift curve of the unsteady airfoil follows the steady curve. Changes occur as soon as this angle is exceeded, at the instant in the stroke cycle marked with (a). The flow starts to separate from the airfoil surface and the unsteady lift increases beyond the maximal achievable lift for the static case. For the instants (b) to (e) the flow reversal near the wall spreads over the whole airfoil, the boundary layer adjusts to the externally imposed flow conditions and the initial lift slope is maintained. With the formation of a distinct LEV at (f) the lift slope increases with growing LEV size. After reaching its maximal size at (h), the LEV detaches from the airfoil leading to full stall at (j) and the lift drops. During the stages of the reattachment of the boundary layer at (k) the unsteady lift undershoots the steady lift. After the reattachment the unsteady airfoil exhibits again unstalled conditions at (l) and matches the steady lift curve.
McCroskey (1982) explains the impact of the effective angle of attack occurring during a stroke cycle on the development of the dynamic stall. Figure 2.3 compares two different stall regimes. Figure 2.3 (a) shows the stall conditions referred to as light stall, which prevails for comparatively low effective angles of attack. Prior to light stall, the airfoil is at the onset of stalling. During this stage flow separation is present only over a small portion of the airfoil chord. This regime corresponds to stages (l) to (a) in figure 2.2; in these stages the lift slope is maintained without a drastic increas in drag. If the effective angle of attack is further increased, then light stall occurs. The boundary layer separates from the airfoil, but no distinct vortex rolls up. This regime can be found in the stages (a) to (b) in figure 2.2. The deviations in the lift curve for this stage indicate the first hysteresis effects for the light stall regime. If the effective angle of attack is increased even further, the flow is in the deep stall regime, shown in figure 2.3 (b). The flow is dominated by a large LEV and strong hysteresis effects are present and the drag increases drastically. The lift drops drastically with the detachment of the LEV, leaving a fully stalled airfoil. In this stage the growth and detachment of the LEVs dominates the flow field and the resulting forces.

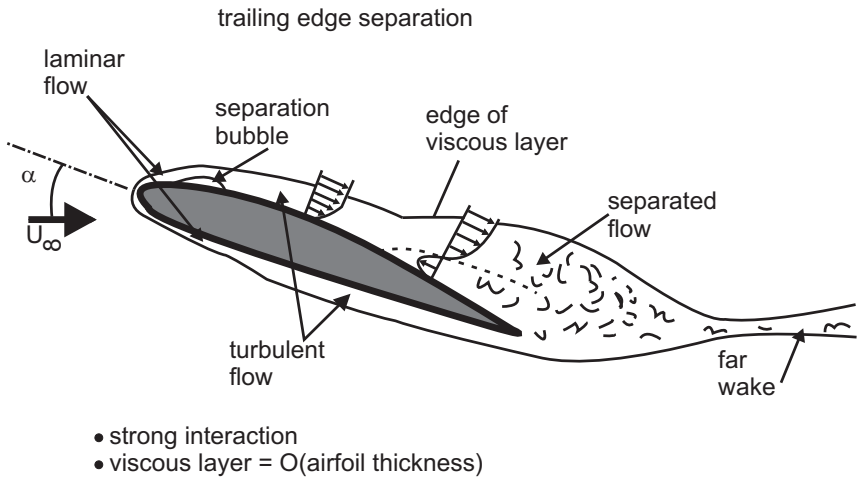

(a) Light stall

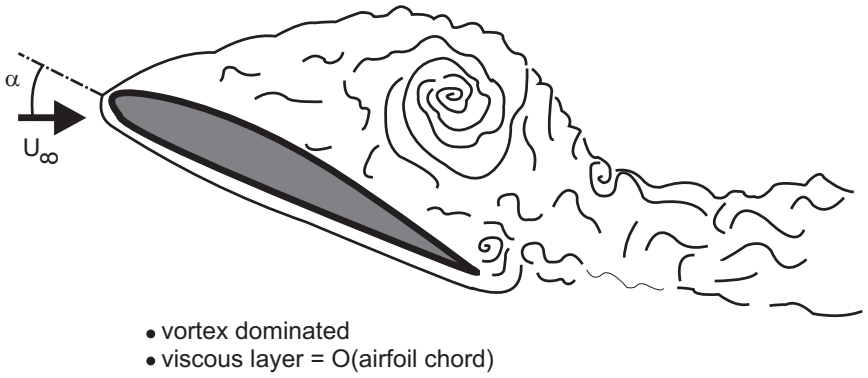

(b) Deep stall

Figure 2.3: Schematic representation of two dynamic stall regimes of an unsteady airfoil, adapted from McCroskey (1982)

From this example it already becomes obvious that the vortex dynamics are crucial for the performance of an unsteady airfoil. A prolonged LEV growth may enhance the produced lift of an airfoil; airfoil kinematics optimally tuned to LEV growth and detachment may suppress fully stalled airfoil conditions and therefore prevent the drop in lift and the associated increase in drag.
The drop in lift can be explained by considering the vortical impulse. Since the airfoil is the only device that can exert a force on the flow and change its impulse, the change in vortical impulse directly contributes to the force on the airfoil. Wu *et al.* (2006) explain the force F_{vort} exerted by a vortical structure as the rate of change of its impulse I_{virt}. This rate of change in the vortical impulse is given by its circulation Γ and the motion of the structure and reads $F_{vort} = -\rho\frac{\partial}{\partial t}(\int_S \Gamma \, \mathrm{d}S)$, where S represents the area covered by the vortical structure. The force may therefore be divided into $F_{vort} = -\rho\frac{\partial \Gamma}{\partial t}(\int_S \mathrm{d}S) - \rho\Gamma\frac{\partial}{\partial t}(\int_S \mathrm{d}S)$, where $\frac{\partial}{\partial t}(\int_S \mathrm{d}S)$ represents the convective speed of the structure. At the instant of LEV detachment, the LEV circulation is assumed to be constant, yielding $\frac{\partial \Gamma}{\partial t} = 0$, but then the formerly attached LEV changes its convection speed and moves away from the airfoil. The vortical impulse therefore experiences a drastic change due to the drastically increased convection $\frac{\partial}{\partial t}(\int_S \mathrm{d}S)$ and the lift force drops accordingly.

2.3 Shear layer roll-up and vortex formation

For an unsteady airfoil the LEV is created by the roll-up of a shear layer, which separates from the airfoil surface at the leading edge. In general, a vortex may be created according to Gharib *et al.* (1998), when a shear layer separates from the wall at an edge. A schematic of a simplified vortex formation is given in figure 2.4.

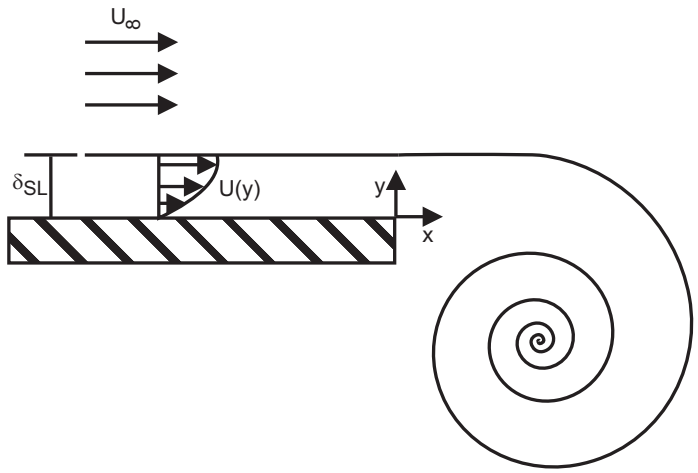

Figure 2.4: Schematic view of vortex formation due to the roll-up of a shear layer

A shear layer with the velocity profile $u(y)$ and the shear layer thickness δ_{SL} forms at the solid wall due to the imposed free stream flow with the uniform velocity of U_∞ and the no slip condition at the wall for $y = 0$. At the edge ($x = 0$ and $y = 0$) the shear layer separates from the wall and rolls-up into a vortex due to its instability against small disturbances, as explained by Michalke (1964). Vortex rings emanating from a shear layer have been experimentally generated by a number of authors using a piston to eject a fluid column into a plenum, among them Didden (1979), Gharib *et al.* (1998), Dabiri and Gharib (2005). Sattari *et al.* (2012) or Whalley and Choi (2012) use dielectric barrier discharge (DBD) actuators to create an isolated starting vortex emanating from a shear layer in absence of any geometrical length scales and study their formation and detachment behavior. According to Kaden (1931) the emerging vortex is then fed by the shear layer with vorticity carrying fluid, which increases the vortex size, mass and circulation.
The amount of vorticity ω contained in the shear layer is determined by the pressure gradient at the separation point. The pressure gradient is linked to the shape of the edge, which in turn determines the vorticity in the shear layer. The following simplification of the Navier-Stokes equation in x-direction (k as the volume forces, ρ as fluid density, η as dynamic viscosity and λ^* as the first Lame-parameter) for Newtonian fluids clarifies this statement:

$$\begin{aligned} \underbrace{\rho \frac{Du}{Dt}}_{\substack{=0, steady, \\ no\ slip, \\ no\ penetration}} &= \underbrace{\rho k}_{=0,\ no\ volume\ forces} - \frac{\partial p}{\partial x} \\ &+ (\lambda^* + \eta) \frac{\partial}{\partial x} \underbrace{\left[\frac{\partial u}{\partial x} + \frac{\partial v}{\partial y} \right]}_{=0,\ incompressible} \\ &+ \eta \underbrace{\left[\frac{\partial^2 u}{\partial x^2} + \frac{\partial^2 u}{\partial y^2} \right]}_{\frac{\partial u}{\partial x} << \frac{\partial u}{\partial y}} \end{aligned} \tag{2.1}$$

Inserting the definition for the vorticity $\omega = \frac{\partial v}{\partial x} - \frac{\partial u}{\partial y}$ into equation 2.1

leads to:

$$\frac{\partial p}{\partial x} = \frac{\partial \omega}{\partial y} \approx \frac{\omega}{\delta_{SL}} \tag{2.2}$$

Considering the ideas of Kaden (1931) the increase in mass m and circulation Γ of the LEV may then be expressed as the transport of fluid and vorticity through the shear layer by the following equations (the symbol $\dot{}$ denotes the temporal derivative $\frac{\partial}{\partial t}$).

$$\dot{m} = \rho \int_{y=0}^{\delta_{SL}} u(y)\, dy \tag{2.3}$$

$$\dot{\Gamma} = \int_{y=0}^{\delta_{SL}} \omega(y) u(y)\, dy \tag{2.4}$$

Didden (1979) suggests a first order approximation $\omega \approx \frac{U_\infty}{\delta_{SL}}$ and a convective fluid transport with a velocity of $\frac{1}{2}U_\infty$ to approximate a solution for equations 2.3 and 2.4, which then yields:

$$\dot{m} = \frac{1}{2}\rho U_\infty \delta_{SL} \tag{2.5}$$

$$\dot{\Gamma} = \frac{1}{2}U_\infty^2 \tag{2.6}$$

Didden (1979) verifies his results experimentally. According to Moore (1975) a more precise approximation is only possible with *a priori* knowledge of the shear layer shape. Considering equations 2.5 and 2.6, it becomes apparent that an increase in circulation does not depend on the shear layer thickness, while the mass flux depends on the shear layer thickness. The effect of leading edge shape with respect to the vortex circulation increase is comparably small (at most of second order), but may be significant for the mass flux.
Despite these relations from Didden (1979), Prandtl (1927) points out other aspects of the importance of the leading edge shape on vortex formation. If a cylinder is placed in a uniform flow, vortices alternately form on the

upper and lower side of the cylinder. Characteristic for their growth and shedding is the cylinder diameter. A successive reduction of the cylinder size finally leads to an infinitesimal diameter as a limiting case. Under these conditions, the vortex formation occurs immediately at a defined location. Therefore the leading edge geometry determines the location of vortex formation and the pressure gradient necessary for initial vortex formation.
Betz (1950) stresses the viscous nature of vorticity generation in a shear layer by stating that the shear layer thickness has to decrease proportionally with the viscosity in order to maintain a constant rate of circulation increase for a vortex, which is consistent with equation 2.2. As an extreme case, for potential flow with a viscosity of 0, the shear layer is reduced to a discontinuity surface and a persistent vortex core is reduced to a singularity.
Rival *et al.* (2008) demonstrate the influence of a manipulated shear layer on the formation of an LEV in flapping flight experiments. By changing the airfoil plunging kinematics, it was possible to 'strengthen' the shear layer at the leading edge of an airfoil and consequently the maximum LEV circulation could be increased.
The properties of the shear layer, including highly viscous effects and the form of the leading edge from which the vortex evolves, play a significant role in the evolution, and potentially, the detachment of a distinct vortex. These properties determine the ratio between mass and circulation fed into the LEV through the shear layer.

2.3.1 Shear layer development on the leading edge of an unsteady airfoil

The shear layer development from the leading edge of an unsteady airfoil is the center of focus in the scope of the present study, therefore the above considerations are exemplarily transferred to this application. Especially the development of the shear layer with respect the characteristic non-dimensional numbers introduced in section 2.1 is discussed. Figure 2.5 schematically shows how the shear layer forms, separates and eventually feeds into an LEV.

It is apparent from figure 2.5, that in contrast to the the non-dimensional

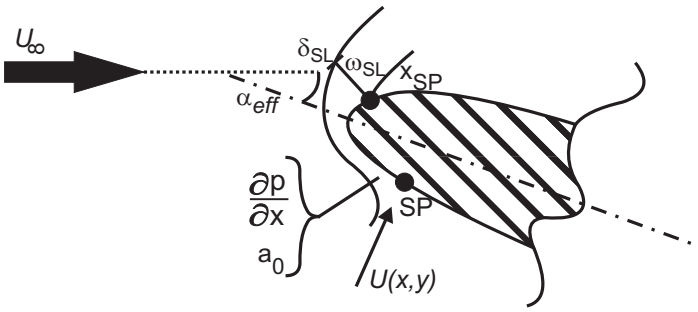

Figure 2.5: Shear layer development at the leading edge, exemplarily shown for the case of an unsteady airfoil. U_∞ denotes the free stream velocity, U denotes the instantaneous velocity experienced by the leading edge of the airfoil, α_{eff} is the instantaneous angle of attack and the dash-dotted line indicates the airfoil chord. From the stagnation point SP on the pressure side of the airfoil a shear layer evolves around the leading edge according to the pressure gradient $\frac{\partial p}{\partial x}$, separates at the critical point x_{SP} and feeds into a vortex. The shear layer properties are given in form of its thickness δ_{SL}, its vorticity ω_{SL} and its curvature a_0.

numbers introduced in section 2.1, the shear layer development is independent of the global flow field and is not linked to the flow around the trailing edge. Neither the chord length nor other global parameters are characteristic length scales for the shear layer development. The local flow field determines the shear layer parameters. In figure 2.5 the shear layer develops from a stagnation point SP at the leading edge, moves upstream around the airfoil nose and separates at a location x_{SP}, where the adverse pressure gradient is sufficiently large. The shape of the leading edge determines the pressure gradient $\frac{\partial p}{\partial x}$ experienced by the shear layer and therefore influences its thickness δ_{SL} and vorticity ω_{SL}, as well as the free stream velocity U_∞ and the kinematic viscosity ν. The curvature a_0 is determined by the the stagnation point flow, which depends on the angle of attack history $\alpha_{eff}(t/T)$. Because of these dependencies, the shear layer parameters of an unsteady airfoil may vary due to a variation of dimensional parameters, although the non-dimensional numbers are kept constant. The local leading edge flow field and the shear layer development on the leading edge

of an unsteady airfoil do not necessarily scale with the development of the global flow field, described by the non-dimensional numbers.

2.4 Optimal vortex formation

In chapter 1 the importance of the LEV detachment on the force history of the airfoil has been described. The vortex circulation and therefore the maximal instantaneous force is limited by the detachment mechanisms, and the instant of detachment is followed by a drastic drop in lift. The most common concept to estimate the limitations of an LEV in flapping flight-like applications is the concept of optimal vortex formation, introduced by Gharib *et al.* (1998) and transferred to efficient biological flight by Dabiri (2009).
The concept of optimal vortex ring formation was developed from the experimental results of Gharib *et al.* (1998). They pushed a column of fluid with a piston through an orifice into a plenum and observed the vortex rings developing from the shear layers forming at the edges of the orifice. After the initial roll-up of the vortex ring, its circulation was increased by entraining more vorticity carrying fluid emerging from the shear layer, during the advancement of the piston. While the overall circulation in the plenum grows continuously, the circulation of the distinct vortex ring reaches a plateau. The instant when the vortex ring no longer accepts any further increase in circulation is called 'pinch-off'. The vortex formation time in this case was defined as $T^* = \frac{\bar{U}_p t}{D} = \frac{L}{D}$, with D as the diameter of the orifice, t the physical time, L the piston stroke length and $\bar{U}_p$ as the averaged piston velocity. In other words, T^* described the evolution state of the vortex ring. Gharib *et al.* (1998) vary the experimental parameters in a wide range, but find that the non-dimensional pinch-off time occurs for all configurations at around $T^* \approx 4$. This indicates that the vortex ring evolves for $T^* < 4$, reaches its final state at $T^* \approx 4$ and does not change further for $T^* > 4$. All additionally produced circulation is stored in the wake after the vortex ring. The pinch-off is explained by topological considerations. With increasing circulation the self-induced convection velocity of the vortex ring increases until it is higher than the shear layer feeding velocity. At this point the fluid emerging from the shear is not entrained into the vortex ring, it rolls up into subsequent vortices trailing

behind the large vortex ring.
A prolongation of the vortex formation time could be achieved by a temporally varying orifice diameter D or varying the piston kinematics, as demonstrated by Dabiri and Gharib (2005) or Shusser *et al.* (2006).

2.4.1 Extension of the concept of optimal vortex formation to flapping flight

Dabiri (2009) transfers the concept of optimal vortex formation to biological flapping aerodynamics and redefines the vortex formation times T^* to adjust it to flapping wings. The formation is given by $T^* = \frac{C\Gamma}{D\Delta U}$ with C as a constant describing the physical properties of the vortex generator ($C = 1$ in the typical case for a plunging wing with one vortex shed per stroke cycle), Γ as the vortex circulation, ΔU as the velocity difference over the shear layer at the leading edge and D as a characteristic length, given by the plunging height $2\Delta h$, which is linked to the airfoil chord length c by the kinematic parameters k an St. Dabiri (2009) links the formation number to the Strouhal number, yielding $T^* = \frac{1}{St}$.
For the application of this concept to flapping wing aerodynamics the chord length of the wing c has been used as the characteristic length scale describing vortex formation, as described by Rival *et al.* (2008). Throughout a large number of biological and technical flapping flight examples, the concept of optimal vortex formation yields a maximal formation number of $T^* \approx 4$ for flight parameters governing efficient forward flight, which lies in a narrow Strouhal number range of $St = [0.2...0.35]$ as found by Triantafyllou *et al.* (2004), Nudds *et al.* (2004) or Taylor *et al.* (2003). The concept also agrees with the results of Milano and Gharib (2005), who find that the maximal generated lift on an airfoil coincides with a formation time of $T^* \approx 4$ or the results Rival *et al.* (2008), whose maximal vortex circulation matches the pinch-off criterion given by the concept of optimal vortex formation.

2.4.2 Universality of the concept

The examples above indicate a universal behavior of vortex formation on airfoils in efficient forward flight if the chord length c is chosen as the

characteristic length scale for the vortex formation time. Vortex growth therefore is limited by the airfoil size under these conditions. However, as the parameters deviate from the ones mentioned above, the agreement between the concept of optimal vortex formation and the experimental results deteriorate; see for example the experiments of DeVoria and Ringuette (2012) or Rival *et al.* (2010). Jones and Babinsky (2010) experimentally observe the detachment of an LEV before it reaches the trailing edge, indicating that that the chord length is not the limiting parameter for vortex growth in this case. Baik *et al.* (2012) show that the LEV detachment is delayed with a varying reduced frequency k, contradicting the predictions made by the concept of optimal vortex formation for higher reduced frequencies. For low reduced frequencies the findings of Baik *et al.* (2012) confirm the concept of optimal vortex formation.
Afanasyev (2006), Domenichini (2011) or Pedrizzetti (2010) observe starting orifice flows and the subsequent formation of vortex rings, similar to the the set-up of Gharib *et al.* (1998). The predictions made by the concept of optimal vortex formation do not hold for their respective cases. They attribute the limitation of their vortex rings to an instability of the feeding shear layer. Sattari *et al.* (2012) create a starting vortex in absence of any geometrical length scale from a wall jet produced by a DBD plasma actuator and observe its evolution. They show, that the detachment of a starting vortex from its feeding shear layer may occur despite the absence of a geometric length scale. The gradual separation of the vortex from its shear layer is attributed to vortex-vortex or vortex-wall interactions, which are inherent to the vortex formation process and cannot be avoided.
The examples given above show that the concept of optimal vortex formation is not universally applicable, but may be applied only in a certain range of wing kinematic parameters. It was shown that a geometrical length scale is not required for the detachment of a vortex from its feeding shear layer. The airfoil chord length may be the limiting parameter for vortex growth only under certain circumstances. A vortex-vortex or vortex-wall interaction is inherent to the process of vortex formation and can act as a limiting factor of the vortex growth. The airfoil chord length is therefore not universally characteristic for vortex detachment. To explain all experimentally observed discrepancies, the singlar vortex detachment mechanisms must be examined in more detail.

2.5 Flow topology

The concept of flow topology is introduced as a tool to better describe and understand the mechanisms leading to vortex detachment from an airfoil. Critical points in the fluid flow can be identified and classified, which allows a better understanding of the fluid mechanics, especially during the detachment of a vortex from a solid surface. Topology is originally a branch of mathematics, which deals with the properties of geometrical objects and their preservation during transformations (Flegg (2001)). A group of neighborhood properties of the points on the surface of such a geometrical object is invariant against transformations (such as stretching, rotation or skewing) and can therefore be classified in a topological sense. The most important of these invariants is the genus g, which is defined by Flegg as 'The greatest number of distinct continuous non-self-intersecting closed curves which may be drawn on a surface without separating it into distinct regions'. Therefore, according to Flegg (2001), a sphere has a genus of $g = 0$, a torus a genus of $g = 1$ and a two-fold torus of $g = 2$. The relationship of the genus to the surface of the geometrical object is given by the Euler characteristic $\chi = 2 - 2g$, which describes the topological features of a geometrical object. Geometrical objects which have the same invariants are topologically equal and have the same Euler-characteristic.
The relevance of the genus g can be illustrated by the well-known example of the hairy sphere. It can be imagined that the surface of a sphere or a torus has been covered by hair, which is 'combed' in such a way that it does not stick out but remains at the surface. It can be further imagined that each hair points in a distinct direction. If the condition is applied that throughout the whole surface no discontinuity in the direction is allowed (i. e. that the hair is combed smoothly), the value of the Euler-characteristic then denotes at how may points this condition cannot be fulfilled. Figure 2.6 (a) and (b) shows two examples of how the hair might be combed on a sphere and how the hair is combed on a torus. Please note that on the sphere two-discontinuities are present, while on the torus no discontinuity is present.

A given geometry may be altered in a topological sense by cutting holes or attaching handles to its surface, which corresponds to a change in the genus of an geometrical object. A torus for example is topologically equivalent to a sphere with an attached handle. To account for such a transfer

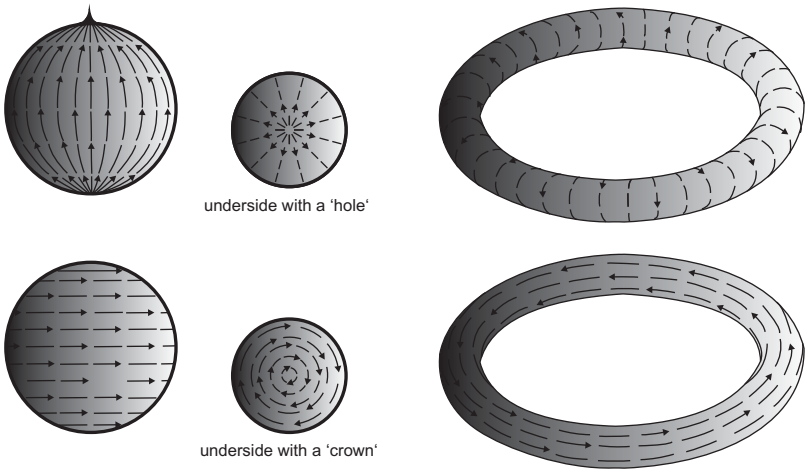

(a) Hairy Sphere (b) Hairy Torus

Figure 2.6: Discontinuous points on the surfaces of (*a*) sphere and (*b*) a torus if the anticipated hair is combed smoothly on the respective surface, adapted from Flegg (2001)

of topological features the Euler-characteristic has to be adjusted accordingly. The Euler-characteristic then yields $\chi = 2 - \Sigma holes - 2\Sigma handles$ according to Flegg (2001).
The points of discontinuity on the surface can be classified according to their properties. The hole in figure 2.6 (*a*) may be represented by a source or a sink, the 'crown' by a vortex. Other possible points are crosspoints (or saddle points) or dipoles. Each point has an integer according to its properties: Sources, sinks and vortices have an index of +1, saddle points of −1 and a dipole of 2.
Topological concepts to visualize flow patterns have been applied by Hunt *et al.* (1978) or Perry and Chong (1987), (1994) or (2000). Huang *et al.* (2001) use topological arguments to distinguish different flow patterns produced by an oscillating airfoil. Foss (2004) transfers the concept of topological analysis to numerous examples in fluid mechanics. The flow regime corresponds in this case to the topological surface and may ac-

cordingly be expressed by the Euler-characteristic. As described in the paragraph above, this flow regime can be connected to the number and character of discontinuous points in the flow by the Euler-characteristic. Discontinuous points in this case are referred to as critical points in general. At these points the flow direction is undetermined, which physically requires zero flow velocity. The most important examples of such critical points are nodes (vortex centers, sources or sinks) or saddle points. These points can either occur in the flow or at a solid wall and can be characterized by their Poincare-Bendixon-index i. A vortex in the free flow has a Poincare-Bendixon-Index of $i = 2$, a saddle point of of $i = -2$. If critical points appear at a solid wall, their index is half of their index in the free flow. Saddle points at a solid wall are referred to as half saddles and have an index of $i = -1$.
These critical points represent flow features in the flow regime, which may be connected to the flow regime with the Euler-characteristic in equation 2.7, given by Foss (2007).

$$\chi = 2 - \Sigma holes - 2\Sigma handles = \Sigma nodes - \Sigma saddles \tag{2.7}$$

According to equation 2.7 the flow regime determines the possible combination of flow features, which may appear in the flow field. If the topology of the flow regime is not changed, the Euler-characteristic remains constant. If new flow features appear, a subsequent set of features inevitably emerges in order to balance equation 2.7 again.
Wu, Ma and Zhou (2006) show that that a two-dimensional configuration with a vortex above a wall is topologically instable. Figure 2.7 (a) shows such a typically situation. The vortex center is denoted by N and the two half-saddles confining the vortex with S_1' and S_2'. The instability arises from the direct connection of the two half saddles confining the vortex, the given topology can not persist. In contrast a topologically stable configuration is shown in figure 2.7 (b) and (c) the rotating vortex center is superimposed with a source or a sink, allowing the flow to move perpendicular to the image plane. Such a configuration is topologically stable. If a topological change from a vortex center to a combined sink/center or source/center is impossible due to two-dimensional experimental conditions, the instability could cause secondary topological structures to form.

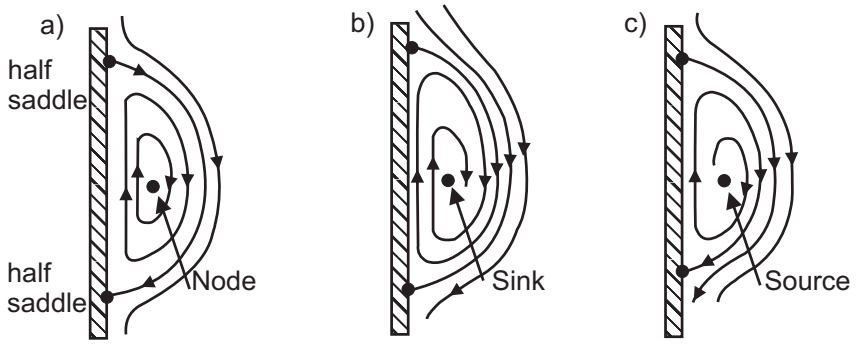

(a) Topological instable configuration due to the direct half-saddle connection

(b) Topologically stable configuration due to a combination of the vortex center with a sink

(c) Topologically stable configuration due to a combination of the vortex center with a source

Figure 2.7: Schematic representation of a nominally two-dimensional vortex above a wall adapted from Wu, Ma and Zhou (2006)

This concept can be used to analyze the case of a plunging airfoil in the wind tunnel, for example applied by Huang *et al.* (2001). The flow regime is in this case represented by the wind tunnel and the airfoil. The topology of this flow regime is schematically depicted in figure 2.8. The dashed line represents the flow regime and corresponds to a sphere with two holes (the wind tunnel) and one handle the airfoil. The incoming flow is denoted by U_∞. The Euler-chracteristic in this case is $\chi = 2_{sphere} - 2 \cdot 1_{2\ holes} - 1 \cdot 2_{1\ handle} = -2$.

How the set of present flow features is preserved during an experiment of a plunging airfoil with LEV development can be schematically shown in figure 2.9. Nodes or vortex centers are denoted by N, saddle points by S and half saddles by S'. The easiest configuration is an attached flow on the airfoil. Two stagnation points on the leading and the trailing edge are present, both are half saddle points with an index of $i = -1$. The

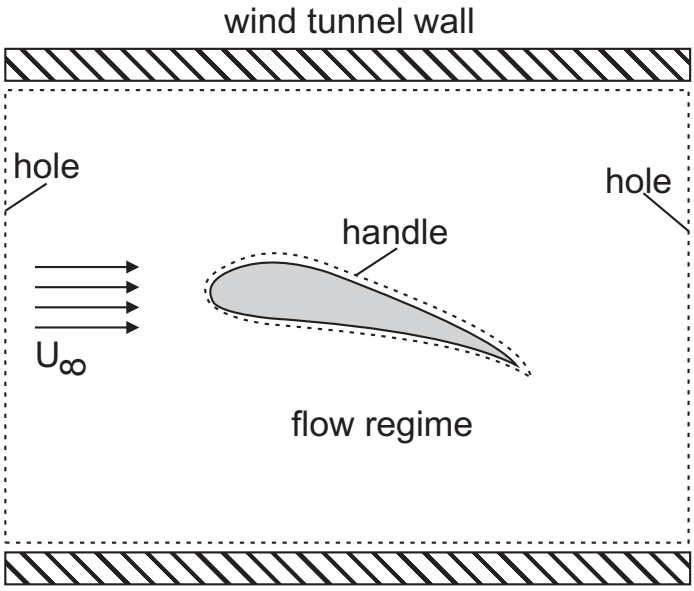

Figure 2.8: Schematic of the flow regime in a wind tunnel with a plunging airfoil and its topological representation

Euler-characteristic then yields $\chi = 2 \cdot (-1)_{half\ saddle} = -2$, which agrees with the flow regime topology. This flow situation is schematically shown in figure 2.9 (a). As soon as a vortex develops, the Euler-characteristic becomes more complicated. Because the vortex center is counted with $i = +2$, either two new half saddles ($2 \cdot (-1)$) or one full saddle ($1 \cdot (-2)$) have to appear in the flow in order to balance the Euler-charateristic. The former type represents an attached vortex, the letter a detached one. Both physically relevant topological configurations are schematically shown in figure 2.9 (b) and figure 2.9 (c). Prior to figure 2.9 (c) the reattachment point represented (half saddle) behind the LEV merges with the stagnation point (half saddle) at the trailing edge, detaches from the airfoil and forms a full saddle in flow, allowing fluid to flow around the trailing edge and be transported upstream.

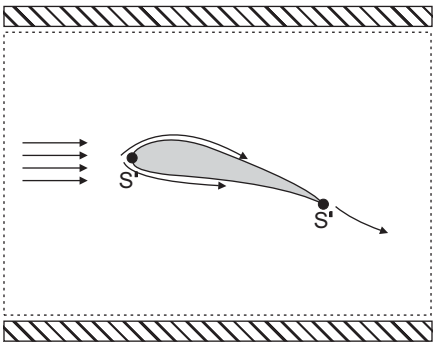

(a) Attached flow

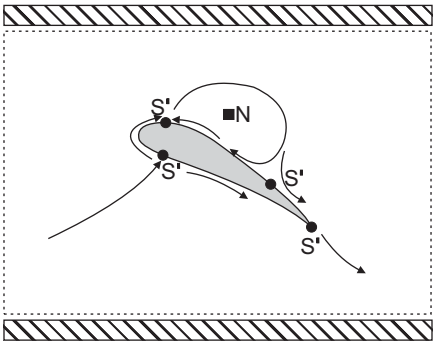

(b) Attached LEV

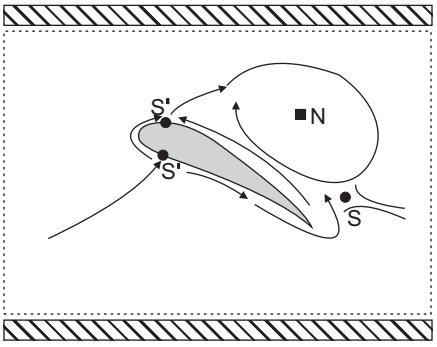

(c) Detached LEV

Figure 2.9: Exemplary evolution of flow features and corresponding topological changes in order to fulfill to Euler-characteristic

2.6 Vortex detachment mechanisms

The mechanisms leading to the limitation and/or the detachment of the LEV are of crucial importance to predict their impact on the lift curve. From section 2.2 it becomes apparent that the lift drastically drops and drag substantially increases with the detachment of the LEV. Usually this detachment process is related to the global flow topology (as demonstrated by Rival *et al.* (2014)), represented by the LEV and the instantaneous streamline confining the inner part from the free stream. During LEV growth this streamline terminates in a reattachment point downstream of the LEV center on the airfoil surface. From this stagnation point fluid is fed either back into the LEV or downstream over the airfoil. Therefore the flow direction at the reattachment point is not defined and the flow velocity at that point is zero. The reattachment point corresponds to a stagnation point. The typical concept to relate the LEV detachment (and the drop in lift) with an instant in the stroke cycle is the position of the reattachment. When the LEV has grown sufficiently that the reattachment point reaches the trailing edge, it is no longer confined to the airfoil and detaches. But why should the trailing edge have an effect on the LEV detachment, when it is supplied with vorticity from the shear layer emanating from the leading edge as described in section 2.3? It is therefore necessary to describe the possible mechanisms leading to LEV detachment in the literature to estimate the physical relevance of such a concept. Basically two different mechanisms appear in the literature, which are briefly described in the subsections 2.6.1 and 2.6.2 below.

2.6.1 Bluff body vortex detachment

A commonly known case of the formation, detachment and convection of vortices into the wake are bluff bodies placed in a uniform flow. Literature regarding this topic is provided for example by Roshko (1954), Williamson (1996) or Gerrard (1966). The flow field around a bluff body is dominated by the formation and detachment of vortices from the alternating sides of the bluff body, as schematically shown in Figure 2.10.

A vortex V_1 rolls up behind a bluff body and grows as it is fed by flow A, which originates at the shear layer SL_1 emanating from the edge on the right side of the bluff body, as described in paragraph 2.3. Gerrard (1966) explains the beginning detachment of the vortex V_1 with the entrainment of the shear layer SL_2, which emanates from the left edge of the bluff body and therefore has opposite signed vorticity ω. As soon as flow B moves across the width of the wake (which is the physical length scale separating both shear layers), the shear layers SL_1 and SL_2 interact, the vortex V_1 detaches and is convected into the wake. At the same time the previous entrainment of the shear layer SL_2 causes flow C. A new vortex of opposite rotation to V_1 starts to grow.

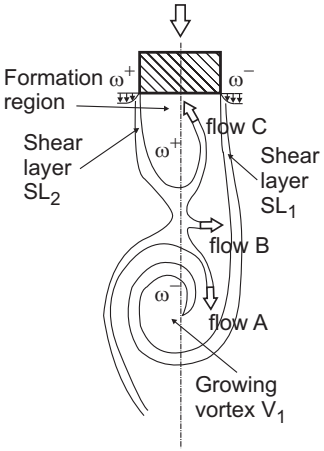

Figure 2.10: Alternating formation and detachment of vortices due to the entrainment of different flow portions from a bluff body. Adapted from Bentley and Mudd (2003)

This concept of vortex detachment from a bluff body is consistent with the considerations of Roshko (1954) and Wu, Ma and Zhou (2006). Wu, Ma and Zhou (2006) use topological arguments to explain the vortex detachment from a bluff body. Figure 2.11 (taken from Williamson (1996) and modified) illustrates this mechanism by means of the instantaneous streamlines. The temporal evolution in the formation and detachment is shown in eight subfigures from (a) to (h). A vortex A with a center N_1 grows from the upper side of a rectangular bluff body. Initially in figure 2.11 (a) it is bounded by the half saddles S_3' and S_4', the stagnation points S_1' and S_2' fulfill the topological constraints. As soon as vortex A grows, S_3' moves across the width of the bluff body and merges with S_2', forming a full saddle point S_1, shown in 2.11 (e). Vortex A is not bounded at the bodies surface anymore, fluid from the lower side of the body is entrained into the region behind the bluff body. A second vortex B forms and the interaction of the shear layer feeding vortex A with fluid of opposite signed vorticity is enabled.

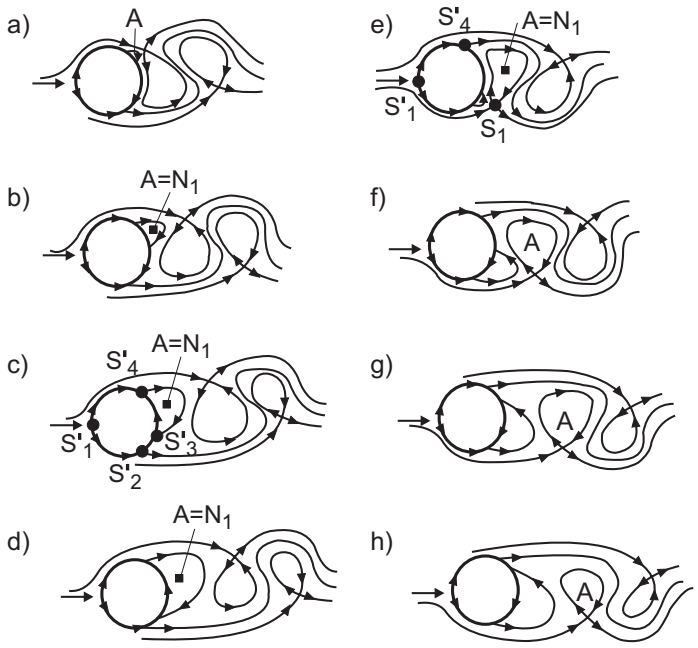

Figure 2.11: Instantaneous streamlines and selected critical points at different stages of vortex formation (adapted from Williamson (1996)). The flow topology clearly demonstrates the mechanism of vortex detachment.

Roshko (1954) emphasizes the meaning of the wake width as the physical parameter which separates both shear layers of opposite signed vorticity from another. Therefore the wake width determines the distance, which has to covered by the entrained shear layer until an interaction of both shear layers and a subsequent vortex detachment is possible. The width of the wake is then successfully used as a characteristic length scale to define a universal non-dimensional vortex shedding frequency $St_{bluff} = \frac{f_{shed} l_{char}}{U_{char}}$ for a number of differently shaped bluff bodies, with f_{shed} as the vortex shedding frequency, l_{char} as a characteristic length scale and U_{char} as a characteristic flow velocity. The characteristic flow velocity U_{char} is given by the wake velocity which in turn depends on the base pressure on the front of the bluff body, which also has an effect on the shear layer properties as described in paragraph 2.3.
It can be concluded that the mechanism of vortex detachment from bluff bodies depends on the global flow topology, especially on the position of the half saddles confining the growing vortex. Regardless of any viscous effects the growing vortex starts to detach, as soon as the confining half saddle has crossed a characteristic length associated with the bluff body diameter. This concept is transferred to the case of an unsteady airfoil by Rival *et al.* (2014). An LEV is also confined by a half saddle on the airfoil surface, which moves rearwards as long as the LEV grows. As soon as it moves beyond the airfoil's trailing edge two half saddles merge and flow reversal around the trailing edge occurs. The shear layer created at the trailing edge is then entrained and transported upstream to the leading, where both shear layers of opposite signed vorticity can interact and lead to vortex detachment. In this case the chord length of the airfoil is the characteristic length determining the interaction of both shear layers. Figure 2.12 taken from Rival *et al.* (2014) illustrates this mechanism. Nodal points are depicted by green points, half saddles with yellow squares and full saddles with red squares. In figure 2.12 (*a*) the flow still attached, in figure 2.12 (*b*) a leading edge vortex has formed and is confined by two half saddles, but has not detached yet. Figure 2.12 (*c*) shows the flow prior to the LEV (upper part) and during LEV detachment (lower part). The merging of two half saddles to a full saddle and the subsequent flow reversal at trailing edge initiating LEV detachment.

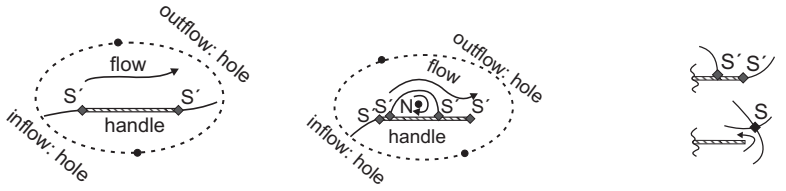

(a) Attached flow (b) Separated flow (c) Flow at the trailing edge

Figure 2.12: Topological representation of the bluff body vortex detachment mechanism transferred to the case of an unsteady airfoil, adapted from Rival *et al.* (2014)

2.6.2 Boundary-layer eruption driven vortex detachment

A second mechanism leading to vortex detachment from a solid surface is presented in the literature, described by Gendrich (1999) or Doligalski *et al.* (1994). This mechanism is the result of an interaction between the inviscid flow features far from the wall and the response of the viscous boundary layer. Figure 2.13 illustrates this situation. A vortex V_1 of the circulation Γ_1 is placed above a solid wall at a vertical distance of y_1 and a homogeneous free stream velocity with the magnitude U_∞ is added. A velocity below the vortex is induced due to its circulation. Note that the vortex V_1 and the boundary layer below V_1 have vorticity with of opposite sign, due to the no-slip condition. Initially in 2.13 (a) the vortex is confined by two half saddles S_1' and S_2'. S_1' and S_2' are stagnation points, where a maximum of the static pressure p occurs. Just below the vortex center with the nodal point N_1 the local velocity $U(x, y)$ is maximal. Along the wall from $x = 0$ to S_1', a positive pressure gradient $\frac{\partial p}{\partial(-x)} > 0$ persits. If the distance a between the vortex V_1 and the wall is decreased or the circulation Γ_1 is increased, the induced velocity magnitude increases accordingly, as well as the pressure gradient $\frac{\partial p}{\partial(-x)}$. Such a change in the flow field is inviscid. If the induced velocity and the pressure gradient exceed a critical value, the boundary layer separates from the surface due to viscous effects, as depicted in 2.13 (b). Doligalski *et al.* (1994) refers to this separation as 'boundary layer eruption' and describes it as an ejection of fluid out of

the boundary layer, forming a 'cloud' or 'spire' with accumulated vorticity. Although Doligalski *et al.* (1994) do not consider topological arguments, a change in the flow topology can be observed. The cloud of (with respect to V_1) counter-rotating fluid forms a new node N_2, accompanied by the formation of two new half saddles S_3' and S_4'. In order to have a continuous flow field at each point x, y a full saddle has to form above N_2 and to fulfill the topological constraints a third node N_3 must form. Due to their rotation, the nodal points N_2 and N_3 are considered as secondary vortical structures. According to Doligalski *et al.* (1994) the interaction between the eruption and the vortex V_1 causes it to detach.

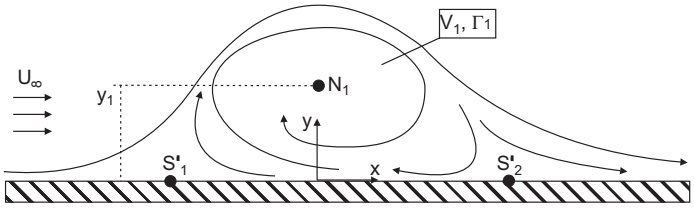

(a) Flow topology prior boundary layer separation

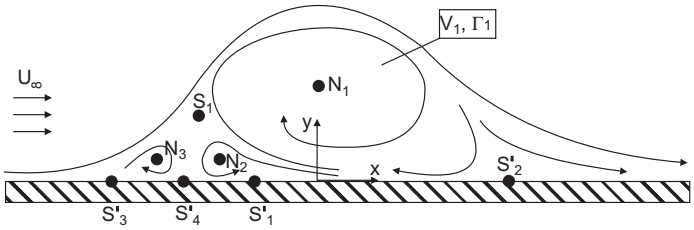

(b) Flow topology after boundary layer separation

Figure 2.13: Schematic representation of the boundary layer separation on a solid surface below a vortex due to viscous/inviscid interactions

Doligalski *et al.* (1994) give a criterion for which the boundary layer separation occurs. Note that this criterion is restricted to the generic case of an steady infinitely long plate without external pressure gradient and the assumption of a rectilinear vortex. A fractional convection

rate $k^* = \frac{\Gamma_1}{4\pi y_1 U_\infty}$ is defined, with higher k^* provoking stronger viscous responses of the boundary layer. If k^* exceeds a critical value due to an increase of the circulation Γ_1 or a decrease of the wall distance of the vortex y_1, the viscous response in form of the eruption takes place. For the above mentioned generic case the critical fractional convection rate is $k^* > 0.25$. The eruption therefore does not explicitly depend on the circulation, but on the velocity induced by the vortex V_1, which depends on the vorticity distribution, the compactness of the vortex and its proximity to the wall. Therefore a smaller and more compact vortex (containing less mass and less circulation) may more likely cause a boundary layer eruption with a subsequent topological change due to its proximity to the solid wall than a vortex, which is stronger in circulation but also in diameter. As explained in paragraph 2.3 the shear layer properties define the ratio of mass and circulation fed to a vortex and may therefore be characteristic for the onset of the boundary layer eruption.
If this concept is transferred to the case of an unsteady airfoil it can be concluded that the vortex detachment mechanism relies on the localized viscous/inviscid interaction of the LEV and the boundary layer in a confined area near the leading edge. The global flow topology and especially the position of the rear reattachment has (in contrast to the bluff body vortex detachment mechanism) no relevance, which means that no geometrical length scale determines the evolution of secondary vortical structures and the LEV detachment. These secondary structures (nodes N_2 and N_3, full saddle S_1 and half saddles S_5' and S_6') cause a redistribution of fluid emerging from the shear layer, as shown in figure 2.14. Initially a large fraction of this fluid is carried into the LEV (node N_1, confined by the half saddles S_3' and S_4') as shown in figure 2.14 (a), but with the occurrence of the boundary layer eruption and its additional nodal point N_2, the flow topology changes as shown in figure 2.14 (b). The full saddle S_1 redistributes the fluid emerging from the shear layer into the third vortex structure around N_3 at the leading edge. As this vortex accumulates more vorticity and starts growing, less vorticity is fed into the LEV, it is cut off from its feeding shear layer while its reattachment point S_4' has not moved beyond the trailing edge. In accordance with the considerations of Wu, Ma and Zhou (2006), the appearance of a full saddle leads to final separation of the LEV and shear layer. Huang *et al.* (2001) find secondary vortical structures in their experiments, which correspond to the described mechanism of eruption driven vortex detachment.

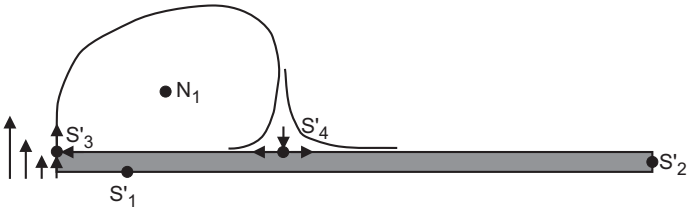

(a) Flow topology prior boundary layer separation

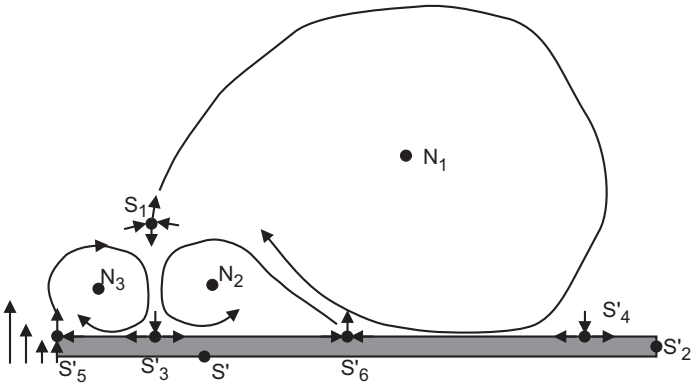

(b) Flow topology after boundary layer separation

Figure 2.14: Topological representation of the eruption driven vortex detachment mechanism transferred to the case of an unsteady airfoil

2.6.3 Implications of the different vortex detachment mechanisms

The previous two paragraphs 2.6.1 and 2.6.2 show that in principle at least two mechanisms may lead to the detachment of a vortex from an airfoil. Both mechanism have in common, that the formation of a full saddle causes a topological change, which leads to the interaction of the LEV feeding shear layer with secondary structures and eventually causes the LEV

to separate from its feeding shear layer. While for the bluff body vortex detachment the geometrical length separating both interacting shear layers is a characteristic length scale, the eruption driven mechanism does not depend on a geometrical length scale. The bluff body vortex detachment mechanism is determined by the inviscid global topology, while the eruption driven mechanism is the result of a localized viscous/inviscid interaction. The reason for this viscous/inviscid interaction is the pressure gradient imposed on the boundary layer by the attached vortex. As explained in paragraph 2.6.2, the viscous boundary layer response is provoked, when the vortex reaches a critical circulation and size (or wall proximity) ratio, which is in turn dependent an the shear layer parameter, as explained in paragraph 2.3. This ratio may be expressed as $\frac{\partial \Gamma}{\partial t} / \frac{\partial V}{\partial t} = f({U_\infty}^1, {\delta_{SL}}^{-1})$, with the volume of the vortex V and the circulation Γ. This ratio indicates that the free stream velocity U_∞ and the shear layer thickness δ_{SL} may be appropriate parameters to normalize an LEV which detaches due to a boundary layer eruption. For the case of bluff body vortex shedding the characteristic parameters are the free stream velocity U_∞ and the chord length c accordingly.

2.7 Hypotheses

As seen in the previous sections, the LEV growth is ultimately limited to the instant, when it has grown enough that its rear stagnation point reaches the airfoil trailing edge. The latest instant of LEV detachment occurs therefore when the LEV covers the whole chord length c and the LEV radius r spans from leading to trailing edge. Figure 2.15 shows the growth of the LEV schematically: Mass is transferred from the separated shear layer with a thickness of δ_{SL} and a curvature a_0 at the leading edge into the LEV, which increases in area A and radius r. ν denotes the kinematic viscosity of the fluid and U_∞ the free stream velocity. The circulation increase of the LEV is determined by the transport of vorticity ω^-.

If the LEV extends sufficiently far over the airfoil chord, flow reversal at the trailing edge takes place and the LEV cannot grow any longer. The ratio $\kappa = \frac{2r}{c}$ reaches a critical value for that instant. (Note that a critical value $\kappa = \frac{2r}{c} = 1$ is expected, but is related to an instantaneous value of

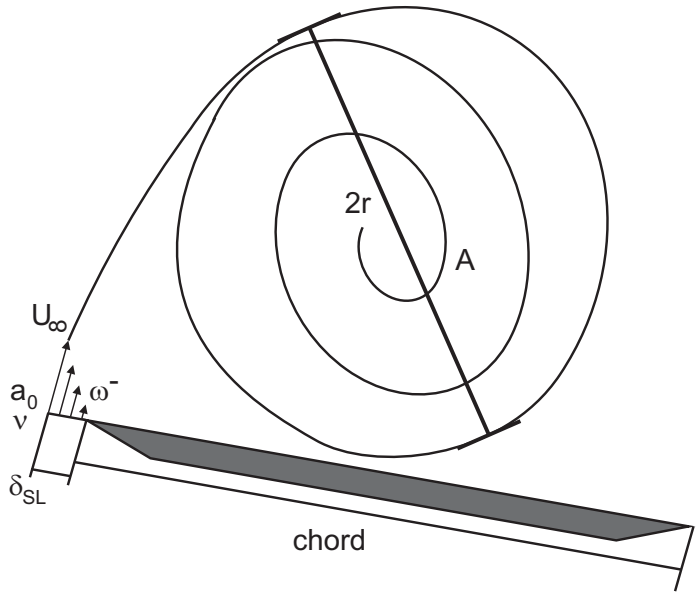

Figure 2.15: Schematic depiction of the mass transport from the shear layer with a thickness δ_{SL}, a curvature a_0 and vorticity ω^- into a hypothetically circular LEV with a diameter $2r$ and an area A on an unsteady airfoil, adapted from Widmann and Tropea (2015).

r. If κ is expressed by the parameters governing the airfoil motion (Re, k, St and $\alpha_{eff,max}$), the histories of shear layer development or airfoil kinematics cannot by considered and therefore the critical value κ_{crit} related to the airfoil motion parameters might deviate from the ideal value of 1.) A transition between both detachment mechanisms occurs for a value of κ_{trans} (which is expected to be smaller than κ_{crit}), for which the bluff body mechanism and the eruption mechanism coincide. The LEV growth is determined by the mass transfer from the shear layer. The quantities influencing LEV growth are therefore denoted as follows: A is the area covered by the LEV, r is the LEV radius (assuming circular size). The mass flux $\frac{1}{2}U_\infty\delta_{SL}$ is given by free stream velocity U_∞, the shear layer thickness δ_{SL} (which in turn depends on the kinematic viscosity of the fluid ν). The

parameter a_0 is representative of the curvature of the shear layer . The motion period T determines the time during which transfer from the shear layer into the LEV is possible. A is computed from the mass flux $\frac{1}{2}U_\infty\delta_{SL}$ into the LEV, the shear layer thickness δ_{SL} is assumed to emerge from the stagnation point and can be estimated using the Falkner-Skan solution. The LEV cover ratio κ can therefore be rewritten using the above definitions:

$$\kappa_{trans} = \frac{2r}{c} \tag{2.8}$$

$$r_{LEV} = \sqrt{\frac{A_{LEV}}{\pi}} \tag{2.9}$$

$$A_{LEV} \approx \frac{1}{2}U_\infty\delta_{SL}T \tag{2.10}$$

$$\delta_{SL} = 2.4\sqrt{\frac{\nu}{a_0 U_\infty}} \tag{2.11}$$

The expression $U_\infty T$ can be replaced by $\frac{\pi c}{2k}$ in equation 2.10, yielding:

$$\kappa_{trans} \approx \sqrt{2.4 * 2}c^{-0.5}k^{-0.5}\nu^{0.25}a_0^{-0.25}U_\infty^{-0.25} \tag{2.12}$$

A numerical value for κ_{trans} cannot be determined analytically, and is likely to depend on the airfoil kinematics, since they influence the shear layer development and the mass and vorticity flux into the LEV. Instead, κ_{trans} may be determined for fixed airfoil kinematics by a case, for which both detachment mechanisms occur at roughly the same time. Equation 2.12 can be rewritten and depends on three non-dimensional groups of parameters: $\kappa = f(k, Re, a_0 c)$. Each group is therefore investigated experimentally in this study. The reduced frequency k and the Reynolds number Re are directly varied while keeping all other parameters constant. The term $a_0 c$ is on one hand varied by investigating different leading edge shapes under the same fluid dynamic conditions and on the other hand by investigating airfoils of different chord lengths but sharp leading edges with the same non-dimensional parameters. The aim of the present investigation is to

better understand the mechanisms leading to the formation and detachment of LEVs. The theoretical considerations help to develop hypotheses, which will be experimentally and numerically verified in order to explore the underlying flow physics. Of importance are especially the shear layer properties connected with the evolution of an LEV. For the given case of an unsteady airfoil, three time scales effect the LEV behavior. The first time scale is given by the airfoil kinematics by the reduced frequency k, as explained in paragraph 2.1. The second time scale determines the LEV growth $\frac{\partial \Gamma_{LEV}}{\partial t}$, which is, according to Roshko (1954), proportional to the flow velocity U_∞: $\frac{\partial \Gamma_{LEV}}{\partial t} \propto U_\infty^2$. The third time scale arises from viscous effects, especially responsible for the shear layer development. The following list summarizes the theoretical considerations and proposes hypotheses concerning the LEV development.

1. Similarity of an unsteady airfoil: Usually keeping the non-dimensional parameters constant (reduced frequency k, Strouhal number St, Reynolds number Re) and the effective angle of attack history $a_{eff}(t)$ results in the similarity of an unsteady airfoil. This is only true as far as global inviscid effects are considered, because these non-dimensional groups use the chord length or the plunging height as length scales. If viscous effects are taken into account, the shear layer thickness breaks the similarity, because it changes on another scale than the above mentioned non-dimensional numbers. If for two cases of an unsteady airfoil the chord length c is increased ten times, the free stream velocity U_∞ has to be decreased ten times. Although the exact shear layer thickness cannot be determined a priori, it will not increase with the same factor as the chord length, because for a laminar layer $d_{SL} \propto U^{-0.5}$ and for a turbulent layer $d_{SL} \propto U^{-0.2}$. In addition it is not clear if a transition in the vortex detachment mechanisms from the bluff body type to the eruption driven type occurs for an increased chord length. An additional non-dimensional parameter taking the viscous effects into account, especially the shear layer properties, is necessary to insure complete similarity, at least in a range of low Reynolds numbers, where viscous effects should be more influential.

2. Transition in LEV detachment mechanisms due to a varying chord length: There are basically two independent mechanisms, which may cause an LEV to detach from an unsteady airfoil. The first of this mechanisms is referred to bluff body vortex detachment mechanism and depends only on the inviscid global flow topology. The position of the rear reattachment point of the vortex determines, when counter rotating fluid is entrained from the trailing edge and transported upstream to the leading edge. The geometrical length (in this case the chord length) separating the shear layer and the layer of counter rotating fluid prior to their interaction and the subsequent LEV detachment is characteristic for this mechanism. Two limiting cases are imaginable. The chord length may either be decreased towards zero or towards infinity. For the former case, there is no running length over which a shear layer could form and an immediate interaction of the opposite shear-layers is possible. Therefore infinitely small LEVs form at a well-defined location and detach due to the bluff body vortex detachment mechanism. For the latter case, there is no interaction of both opposite shear layers, because the rear reattachment point never exceeds the trailing edge. For the latter case the convective time scale associated with inviscid effects is increased and therefore viscous effects dominate; the global flow topology does not change. Instead, with a growing LEV circulation, the boundary layer at the leading edge starts to separate from the airfoil surface due to a viscous/invscid interaction due to the effects described in paragraph 2.6.2, which causes the LEV to detach. Therefore a critical chord length $0 < c < \infty$ should exists (for constant k, St and a_{eff}-history), for which a transition in the vortex detachment mechanisms occurs. No experiments have been conducted to date to investigate this transition process or confine a region of non-dimensional parameters in which each mechanism determines LEV detachment. If the arguments of Betz (1950) and Prandtl (1927) presented in paragraph 2.3 are taken into account, then the ratio of LEV circulation and contained mass may be representative for the eruption driven detachment mechanism. The characteristic length scale determining this ratio is the shear layer. It is of interest if the shear layer parameter therefore serves as a characteristic length in the normalization of an LEV, when the trailing edge is not involved. Yarusevich (2009) uses scaling laws to non-dimensionalize the shedding frequency of vortices.

The non-dimensional shedding frequency is given by $f^* = \frac{f l_c}{U_\infty}$, with the shedding frequency f, the free stream velocity U_∞ and a characteristic length scale l_{char}. The non-dimensional shedding frequency scales in his case with $f^* \propto U^{-1.5}$, indicating that the characteristic length scale varies with $l_{char} = U_\infty^{-0.5}$.

3. Transition in vortex detachment mechanisms due to viscous effects: The Reynolds number defines the effect of viscous forces in a flow. As seen in the paragraph above the ratio of inviscid to viscous forces is likely to determine which LEV detachment mechanism occurs first. No matter which mechanism occurs first, the LEV detachment appears to be linked with the formation of full saddle point. Because there is a wide range of Reynolds numbers between helicopters and MAVs, it may in practice have an effect on the vortex formation for different cases. At small Reynolds numbers viscous effects are pronounced and the secondary vortical structures at the leading edge are more likely to form. The interaction of the shear layer with structures of opposite vorticity may cause the LEV to be cut from its feeding layer. For high Reynolds numbers these local structures are supposedly suppressed or delayed with respect to the stroke cycle, the LEV detachment is expected to occur due to the bluff body vortex detachment mechanism. For a given set of parameters a transitional Reynolds-number is proposed to exist: Below this Reynolds number the local flow topology at the leading edge changes due a separation of the boundary layer before the LEV rear reattachment point moves beyond the trailing edge. Above this number these changes are suppressed and the bluff body vortex detachment mechanisms limits the LEV growth.

4. Influence of the leading edge shape on the LEV formation: The leading edge has an influence on shear layer properties as shown in paragraph 2.3 and therefore effects the interactions of the secondary vortical structures with the shear layer. It can be expected that shear layers originating from a sharper leading edge are thinner and have an increased vorticity due to a higher pressure gradient when compared to shear layers originating from rounder leading edges. Such layers seem to be more resistant against the interaction with other

flow structures and should therefore result in an higher LEV circulation.

5. Influence of the different time scales on vortex formation: According to Baik *et al.* (2012) the reduced frequency changes the global flow topology. For low reduced frequencies the LEVs agree with the concept of optimal vortex formation, but this agreement ceases with increasing reduced frequencies. For a fixed vortex growth rate as stated by Roshko (1954) the stages of the airfoil motion and the effective angle of attack are shifted against the vortex formation stages with varying reduced frequency. For low reduced frequencies the maximum angle of attack during one stroke cycle occurs after the LEVs rear reattachment point has reached the trailing edge, the bluff body vortex detachment is supposed to cause LEV detachment. For high reduced frequencies the maximal angle of attack during one stroke cycle has already been bypassed before the LEV reaches its maximal size. Therefore the velocity difference over the shear layer decreases in later LEV stages, which decreases the LEV growth rate and promotes detachment. An optimal reduced frequency should exist, for which the LEV can accumulate maximal circulation. The peak in LEV formation is presumed to occur slightly after the maximal effective angle of attack has been reached in the stroke cycle, which is consistent with the findings of Milano and Gharib (2005), who find a maximal lift for a vortex detaching at a quarter of the stroke period.

6. Manipulation of the detachment process: If the mechanisms causing LEV detachment under defined flow conditions are understood, they may be manipulated with appropriate devices in order to prolong the LEV growth and therefore increase the LEV circulation; hence lift. As described in paragraph 2.6 both detachment mechanisms seem to be linked with the occurrence or motion of critical points, at which the flow velocity is near zero. This means that these points can readily be manipulated with small forcing. For efficiency considerations such a case is advantageous, because the global flow can be manipulated with only a small localized force. A DBD plasma actuator can be used to put a body force of small magnitude into the flow at critical points and observe the effect on the global flow, in order to

see if the detachment processes can be influenced.

7. Prediction of the LEV detachment mechanism: The LEV detaches from an airfoil analogously to vortices shedding from a bluff body, when its size is large enough to facilitate flow reversal at the trailing edge. If boundary-layer eruption occurs (either to a change in the local pressure gradient at the leading edge or an interaction between LEV and airfoil wall boundary layer), before flow reversal takes place, a transition in the detachment mechanisms can be expected. Therefore a parameter, which links the global flow parameters with the instantaneous causes of the LEV detachment mechanisms is suitable for predicting such a transition. The mass transfer from the shear layer into the LEV determines the instant, when flow reversal may occur. The area covered by the LEV as a result of its growth can be related to the airfoil chord. This ratio κ is given in equation 2.12 as such a parameter. If this area is sufficiently large, then flow reversal can occur for a given set of motion parameters. For large κ flow reversal is expected, for low κ eruption caused LEV detachment, with a transitional value κ_{trans} in between. Although this critical value is likely to depend on the shear layer thickness, the airfoil kinematics and the angle of attack history, it may be used to exemplarily predict the LEV detachment mechanism for a certain parameter space.

3 Experimental setup and analysis methods

The fundamental effects associated with the formation and detachment of vortices as described in chapter 2 are experimentally investigated by the observation of the flow field around simplified airfoil models. Particle image velocimetry (PIV) as an optical measurement technique is used to obtain time-resolved two-dimensional velocity fields. To create a distinct leading edge vortex, the airfoils execute an abstract pitching and/or plunging motion with high effective angles of attack. Flat plates are chosen to eliminate the effect of curvature induced pressure gradient. Distinct parameters like the chord length, the reduced frequency, the airfoil leading edge shape and the Reynolds number are varied to study their isolated influence on the growth and detachment behavior of the LEVs.
The majority of the experiments has been carried out in the open return windtunnel at the Technische Universität Darmstadt (TUDA); one measurement campaign was performed in the water tunnel of the university of Calgary. The windtunnel characteristics, the experimental rig and the measurement instrumentation are described in this chapter, the water tunnel description is given chapter 6.
Figure 3.1 shows the experimental setup in the windtunnel. Air flows into the test section from right to left in this figure. Linear actuators below the test section facilitate a two-degree of freedom pitching and/or plunging motion. The field of view (FOV) is subdivided into two parts, one global flow field and one flow field in the vicinity of the leading edge and is illuminated by a laser light sheet from downstream. Two cameras in front of the test section capture each field of view, the global flow field is observed directly, the local flow field via a mirror construction.

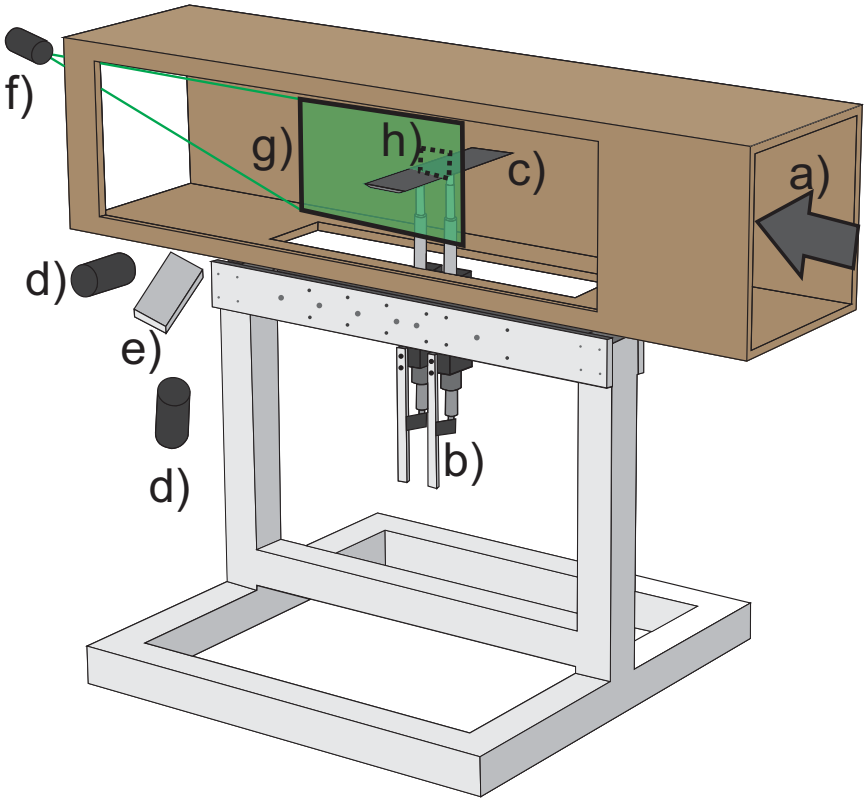

Figure 3.1: General experimental setup in the test section of the open return tunnel of the TUDA. The air flow direction is from right to left, indicated by the arrow. The components in the setup are: *a*) test section, *b*) linear actuators producing pitching and plunging motion, *c*) airfoil spanning from wall to wall, *d*) high speed CMOS cameras, *e*) mirror, *f*) light sheet optics. PIV Laser and laser beam extender are not shown.

3.1 Windtunnel properties

To realize unsteady effects such as the distinct formation of a leading edge vortex formation, the airfoils have to move sufficiently quick and their motion has to exhibit a large velocity with respect to the free stream flow. Therefore low free stream velocities are desired for the experimental investigation of unsteady aerodynamic effects.
A schematic view of the windtunnel and its varying cross sections from inlet (A) to outlet (after F) is given in figure 3.2. The inlet chamber has a cross section of 2.2 m $\times$ 2.2 m , a nozzle with a contraction ratio of 24 : 1 and a test section of 2 m length and a 0.45 m $\times$ 0.45 m cross section, followed by an impeller and an outlet diffusor. Five turbulence screens and a flow straightener are installed in the settling chamber and additional intakes with filter fleeces can be mounted to increase the pressure loss at the inlet.

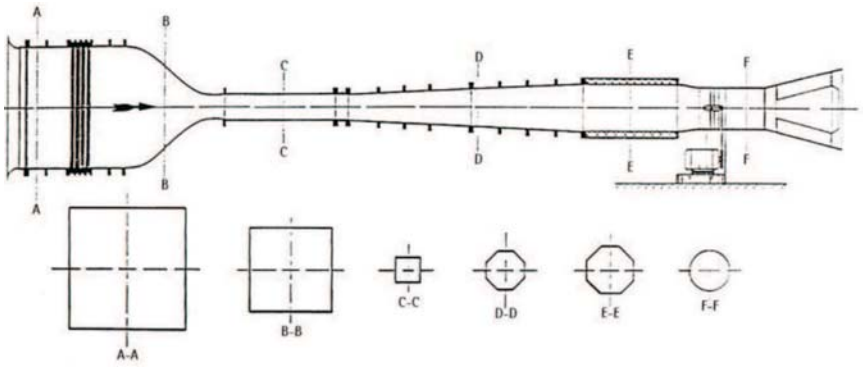

Figure 3.2: Schematic view of the open return windtunnel at TUDA. The cross sections are shown at settling chamber ($A - A$), nozzle ($B - B$), test section ($C - C$), and outlet ($D - D$) till ($F - F$).

3.1.1 Flow quality

To estimate the flow quality in terms of turbulence level and two-dimensionality for low free stream velocities preliminary measurements using hot wires and laser Doppler anemometry (LDA) were conducted. Free stream velocities

of $U_\infty = 1.5\ \frac{\mathrm{m}}{\mathrm{s}}$ and $U_\infty = 4.0\ \frac{\mathrm{m}}{\mathrm{s}}$ were selected. The free stream velocity necessary for the experiments is not expected to be lower than $U_\infty = 1.5\ \frac{\mathrm{m}}{\mathrm{s}}$ or above $U_\infty = 4.0\ \frac{\mathrm{m}}{\mathrm{s}}$. For free stream velocities $U_\infty > 4.0\ \frac{\mathrm{m}}{\mathrm{s}}$ the flow quality is expected to improve.
A rake holding 17 hot wire probes was placed in the test section 1 m downstream of the section entrance in the middle of the windtunnel height. The probes were custom made of 10 μm tungston wire, their signal was processed by a custom made 64-channel CTA system used and described by Reeh (2014) for inflight measurements. The probes were calibrated using a Pitot probe. The hot wires simultaneously collect data at a sample rate of $10,000$ Hz over a period of 30 s. The probes were distributed from wall to wall ($-0.4 < \frac{y}{h_{WT}} < 0.4$) to check if two-dimensional conditions prevail in the test section and to estimate the turbulence level. The turbulence level is defined as $Tu = \frac{1}{U_\infty}\sqrt{\overline{u'^2}}$, with the velocity fluctuations $\overline{u}'$ defined as $\overline{u'^2} = \frac{1}{n-1}\sum_{i=1}^{n}(\overline{U} - U_i)^2$, with the number of samples n, U_i as the instantaneous velocity and $\overline{U}$ as the mean velocity in streamwise direction at each measurement point.
The results of the hot wire measurements are shown in figure 3.3. The time-averaged velocity profiles $\overline{U}$ are given as a solid line and the fluctuation level is given by the root mean square (RMS) value $\sqrt{\overline{u'^2}}$ as error bars. Figure 3.3 (a) shows the case for $U_\infty = 1.5\ \frac{m}{s}$, figure 3.3 (b) for $U_\infty = 4.0\ \frac{\mathrm{m}}{\mathrm{s}}$. In both cases the turbulence level varies between $Tu = 0.5 - 2.0$ %. At both speeds the mean velocity varies less than 12 % across the test section width.

The LDA system was traversed at a measurement plane 500 mm downstream of the test section entrance. The signal was acquired by a *Dantec FlowExplorer* LDA and processed with a *Dantec BSA F*30 processor *DEHS* droplets were used as seeding, introduced in the settling chamber of the windtunnel. Figure 3.4 schematically indicates the LDA measurement points. The streamwise coordinate x and its respective velocity component U is directed into the image plane in this figure. The velocity component V points along the coordinate y, W along z. The LDA system records U and W. The cross section is not completely optically accessible, only a part of the cross section from the viewing window to the middle of the test section was covered. The data were sampled at approximately 1000 Hz over a period of 30 seconds.

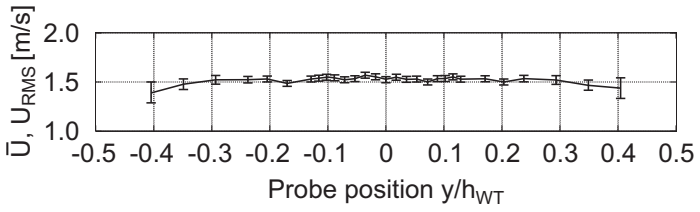

(a) $U_\infty = 1.5\ \frac{m}{s}$

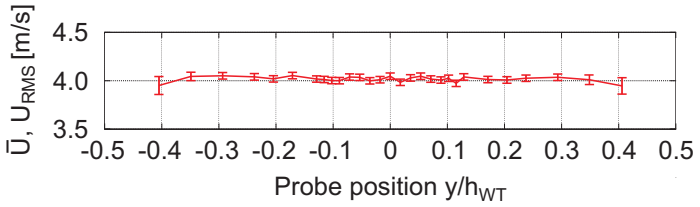

(b) $U_\infty = 4.0\ \frac{m}{s}$

Figure 3.3: Time averaged velocity profile $\overline{U}$ and fluctuation level $\sqrt{\overline{u'^2}}$ measured with the hot wire rake for nominal free stream velocities of $U_\infty = 1.5\ \frac{m}{s}$ and $U_\infty = 4.0\ \frac{m}{s}$

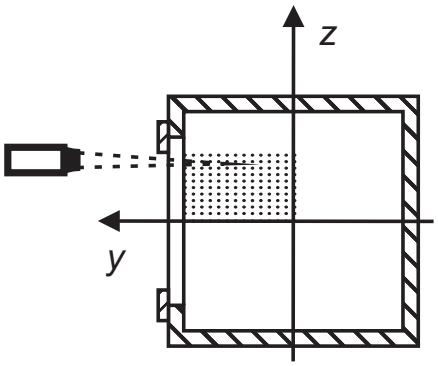

Figure 3.4: Measurement points of the LDA system

The results of the LDA measurements are shown in figure 3.5 over y and z normalized with the windtunnel height h_{WT}. The upper half of

figure 3.5 shows the velocity profiles normalized with the nominal flow speed $U(y,z)/U_\infty$, the lower half shows the turbulence level distribution $Tu = \frac{1}{U_\infty}\sqrt{0.5(\overline{u'^2} + \overline{w'^2})}$, with the velocity fluctuations $\overline{w'}$ and $\overline{u'}$ defined analogously to the hot wires. In the left half the nominal flow velocity was set to $U_\infty = 1.5\ \frac{\mathrm{m}}{\mathrm{s}}$, in the right half to $U_\infty = 4.0\ \frac{\mathrm{m}}{\mathrm{s}}$.

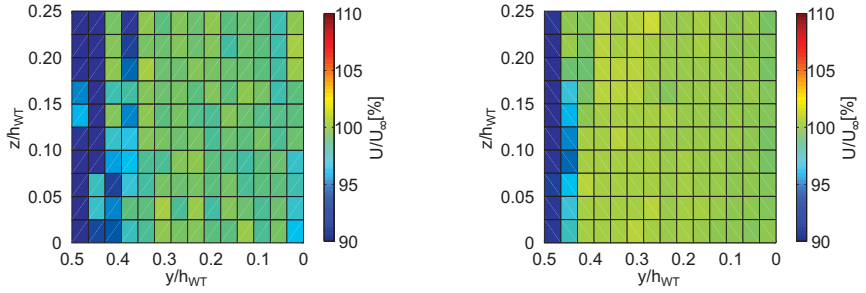

(a) $\frac{U(y,z)}{U_\infty}$ at $U_\infty = 1.5\ \frac{\mathrm{m}}{\mathrm{s}}$

(b) $\frac{U(y,z)}{U_\infty}$ at $U_\infty = 4.0\ \frac{\mathrm{m}}{\mathrm{s}}$

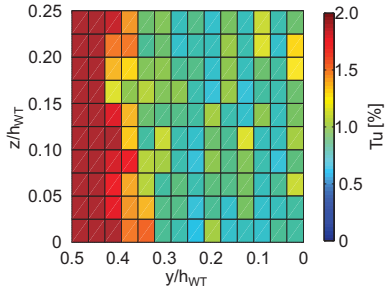

(c) $Tu(y,z)$ at $U_\infty = 1.5\ \frac{\mathrm{m}}{\mathrm{s}}$

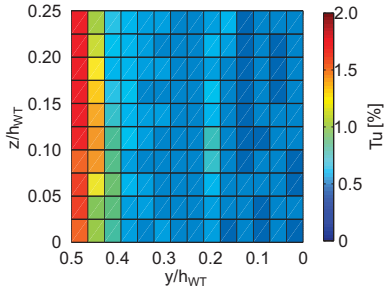

(d) $Tu(y,z)$ at $U_\infty = 4.0\ \frac{\mathrm{m}}{\mathrm{s}}$

Figure 3.5: Velocity and turbulence distributions in the measurement plane in (y,z) coordinates measured with the LDA system. $y/h_{WT} = 0$ and $z/h_{WT} = 0$ mark the wintunnel center, $y/h_{WT} = 0.5$ marks the wind tunnel wall. $z//h_{WT} = 0.25$ marks the upmost measurement ponits

In the free stream ($y/H_{WT} < 0.35$) the velocity matches the nominal values of $U_\infty = 1.5\ \frac{\mathrm{m}}{\mathrm{s}}$ and $U_\infty = 4.0\ \frac{\mathrm{m}}{\mathrm{s}}$, while the wall influence decreases the streamwise velocity for the outer parts of the test section. The turbulence level is of the order of magnitude of $Tu = 1 - 2\%$ in the free stream, but increases towards the outer parts of the windtunnel near the side walls. As expected the velocity profile at $U_\infty = 4.0\ \frac{\mathrm{m}}{\mathrm{s}}$ is more uniform, the turbulence level lower and thus the flow quality higher than for $U_\infty = 1.5\ \frac{\mathrm{m}}{\mathrm{s}}$. The measured turbulence level matches for both measurement methods (hot wires and LDA) and corresponds to the turbulence level measured by Rival (2009) in the same windtunnel, although the measurement range was significantly reduced to lower free stream velocities.

3.2 Experimental rig and airfoil kinematics

The principle airfoil kinematics are schematically shown in figure 3.6 for an early instant in the airfoil motion period t_1 and a later instant t_2. The airfoil pitching and plunging kinematics are produced by two linear actuators of the type $LinMot\ PS01-48x240F-C$. Their maximal stroke is 240 mm and their maximal stroke speed is 1.7 $\frac{\mathrm{m}}{\mathrm{s}}$ with a position repeatability of ± 0.5 mm given by the manufacturer. The actuators can be controlled and configured by the manufacturer's $LinMot\ LinTalk$ software. The synchronization between the PIV system and the airfoil motion is facilitated with $LabView$ software and a $National\ Instruments$ DAQ board of the type USB 6259 as an interface communicating with the $LinMot\ LinTalk$ control software via $RS232$ ports and directly triggers both laser cavities and the camera acquisition by USB signals. The heights of the airfoil at the leading and the trailing edge are denoted by h_1 and h_2. The geometrical angle of attack results from a vertical height difference between h_1 and h_2.

The effective angle of attack α_{eff} is a result of the combined pitching and plunging motion, given by equation 3.1 with α_{geo} as the geometrical angle of attack due to the pitching motion and α_{plunge} due to the airfoil motion.

$$\alpha_{eff}(t) = \alpha_{geo}(t) + \alpha_{plunge}(t) \tag{3.1}$$

As described by Davids (1999) the pitch rate $\dot{\theta}$ has an influence on the effective angle of attack, when the non-dimensional pitching location s_{pivot}

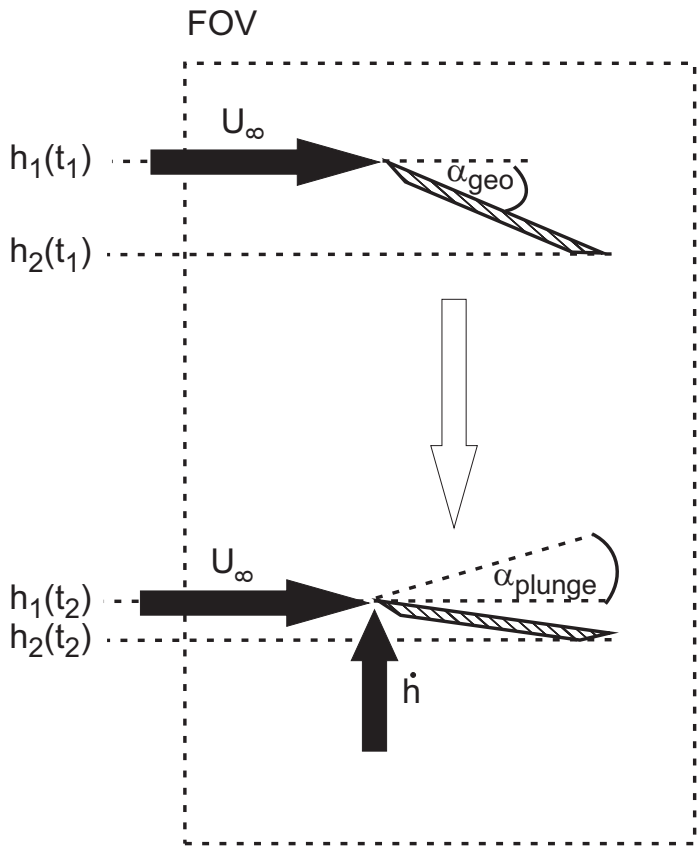

Figure 3.6: Schematic airfoil kinematics with the height of the leading edge h_1 and the trailing edge h_2, the plunging velocity $\dot{h}$, geometric angle of attack α_{geo}, the plunging induced angle α_{plunge} and the free stream velocity U_∞. Adapted from Widmann and Tropea (2015)

is downstream of the leading edge and introduces an additional velocity component besides the plunging velocity $\dot{h}_1 = \frac{\partial h_1}{\partial t}$ to the leading edge region, which can be described by equation 3.2:

$$\begin{aligned}\alpha_{eff}(t) &= \alpha_{geo} + \alpha_{plunge} \\ &= \alpha_{geo} + tan^{-1}(\frac{\dot{h}_1 + cs_{pivot}\dot{\theta}cos(\theta)}{U_\infty - cs_{pivot}\dot{\theta}sin(\theta)})\end{aligned} \tag{3.2}$$

The pivot location was selected at the leading edge with $s_{pivot} = 0$ to exclude pitch rate effects and reducing equation 3.2 to:

$$\alpha_{eff}(t) = \alpha_{geo} + tan^{-1}(\frac{\dot{h}_1}{U_\infty}) \tag{3.3}$$

The plunging part contributing to the effective angle of attack is given by the sinusoidal plunging motion $h_1(t)$. The geometric angle of attack is then calculated for the combined pitching and plunging cases as $\alpha_{geo} = \alpha_{eff,max} - tan^{-1}(\frac{\dot{h}_1(t)}{U_\infty})$ to produce a sinusoidal angle of attack history. The height difference $\Delta h(t) = h_1(t) - h_2(t)$ is in turn determined by the $\alpha_{geo} = tan^{-1}\Delta h x_{spacing}$, with $x_{spacing}$ as the fixed spacing of 80 mm between the linear actuators in the streamwise direction. The maximum blockage during the combined pitch and plunge motion did not exceed 5.6 % for $\alpha_{eff,max} = 30°$, for a pure pitching motion with a maximum geometrical angle of attack of $\alpha_{eff,max} = 30°$ the blockage was 12.3 %.

3.3 Airfoil shape

Interchangable airfoils were used to investigate the influence of their chord length. For all experiments conducted in the windtunnel flat plates with sharp leading and trailing edges were selected, but four different chord lengths of $c = 90$ mm, $c = 120$ mm, $c = 150$ mm and $c = 180$ mm were used. The airfoils thickness of $d = 5$ mm and the leading edge shape with an angle of $\theta = 30°$ were kept constant for all profiles (see figure 3.7).

As discussed in paragraph 2.3 the LEV formation and detachment is likely to be influenced by the pressure gradient on the airfoil surface. For the most simple case of a flat plate, the effects induced by the cambering can be excluded and one parameter effecting LEV formation can be eliminated.

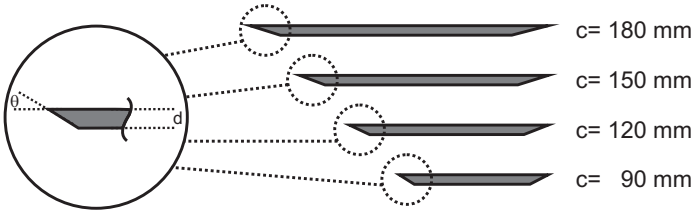

Figure 3.7: Schematic description of the airfoils, adapted from Widmann and Tropea (2015)

According to the considerations of Prandtl (1927) the flow separates immediately at sharp leading edges and the LEV formation sets in at a well defined location for all observed experimental parameters. The shear layer separation location is therefore not influenced by the flow parameters Re, St, k and α_{eff}. The influence of a variation of these parameters on the LEV evolution is then independent of the separation location and an isolated parameter change can be investigated. Using this simple plate geometry ensures well-defined boundary conditions and inter-parameter comparability of the individual experiments. The outer shape of the airfoil is depicted in figure 3.7.
To ensure nominally two-dimensional flow conditions, the airfoils spans from wall to wall with a gap of less than 2 mm between the airfoil edge and the tunnel wall. Their insides were hollow to reduce the inertial mass and stiffened using spanwise ribs to prevent vibrations. A rapid prototyping machine was used to sinter the complex inner geometry of the airfoils. Before using the airfoils in the windtunnel, their surfaces were polished and varnished in black, to reduce reflections from the laser light sheet during the PIV experiments.

3.4 Measurement instrumentation

3.4.1 Smoke flow visualization

Prior to the quantitative PIV experiments smoke flow visualizations were conducted to assess the unsteady LEV behavior and the secondary struc-

tures evolving at the leading edge. Therefore smoke was introduced to the air flow by evaporating baby oil from a heated wire. The wire was stretched vertically across the test section 100 mm upstream of the leading edge at quarter span position. The wire consisted of constantan with an electric resistance of 28 $\frac{\Omega}{\mathrm{m}}$ and a diameter of 0.15 mm. Insulating fasteners were place at a distance of 0.5 m slightly above and below the test section and an electric potential of 18 V was applied to heat the wire by a DC laboratory power supply. The smoke sheet was illuminated by a metal halogen lamp with a power of 300 W from above and recorded by a *Phantom v*12.1 high speed CMOS cameras with a resolution of 1280 $\times$ 800 pixels at an acquisition frame rate of 1 kHz. A lense with a focal length of 50 mm was chosen and the camera exposure time was set to 0.6 ms. A stable smoke sheet could be produced up to free stream velocities of $U_\infty = 6\frac{\mathrm{m}}{\mathrm{s}}$.

3.4.2 Particle Image Velocimetry

The LEV development is studied using particle image velocimetry (PIV) under simplified conditions with abstracted airfoil kinematics and flat plates, in order to understand the isolated vortex behavior and identify independent influencing parameters. The Focus of research lies on the detachment timing of the LEVs and the mechanisms limiting LEV size and circulation and their influencing parameters. PIV is used to record two-dimensional velocity fields and to study the LEV behavior. The PIV system consists of one dual cavity *Litron LDY* $-$ 303 high speed Nd:YLF laser with a wavelength of $\lambda = 527$ nm, two *Phantom v*12.1 high speed CMOS cameras with a resolution of 1280 $\times$ 800 pixels, light sheet optics installed at the ceiling of the windtunnel and a beam extender, which guides the beam from the laser outside the windtunnel to the light sheet optics. The assembly of these components is shown in figure 3.1, the laser and the beam extender are not shown. The green shaded area indicates the illuminated region of the windtunnel, the solid black rectangle around the airfoil shows the global field of view. Inside of this global field of view is a dashed box. This dashed box indicates a smaller local field of view to better resolve the emerging secondary structures near the leading edge. While the global field of view is recorded directly, the local field of view is recorded via a mirror installed in front of the test section.
Time resolved data were acquired and processed. For the combined pitch-

ing and plunging experimental cases with one field of view (FOV) and one camera (as shown in figure 3.1 g), a Nikkor 60 mm$f/2.8$ lens was used. For the pure pitching experimental cases two fields of view were simultaneously captured: for the global FOV (as shown in figure 3.1 g)), a Nikkor 60 mm $f/2.8$ lens was used and for the local field of view (as shown in figure 3.1 h)), a Nikkor 110 $mmf/2.8$ lens was used. In all cases an optical filter with a wavelength of 527 nm corresponding to the laser light were mounted on the cameras to reduce reflections and ambient light.
For the combined pitching and plunging cases the cameras covered a FOV with the sizes of $\frac{x}{c_{max}} = 2.2$ in streamwise direction and $\frac{y}{c_{max}} = 2.67$ perpendicular to the streamwise direction with respect to the largest chord length of $c_{max} = 180$ mm. In cases of two FOVs a pure pitching cases is investigated, since the local FOV at the leading edge covers a small area and needs to be observed over an entire stroke cycle. The airfoil would quickly pass that small FOV for a plunging motion and the flow evolution at the leading edge could only be captured during a short period of the stroke cycle. The global FOV has the dimensions of $\frac{x}{c} = 2.9$ and $\frac{y}{c_{max}} = 2.0$ with respect to a chord length of $c = 120$ mm. The local FOV has the dimensions of $\frac{x}{c} = 0.5$ and $\frac{y}{c_{max}} = 0.345$. The largest FOV has an area of 0.0322 m^2. To illuminate the FOV a laser light sheet of 3 mm thickness was positioned in streamwise direction at 18 % of the span width using a light sheet optic, as shown in figure 3.1. The laser beam was led from the outside of the windtunnel to the light sheet optics using a beam extender in order to prevent open light paths. The sheet optic was placed inside the windtunnel downstream of the airfoil in order to reduce the divergence of the laser sheet to a minimum. The laser was operated at the highest output of 21 mJ pro pulse and data were acquired at a laser repetition rate of 1 kHz. The DEHS seeding particles were introduced into the settling chamber and had a mean diameter of $d_{DEHS} = 0.5 - 1.5$ μm according to Raffel, Willert, Wereley and Kompenhans (2007) and a density of $\rho_{DEHS} = 910$ $\frac{kg}{m^3}$. The response time $\tau_s = d^2_{DEHS}\rho_{DEHS}/18\mu = 2.7\mu s$ of the particles was computed according to Raffel, Willert, Wereley and Kompenhans (2007). μ represents the dynamic viscosity of the air flow. To estimate, if the inertia of the seeding particles is sufficiently low for the conducted measurements, its response time has been compared to a typical flow time τ_F. This flow time was conservatively estimated as the convective time of the Kolmogorov length scale η_K and reads $\tau_F = \eta_K/U_\infty$. The

Kolmogoroy length scale was estimated to be $\eta_K = c \times Re^{-\frac{3}{4}} \approx 60\ \mu m$, with c as the chord length representing the global length scale. For the highest used flow velocity τ_F amounts to 20 μs, which is large compared to the response time. DEHS is therefore assumed to follow the air flow sufficiently. The area upstream of the leading edge and below the solid airfoil was masked because of insufficient illumination. Early in the stroke cycle the airfoil suction surface was hidden due to parallax.
The raw data were recorded in the double-frame mode with a pixel depth of 12 *bit* and correlated with a stepwise refinement scheme of the interrogation area (IA) and an overlap of 50 %, beginning with an IA of 64 $\times$ 64 pixels and ending with an IA 16 $\times$ 16 pixels. According to the manufacturer a particle displacement of 0.1 $pixels$ can be resolved.
The maximal interrogation size was selected by the need to resolve local velocities, which may be significantly larger than the undisturbed free stream velocity. In this case the maximal velocity was set to $U_{max} = 10 \times U_\infty$. As a rule of thumb the correlation works most reliable if a particle displacement of $\frac{1}{4} - \frac{3}{4}$ IA is ensured. The time between the two frames Δt_{frames} has been set in such a way to ensure a displacement of approximately 20 particles under consideration of the conversion factor between physical image plane and camera sensor $f_{conversion}$ for U_{max} in order to fulfill the rule of thumb for an IA size of 64 $\times$ 64 pixels. With a conversion factor of $f_{conversion} = 0.0203\ \frac{\mathrm{mm}}{pixel}$ the time between the two frames was set to $\Delta t_{frames} = 170\ \mu \mathrm{s} \frac{\mathrm{m}}{\mathrm{s} U_\infty}$ depending on the free stream velocity. To determine the smallest IA size three correlation schemes with a stepwise reduction of the IA size have been executed for the same raw data, beginning with an IA of 64 $\times$ 64 pixels but ending at an IA size of 32 $\times$ 32 pixels, 16 $\times$ 16 pixels and 8 $\times$ 8 pixels respectively.
While the spatial resolution increases with decreasing IA size, their reliability ceases, because the displacement of the seeding particles exceeds the IA size and no corresponding particles can be correlated in two consecutive frames. Therefore a compromise between spatial resolution and reliability has to be found. The manufacturer states that a ratio of 1 : 2 or higher between the two largest correlation peaks insures reliable results: local velocity vectors below that limit are considered invalid. For all three correlation schemes the mean correlation height, the percentage of invalid vectors in the velocity field and the spatial resolution have been recorded to estimate their respective performance. The result is summarized in table 3.1. Note that the vectors below the airfoil were masked and are not

Table 3.1: Comparison of the three correlation schemes with different minimal IA size

minimal IA size [*pixels*]	32 × 32	16 × 16	8 × 8
spatial resolution	63 × 49	128 × 99	256 × 199
masked out vectors	1075	5396	16887
mean correlation height ratio	2.94	2.74	0.79
invalid vectors	127 $\hat{=}$ 6.3 %	494 $\hat{=}$ 6.8 %	5143 $\hat{=}$ 15.1 %

considered for determining the minimal IA size.

While the percentage of invalid vectors and the mean correlation height drops only slightly from a minimal IA size of 32 × 32 to 16 × 16, the spatial resolution is doubled in each direction. in both cases the mean correlation height ratio is more than twice the required value for valid data. The same improvement of spatial resolution is obtained from a minimal IA size of 16 × 16 to 8 × 8, but the percentage of invalid vectors increases drastically and the mean correlation height ratio falls significantly below the boundary of being valid. As a compromise a minimal IA size of 16 × 16 pixels was chosen.
With these parameters the lowest resolvable velocity U_{min} can be estimated according equation 3.4. Approximately six percent of the free stream velocity (corresponding to the measurement uncertainty) $\frac{U_{min}}{U_\infty} = 0.015$ can be resolved. The vorticity is in a two-dimensional flow field defined as $\omega = \frac{\partial V}{\partial x} - \frac{\partial U}{\partial y}$ and can be obtained from the discrete data by calculating the curl $\omega = \frac{V_i - V_{i-1}}{\Delta x} - \frac{U_j - U_{j-1}}{\Delta Y}$ with $i, i-1, j$ and $j-1$ as neighboring points and ΔX and ΔY as the grid spacing. According to Raffel, Willert, Wereley and Kompenhans (2007) the uncertainty of the normalized vorticity $\Delta\omega$ can be calculated with the linear error propagation if the assumptions of weakly correlated neighboring data holds. For a low overlap (50 % or less) and a coarse spacing, as for the given cases, the neighboring data are only weakly correlated. Therefore the vorticity uncertainty amounts to $\frac{\Delta\omega c}{U_\infty} = 0.76$ for the most unfavorable experimental case with the maximal chord length $c = 180$ mm and the lowest flow velocity $U_\infty = 1.5\ \frac{\mathrm{m}}{\mathrm{s}}$.

$$
\begin{aligned}
U_{min} &= 0.1\ pixel\ * f_{conversion}/\Delta t_{frames} \\
&= 0.1\ pixel\ * f_{conversion} * U_\infty \frac{\mathrm{s}}{\mathrm{m}} \frac{1}{170\ \mu\mathrm{s}} \\
\frac{U_{min}}{U_\infty} &= 0.015
\end{aligned}
\tag{3.4}
$$

Outliers were defined as vectors, whose deviation from the mean in a 3 $\times$3 neighborhood was six times larger than the standard deviation. These spurious vectors were removed applying a 3 $\times$3 median filter. No more than 10 % of the vectors were affected by the outlier detection.
For the experiments with a pure pitching motion a mirror has been added to the setup in order to enable a simultaneous recording of a local FOV and a global FOV using two cameras. The flow is recorded using the two fields of view (FOV) of the PIV system, as described in section 3.4.2. The setup is shown schematically in figure 3.8.

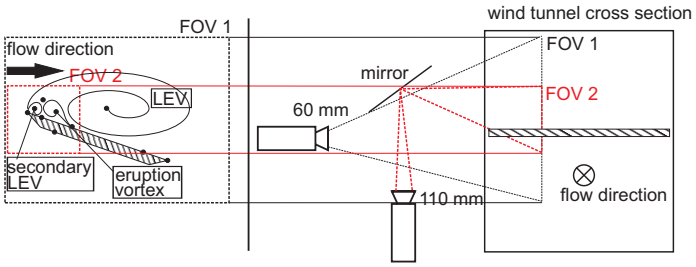

Figure 3.8: Schematical setup of the cameras recording the two FOVs

On the left hand side a lateral view of the expected flow field around a pitching flat plate in the wind tunnel is given. The two separate fields of view are indicated by a black (FOV 1) and a red frame (FOV 2). The flow structures in each FOV are schematically shown, critical points are depicted as black dots. While FOV 1 covers the global flow field around the pitching flat plate, FOV 2 is limited to near the leading edge to resolve more details. On the right hand side the corresponding experimental setup around the wind tunnel is shown, the viewing direction is downstream (with the flow pointing into the pitured plane). Again, FOV 1 is

indicated by a black frame and FOV 2 by a red frame. While FOV 1 is recorded directly, a mirror is tilted about 45° and projects FOV 2 into the second camera. The global field of view is recorded directly with an objective with a focal length of 60 mm. The local field of view is recorded through a mirror using an objective with a focal length of 110 mm.

3.5 Repeatability and two-dimensionality

For each set of experimental parameters, five repetitions were performed. The five single experimental runs were analyzed separately and the results averaged. Doing so requires sufficient repeatability of the single experimental runs. An example of these five runs for a pitching and plunging flat plate at a free stream velocity of $U_\infty = 1.5\frac{\mathrm{m}}{\mathrm{s}}$ and a chord length of $c = 180$ mm is exemplarily given in figure 3.9 for a non-dimensional instant of $t/T = 0.22$ in the stroke cycle T. This example was chosen because of the lowest free stream velocity of $U_\infty = 1.5\frac{\mathrm{m}}{\mathrm{s}}$, which is expected to be the least repeatable case.

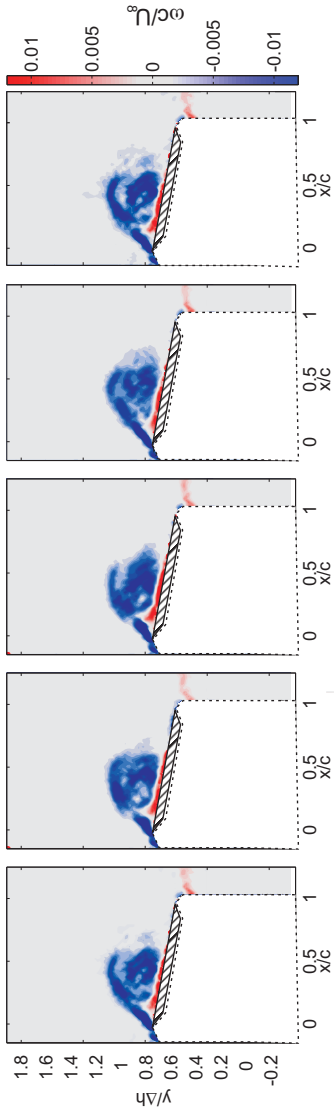

Figure 3.9: Comparison of five independent experimental runs at $U_\infty = 1.5\frac{\mathrm{m}}{\mathrm{s}}$ and $c = 180$ mm for a non-dimensional instant of $\frac{t}{T} = 0.22$. The normalized vorticity $\omega c/U_\infty$ is shown color coded.

In figure 3.9 the five runs are arranged horizontally, the normalized vorticity $\frac{\omega c}{U_\infty}$ (negative vorticity as blue, positive vorticity as red) and the instantaneous streamlines are shown. The x and y axes are normalized by the chord length c and the plunging height Δh respectively. The contour and the masked out area are schematically shown. In each run a distinct LEV, represented by an accumulation of negative vorticity, develops above the airfoil. Vortex size and center match in all cases, qualitatively indicating repeatability.
To quantitatively estimate the repeatability after processing the data the standard deviation $\sigma_{U,V}(x,y) = \sqrt{(\sigma_U^2(x,y) + \sigma_V^2(x,y))}$ of the flow magnitude is calculated at each spatial point x, y over all five runs. The normalized standard deviation $\sigma_{U,V}(x,y)/U_\infty$ is then shown for the above mentioned case in figure 3.10 , overlaid with the mean velocity vectors at each second spatial point. The figure is taken at a non-dimensional instant of $\frac{t}{T} = 0.30$, after the expected LEV detachment, when the standard deviation is expected to be largest.

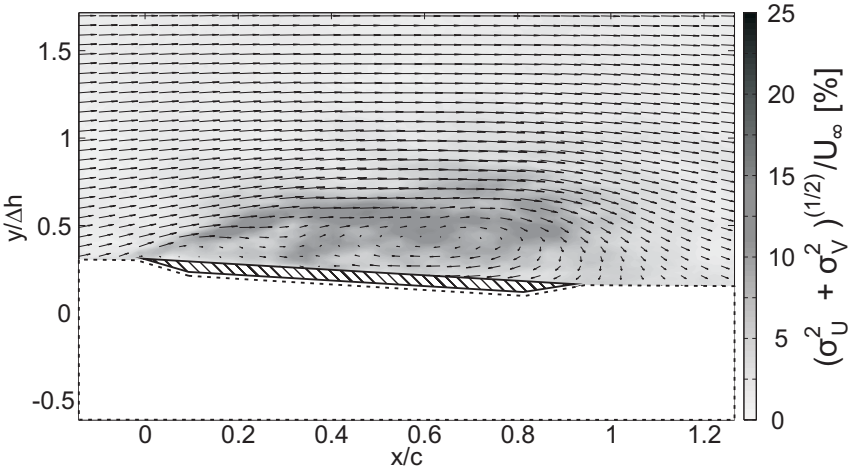

Figure 3.10: Normalized standard deviation $\sqrt{(\sigma_U^2(x,y) + \sigma_V^2(x,y))/U_\infty}$

The standard deviation is shown in the most interesting region just above the airfoil, the area below the airfoil has been masked out. The largest

run-to-run deviations are found inside the LEV and the shear layer, while the are near wall region and the free stream show little deviations. The mean standard deviation over the whole field of view is calculated as $\overline{\sigma}_{U,V} = \frac{1}{N}\sum_{i=1}^{N}\sigma_{U,V}(i)$ with i indicating each spatial point and N as the number of valid spatial points in figure 3.10 amounts to $\overline{\sigma}_{U,V}/U_\infty = 6.4$ %. This value has been calculated for all experimental cases of combined pitching and plunging motions and pure plunging motions. For the combined pitching and plunging motion this mean standard deviation lies in a range of $\overline{\sigma}_{U,V}/U_\infty = 4.3 - 6.5$ % and is somewhat larger for global FOV of the pure pitching experiments with $\overline{\sigma}_{U,V}/U_\infty = 6.6 - 8.8$ %. Given the small free stream velocities, these flow conditions are considered as repeatable.
For the conducted experiments with prevailing unsteady conditions with reduced frequencies of $k > 0.1$ wall effects are negligible, since Carr *el al.* (1977) find only marginal wall effects for their airfoils with an aspect ratio of $AR = 1.6$ at $Re = 2 * 10^6$ and Maresca *el al.* (1979) show that wall effects for their airfoil with an aspect ratio of $AR = 2$ at $Re = 57\ 000$ do not alter their results for reduced frequencies $k > 0.11$. The airfoils used in this experimental campaign have a minimum aspect ratio of $AR = 2.44$ and a minimum reduced frequency of $k = 0.16$ is tested, therefore wall effects are not expected to effect the experimental results.

To test for two-dimensional flow behavior, the test case with the largest aspect ration and hence the highest expected three-dimensional effects and spanwise cross flows has been investigated using smoke flow visualizations. The chord length is 180 mm and the airfoil spans from wall to wall, which are $s = 450\,mm$ apart. The aspect ratio for the respective case is $AR = 2.5$, the Reynolds number is $Re = 17\,000$, the reduced frequency is $k = 0.5$ and the Strouhal number is $St = 0.25$. A smoke sheet was introduced at seven different spanwise positions over one half of the airfoil as schematically shown in figure 3.11.

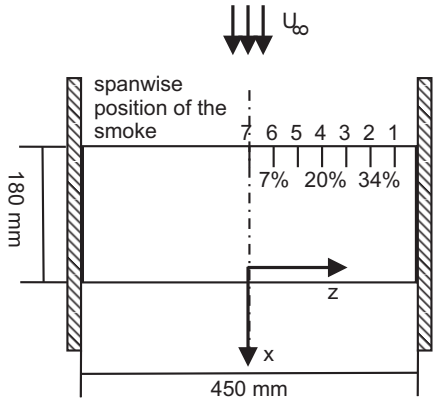

Figure 3.11: Schematic description of the smoke visualization setup. The streamwise coordinate is denoted by x, the spanwise coordinate is denoted by z. The spanwise positions, where smoke was introduced is marked by numbers from 1 to 7. Incoming flow is denoted by U_∞

The global flow field behavior and the spanwise variation of the leading edge vortex at the spanwise positions 2, 4 and 6 (at 34 %, 20 % and 7 % respectively of the span outboard of the airfoil center) have been investigated by placing the camera perpendicular to the smoke sheet. Figure 3.12 shows snapshots of the vortex evolution for instant in the motion cycle of $t/T = 0.22$. It can be seen, that the global flow field and the LEV evolution do not vary significantly in spanwise position.

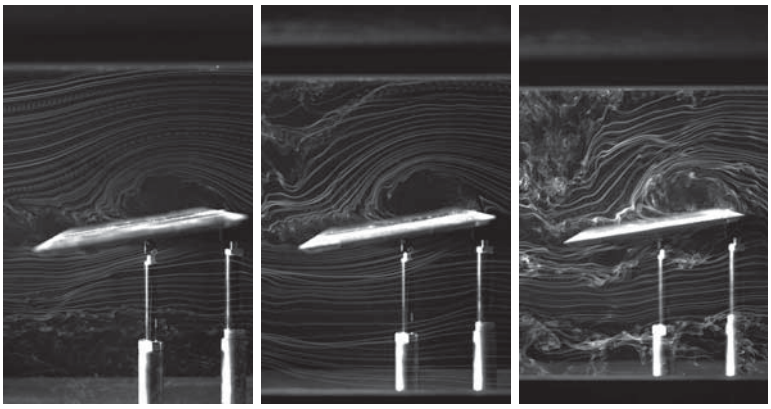

(a) spanwise position 6 (b) spanwise position 4 (c) spanwise position 2

Figure 3.12: Smoke flow visualization at the spanwise positions 2, 4 and 6 in sideview at $t/T = 0.22$

To uncover crossflow components of the flow field, the camera has been placed downstream of the airfoil to investigate the spanwise deviations of the smoke. Additionally, a polyamide powder with a mean particle diameter of 45 μm and a density of 9 $\frac{g}{cm^3}$ has been spread near the leading edge. The movement of the powder indicates spanwise velocity components. Figure 3.13 shows the smoke sheets at three spanwise positions at an instant in the motion cycle of $t/T = 0.28$. Due to the fixed camera position, the spanwise postions are recorded under a different perspective.

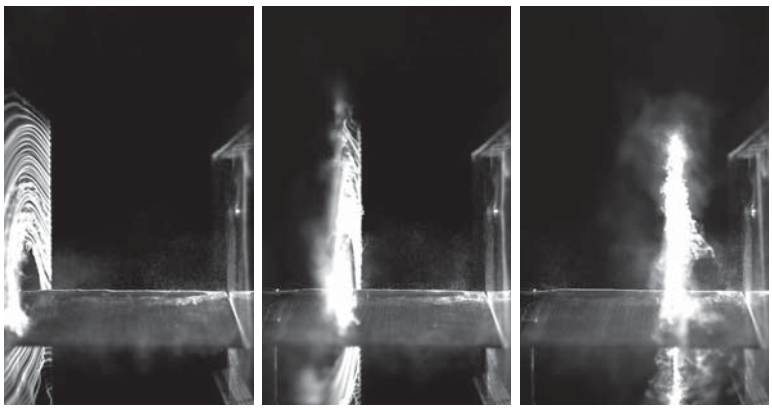

(a) spanwise position 6 (b) spanwise position 4 (c) spanwise position 2

Figure 3.13: Smoke flow visualization at the spanwise positions 2, 4 and 6 in rear view at $t/T = 0.28$

The smoke sheet remains in a plane during the motion cycle, only small potions of smoke are carried outboard of the airfoil. The powder does not exhibit a perceptual spanwise motion. Except of the airfoil corners the powder creates a two-dimensional distribution after the motion. Therefore the flow is considered two-dimensional, at least in the airfoil section near the center (between spanwise position 2 and 6), where the PIV measurements were carried out. All other experimental cases were considered as two-dimensional since they are less perceptive for cross flows and three-

dimensional effects, since their aspect ratio is larger.

3.6 Analysis methods

From the time resolved velocity fields different quantities can be extracted to evaluate the LEV formation behavior and the LEV detachment mechanisms. Besides the application of topological concepts (introduced in section 2.5) to the flow field, quantitative values are extracted using vortex identification methods and methods for the identification of critical points. The most important of these quantities are the circulation of the LEV Γ^{LEV} and the TEV Γ^{TEV}, the circulation of the secondary vortex emerging at the leading edge due to the boundary layer eruption $\Gamma^{Eruption}$, the circulation of the secondary LEV $\Gamma^{sec.LEV}$, the streamwise position of the rear reattachment point of the LEV on the airfoils suction side X_{SP} and the trajectory of the LEV center x_{LEV} and y_{LEV}.
In a first step these quantities are calculated for the independent experimental runs, then the average and the standard deviation is calculated. In order to preserve small scale structures at the leading edge, the single time resolved velocity fields are not averaged over the five independent runs.
The Γ^{LEV} curve represents the evolution of the LEV over the stroke cycle. LEV detachment is defined according to Fage and Johansen (1928), when the LEV does not accept any more vorticity from its feeding shear layer and its circulation exhibits a peak or plateau. This instant may then be connected with the occurrence of other flow features
The LEV rear stagnation point X_{SP} is a measure of the LEV size and therefore the global flow topology. As soon as the LEV rear stagnation point moves beyond the trailing edge, a full saddle forms above the trailing edge and enables flow reversal at the trailing edge. As seen from section 2.6.1 this flow reversal is the onset of the bluff body LEV detachment mechanism. With this formation of a full saddle and flow reversal at the trailing edge a TEV is generated. Due to the circular motion of the fluid at the trailing edge the TEV rolls up. The LEVs rear stagnation point XSP can indicate the global flow topology and the instant in time, when the bluff body detachment mechanism is triggered and therefore if the chord length is characteristic for LEV detachment.
The formation of the TEV is directly linked to the size of the LEV and its rear reattachment point. A rise in the Γ^{TEV} curve indicates a changed

flow topology at the trailing edge due to the excess of X_{SP} beyond the airfoil chord.
The $\Gamma^{Eruption}$ curve represents the evolution of the secondary structures near the leading edge due to the boundary layer separation. A sudden rise in this curve indicates the instant, when the boundary layer erupts and if a correlation with the LEV detachment exists. It can also be correlated with the position of the rear stagnation point X_{SP} to check whether the formation of secondary structures at the leading edge directly depends on the flow reversal at the trailing edge or if it can occur independently. Therefore both possible LEV deatchment mechanisms introduced in section 2.6 can be distinguished.
Similar information may be gathered from the secondary LEV structure. As soon as a new full saddle above the leading edge appears and the fluid from the shear layer is redistributed between the primary and the secondary LEV structure as explained in section 2.6.2, a rise in the $\Gamma^{sec.LEV}$ curve can be expected. This curve indicates a change in the local flow topology at the leading edge.
These structures are exemplarily shown in figure 3.14. The airfoil is shown for chord normalized $\frac{x}{c}$ and stroke normalized $\frac{\Delta h}{y}$ coordinates. The above mentioned structures are shown by white contour lines, the vortex center is marked with a white dot. It should be noted, that the direction of rotation of the LEV and the secondary LEV is clockwise and the direction of rotation of the eruption caused secondary vortex and for a TEV is counter clockwise. The color coded contour represents the Γ_2 scalar field, which is used for the vortex identification and explained below. To distinguish the above mentioned flow structures and calculate their circulation flow topology and methods for critical identification and vortex identification are used.

3.6.1 Vortex identification

While the vorticity is a local quantity in the flow field $\omega(x, y) = \frac{\partial v}{\partial x} - \frac{\partial u}{\partial y}$, the circulation is a global measure of the strength of a vortex. The entire vorticity in the flow field cannot be attributed to distinct vortices, because regions of pure shear also exhibit a certain amount of vorticity or spurious vectors may cause large local vorticity values. The circulation of a vortex is therefore calculated by integrating the vorticity $\omega(x, y)$ over the

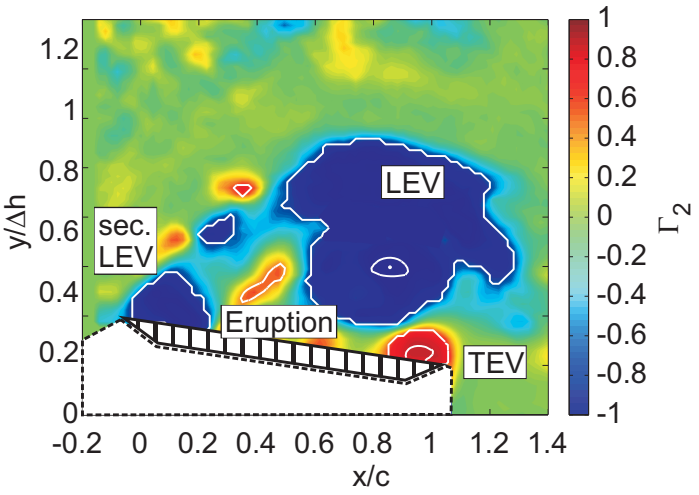

Figure 3.14: Exemplarily shown vortex structures with the corresponding Γ_2 scalar field

respective area A covered by a vortical structure. Therefore either methods are needed, which can distinguish between single vortex structures, or integration areas, which represent the vortex structures, have to be chosen manually. Because the manually defined integration areas may be arbitrary or may overlap unintentionally and calculate a spurious amount of circulation, vortex identification methods are preferred.
In the literature two types of vortex identification methods can be found. One method relies on the local flow properties. Kolar (2011) gives an overview of these methods, which are based on the decomposition of the flow velocity gradient $\nabla u = S + \Omega$ into a symmetric strain rate tensor $S_{ij} = \frac{1}{2}\left[\frac{\partial u_i}{\partial x_j} + \frac{\partial u_j}{\partial x_i}\right]$ and an antisymmetric vorticity tensor $\Omega = \frac{1}{2}\left[\frac{\partial u_i}{\partial x_j} - \frac{\partial u_j}{\partial x_i}\right]$, given in index notation. The most common of these methods are briefly describe below.

- Q-criterion: The Q-criterion introduced by Hunt *el al.* (1988) allocates flow regions to a vortex, when the magnitude of the vorticity prevails over the magnitude of the strain rate $Q = ||\Omega|^2 - ||S||^2 > 0$.
- Δ-criterion: Chong *el al.* (1990) define points of the flow field as a

vortex, if the streamlines around that point exhibit a circular motion in a reference frame moving with that point. They use the eigenvalues λ stemming from the characteristic equation for incompressible flows $\lambda^3 + Q\lambda - R = 0$ to characterize the local streamline pattern using the critical point theory, with Q as the vorticity tensor and $R = Det(\frac{\partial u_i}{x_j})$. For $\Delta = \frac{Q}{3}^3 + \frac{R}{2}^2 > 0$ a circular motions prevails and a vortex is defined.

- λ_2-criterion: Jeong and Hussain (1995) use the eigenvalues of the strain rate transport equation $\frac{DS_{ij}}{Dt} - \nu\frac{\partial S_{ij}}{\partial x_{kk}} + \Omega_{ik}\Omega_{kj} + S_{ik}S_{kj} = -\frac{1}{\rho}\frac{\partial p}{\partial x_{ij}}$ to determine local pressure minima associated with a vortical structure. The strain-rate transport equation is reduced by canceling unsteady irrotational terms $\frac{DS_{ij}}{Dt} = 0$ and viscous effects $\nu\frac{\partial S_{ij}}{\partial x_{kk}} = 0$. A vortex is then defined, when two of the eigenvalues of the simplified equation $\lambda_1 \geq \lambda_2 \geq \lambda_3$ are smaller than zero, or $\lambda_2 < 0$. Inaccuracy may arise from neglecting unsteady and viscous effects.

Due to measurement uncertainty, small scale velocity fluctuations and small spacing between the data points for PIV, the gradients may be falsified and the vortex identification methods can fail and locally disrupt the coherence of vortical structures. Therefore an alternative type of vortex identification methods was introduced by Graftieaux *el al.* (2001) to overcome these problems. This methods relies on an integral flow behavior in contrast to the above mentioned local identification criteria. At each point P in a the flow field the two scalars Γ_1 and Γ_2 are defined. S denotes a planar area around P, which contains N measurement points. For each of the N points M an algorithm is performed to obtain an integral scalar value Γ_1 and Γ_2 in S with the center P. Both Γ_1 and Γ_2 lie in the range $-1...1$. Points in the flow field exceeding the typical threshold of $\Gamma_1 \geq 0.9$ are defined as a vortex center, points in the flow field exceeding the typical threshold of $\Gamma_2 \geq \frac{2}{\pi}$ are allocated to a vortical structure.
The mathematical definition of Γ_1 for discrete velocity field is given by equation 3.5 taken from Graftieaux *el al.* (2001).

$$\begin{aligned}\Gamma_1 &= \frac{1}{N}\sum_N \frac{PM \times U_M}{||PM|| \cdot ||U_M||} \\ &= \frac{1}{N}\sum_N sin(\theta_M)\end{aligned} \tag{3.5}$$

Γ_1 describes the averaged angle θ_M between the flow velocity U_M at point M and the distance PM between the center point P and M and captures the circular fluid motion around P. The number of N points acts as a spatial filter and is set to a typical value of $N = 9$. The procedure is schematically illustrated in figure 3.15.

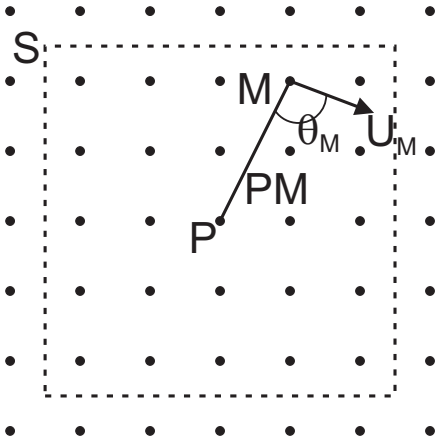

Figure 3.15: Illustration of the determination of the scalar Γ_1 according to Graftieaux *el al.* (2001)

Γ_2 is calculated analogous to Γ_1, with the only difference that not the angle between PM and the absolute flow velocity U_M is considered, but the velocity $U_M - \tilde{U}_P$ relative to the averaged convection speed of $\tilde{U}_P = \frac{1}{N}\sum_N U_M$ in S. Therefore Γ_2 is in contrast to Γ_1 galilean invariant. The mathematical definition of Γ_2 for discrete velocity field is given by equation 3.6.

$$\Gamma_2 = \frac{1}{N} \sum_N \frac{PM \times (U_M - \tilde{U}_P)}{||PM|| \cdot ||U_M||} \tag{3.6}$$

The vortex trajectory can be obtained by tracking the maximum value of Γ_1 representing the vortex center. The LEV was defined as the vortical structure in the *FOV* containing the largest amount of clockwise circulation. The TEV was defined as the structure of counter-clockwise circulation whose center was downstream of 75 % of the chord length. The eruption vortex was defined as the coherent structure of counter-clockwise circulation above the airfoil between $0 \leq \frac{x}{c} \leq 0.6$. The implementation of this method has been verified by determining the circulation of a well-defined Lamb-Oseen vortex.

3.6.2 Critical point identification

The LEV rear reattachment point is tracked to identify the instants in the stroke cycle, when flow reversal at the trailing edge may occur. These instants can be correlated with the LEV circulation to evaluate the LEV detachment mechanism. The rear reattachment point belongs to a group of distinct points in flow fields, referred to as critical points. At these critical points the direction of velocity is indefinite and therefore the velocity magnitude is zero. If these points are attached to a solid wall, the shear stress vanishes. Therefore the LEV rear reattachment point can be identified as long as the LEV is attached to the airfoil as the rear most stagnation point on the surface of the airfoil. The cartesian velocity information on the surface of the airfoil suction side is under consideration of the instantaneous geometrical angle of attack transformed into a component along the chord length U_{chord} and a component normal to the wall $U_{wallnormal}$. The critical points on the airfoil are determined for neighboring points whose chordwise velocity components change their sign $U_{chord,i} * U_{chord,i+1} < 0$. The critical points in the free stream are more difficult to obtain, the method described by Depardon *el al.* (2006) has been used. In a first step areas potentially containing critical points are marked. It is assumed that the flow angle in the vicinity of a critical point is not uniform and covers a broad range of different angles nearly uniformly. The range of velocity angles is divided

Table 3.2: Classification of a critical point according to the real and imaginary parts of the eigenvalues of their Jacobi matrix

	R_1	I_1	R_2	I_2
saddle point	< 0	$= 0$	> 0	$= 0$
sink	< 0	$= 0$	< 0	$= 0$
source	> 0	$= 0$	> 0	$= 0$
attracting focus	$= R_2 < 0$	$= -I_2 \neq 0$	$= R_1 < 0$	$= -I_1 \neq 0$
repelling focus	$= R_2 > 0$	$= -I_2 \neq 0$	$= R_1 > 0$	$= -I_1 \neq 0$
center	$= 0$	$= -I_2 \neq 0$	$= 0$	$= -I_1 \neq 0$

into eight bins of the size of $\frac{\pi}{4}$. For each point in the FOV an area of 5×5 neighboring points was selected and the flow angle was calculated for each neighboring point. If at least six bins were populated, the area was considered as a potentially containing a critical point.
According to Helman and Hesselink (1991) critical points can be classified into centers, foci, sources, sinks and saddle points. The eigenvalues Λ_1 and λ of the Jacobi matrix $J = \frac{\partial u_i}{\partial x_j}$ of the flow at the respective critical point can be used to determine to which class this critical point belongs. Therefore the eigenvalues are divided into their imaginary I and real R parts $\lambda_1 = I_1 + R_1$ and $\lambda_2 = I_2 + R_2$, which characterize the topology in the vicinity of that critical point. Table 3.2 summarizes the classification. In this study saddle points are considered and foci and centers are denoted as nodes (or vortex centers). The drawback of this method is its sensitivity against noise or spurious vectors, since it relies on the velocity gradients and may calculate unphysical critical point properties for experimental data.

Another method to distinguish critical points in the free stream (explained by Depardon *el al.* (2006)) is the utilization of the Poincare-Bendixson Index (PBI). A closed loop L is placed around a region of potentially critical points and the angle θ_i between an arbitrary fixed line and the velocity vectors at the points on i on L is calculated. The normalized change in the angle $\frac{\Delta\theta}{2\pi} = PBI$ along L corresponds to the number of saddle points and nodes inside L. If $PBI = +1$ the critical point is a node, if $PBI = -1$ the critical point is a saddle point. To exactly determine the position of a

saddle point in an area with $PBI = -1$, the extremum $|\Delta\theta| = \frac{-cos(\theta_M)}{sin(\theta_M)}$ or $|\Delta\theta| = \frac{sin(\theta_M)}{cos(\theta_M)}$, depending on θ_M, is used. After distinguishing all identified critical points into saddles and nodes and determining their precise location, the LEV rear attachment point is considered as the rearmost saddle (or half saddle) point in the FOV.

3.6.3 Finite time Lyapunov exponent

The finite time Lyapunov exponent (FTLE) is used to characterize the unsteady boundary layer separation caused by a vortex-wall interaction near the leading edge of an airfoil. According Ruiz *el al.* (2010) the FTLE is able to indicate separated regions in the flow field by a ridge which corresponds to a unstable manifold and is indicated by a high value for the FTLE. If such a ridge appears in the flow field, a closed separated region starts to form and marks the begin of a boundary layer eruption, which has great impact on the LEV detachment behavior.
The basic idea is schematically shown in figure 3.16. Two distinct regions in the flow field have developed. The primary LEV and a secondary vortical structure due to boundary layer separation beginning at the half saddle S'. Both flow regions are separated by a dashed line connecting the full saddle point S with S'.

The FTLE is a scalar vector which represents the amount of stretching along a trajectory between two consecutive time step and gives a measure for the separation of two trajectories. These trajectories are calculated from seeding the flow field with virtual particles and track their positions over time (forward or backward) by integrating their displacement. For backward time integration, if the particle trajectories originating at different positions in the flow converge in the same neighborhood for a certain choice if finite integration time T_f the FTLE is large and marks a separatrix in the flow field. For forward integration, the FTLE is large for two virtual particles starting in close vicinity, but whose trajectories diverge. In figure 3.16 particles originally placed in the primary LEV or the separated flow region move backwards along the indicated path lines and converge at the dashed line, which marks the border between the two regions.
The method to calculate the trajectories of these virtual particles here was

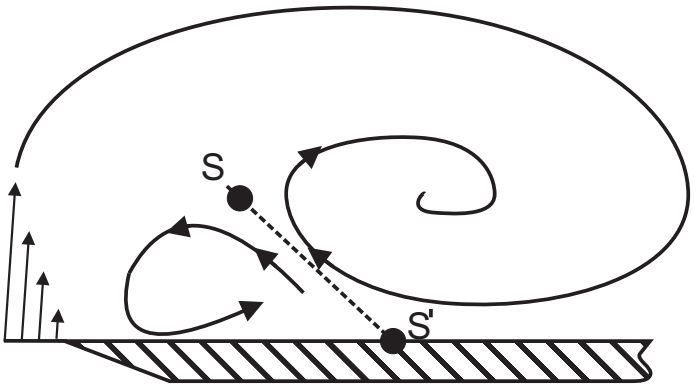

Figure 3.16: Flow structure near the leading edge of an airfoil

introduced by Haller (2002). The linearized trajectories of all points in the vicinity of a point $x_0 = x(t_0; t_0, x_0)$ with t_0 and x_0 as the starting conditions in time and space are integrated over the finite time T_f, using the local velocity vector $\frac{\partial x}{\partial t} = \vec{U}(t, x)$. It was shown by Haller (2002) that the direction of the largest stretching between two neighboring points can be expressed by the maximum eigenvalue $\lambda_{max}(\Delta)$, with $\Delta = A^T A$, where $A = \frac{\partial x_i(t+T_f;t_0,x_o)}{\partial x_j(t_0;t_0,x_o)}$ denotes the spatial gradient tensor of two neighboring points after the integration time T_f. The FTLE $\sigma_{t_0}^{T_f}(x_0)$ is then defined as an exponential separation rate at x_0 , given by $\sigma_{t_0}^{T_f}(x_0) = \frac{1}{T_f}\sqrt{\lambda_{max}(\delta)}$. The equations above have been taken from Shadden *el al.* (2005).
The velocity fields, which were acquired with a rate of 2 kHz were interpolated using time steps of 0.25 ms. The integration time was set to $T_f/T = 3.16$ % with respect to the airfoil motion time T.
This operation is then applied to the temporally interpolated unsteady velocity fields and an exemplary results from experimental data is given in figure 3.17. The Lyapunov exponent σ is overlaid with instantaneous streamlines of the velocity field. Distinct ridges can be seen at the shear layer, separating the far flow field from the inside of the vortical structures. The boundary layer separation is confined by ridges against the large primary LEV an the secondary LEV right at the leading edge. The structure of the Lyapunov exponent corresponds to the instantaneous streamlines

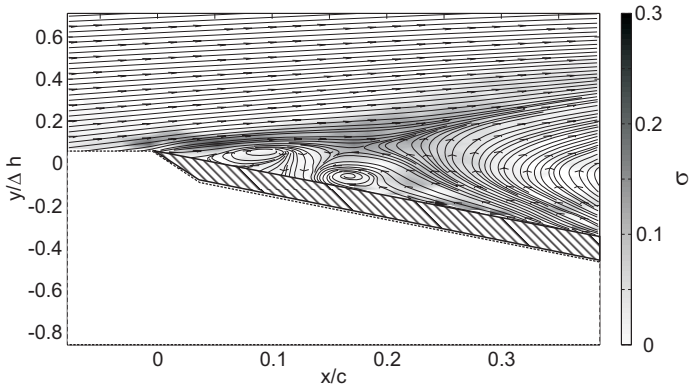

Figure 3.17: Exemplary instantaneous streamlines and Lyapunov exponent σ of unsteady flow structures at the leading edge of an airfoil

and captures the boundary layer separation correctly.

4 Smoke flow visualization

Smoke flow visualization illustrates the LEV growth and detachment processes and serves to gain better descriptive insights into the physical processes associated with LEV detachment. Additionally this visualization was used to verify the hypothesis, that the LEV detachment does not depend directly on the interaction of the LEV with the trailing edge, but instead is caused by interrupting the connection between the feeding shear layer and the LEV at the leading edge. This may either be caused by the formation of secondary vortical structures due to viscous/inviscid effects or the upstream transport of fluid from the trailing edge containing opposite signed vorticity. Both mechanisms may lead to LEV detachment independently and are described in section 2.6. The smoke flow visualization reveals the overall evolution of LEV formation and the evolution of the flow near the leading edge prior to LEV detachment.
Figure 4.1 shows the results of the smoke flow visualizations of a pitching flat plate with a chord length of 120 mm for in time equally sampled instants $t/T = [0.44...0.89]$ in the non-dimensional stroke cycle with the flow direction from left to right. The given configuration serves as an example to illustrate all relevant flow phenomena. The plate is started from rest at a non-dimensional stroke cycle $t/T = 0$, reaches its maximal angle of attack 45° at $t/T = 0.5$ and is fixed at that position to observe the LEV evolution independent of subsequent upstroke effects. The Reynolds number was set to $Re = 28,000$, the reduced frequency to $k = 0.5$ and images were acquired with a frequency of $f_{acq} = 1$ kHz.

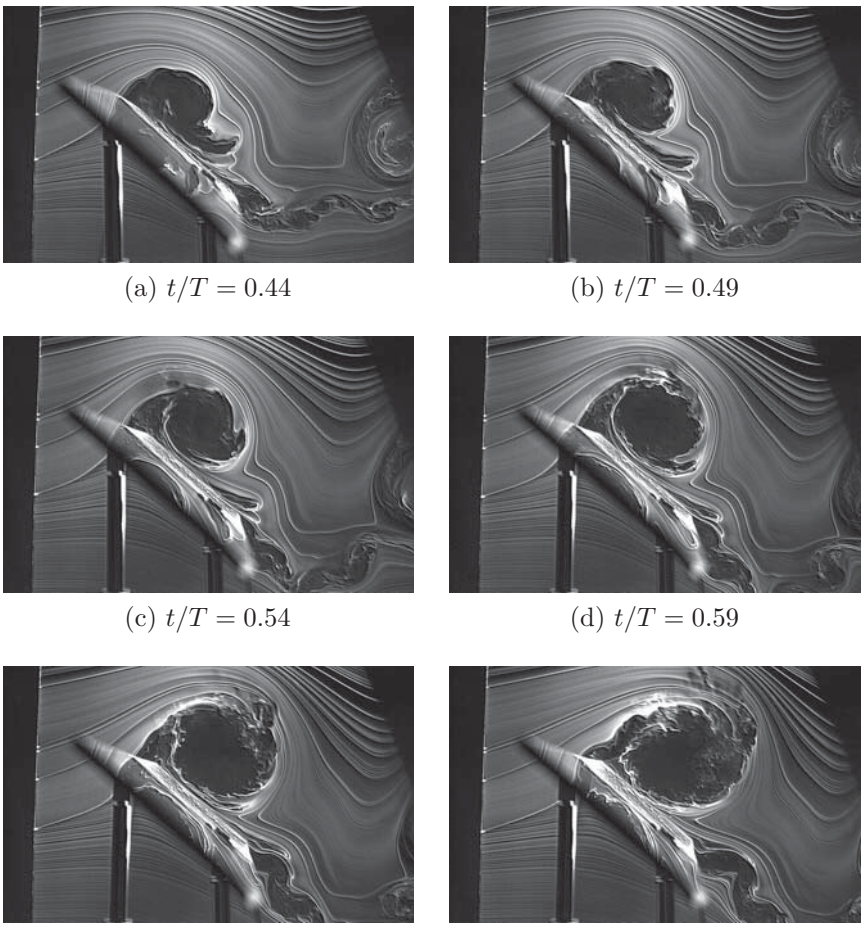

(a) $t/T = 0.44$ (b) $t/T = 0.49$

(c) $t/T = 0.54$ (d) $t/T = 0.59$

(e) $t/T = 0.64$ (f) $t/T = 0.69$

Figure 4.1: Smoke flow visualizations of the global LEV growth and the formation of local secondary structures near the leading edge

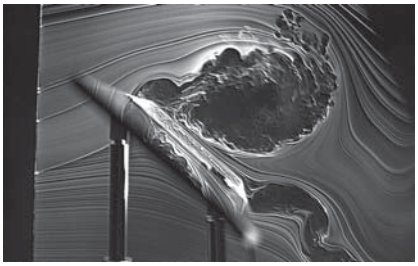

(g) $t/T = 0.74$

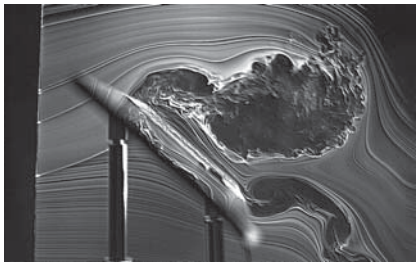

(h) $t/T = 0.79$

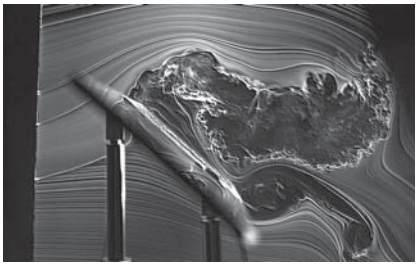

(i) $t/T = 0.84$

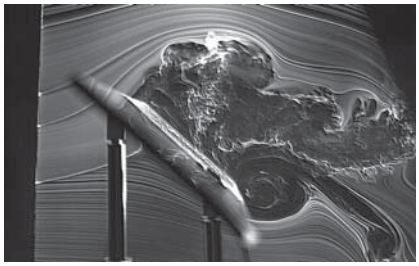

(j) $t/T = 0.89$

Figure 4.1: Smoke flow visualizations of the global LEV growth and the formation of local secondary structures near the leading edge

At the cycle time $t/T = 0 - 0.44$ the shear layer separates at the leading edge and the unsteady separation bubble rolls up into a distinct vortex. This distinct vortex is visible above the flat plate for Figure 4.1 (a). The starting TEV is visible on the right edge of the figure. Between $t/T = 0.44 - 0.59$ this vortex grows and no flow separation at the leading edge is apparent. At $t/T = 0.64$ a first kink or separation bubble in the boundary layer directly at the leading edge is visible. During this period the LEV reattachment point moves downstream. At $t/T = 0.69$ the LEV reattachment point has not reached the trailing edge yet, but a region with two counter rotating secondary vortices is present at the leading edge. A secondary vortex rolls up from the shear layer. While the LEV grew larger in the period $t/T < 0.69$, at $t/T = 0.69$ a tilt to the right side of the LEV is visible, indicating that the LEV is convected downstream instead of growing further. As the LEV convects downstream, its rear reattachment point reaches the trailing edge and subsequently a TEV starts to roll up at $t/T = 0.74$ and the secondary LEV at the leading edge has developed into a distinct vortex. At $t/T = 0.79$ a channel has opened below the LEV enabling fluid from the trailing edge to be transported upstream, which inhibits the growth of the secondary LEV, and the primary LEV deteriorates. While the TEV continues to grow for $t/T \geq 0.84$, the two LEVs lose their distinct shape and move downstream, concluding the LEV formation and detachment cycle.
It can be seen from the visualizations that the secondary structures at the leading edge may form independently of the position of the LEV rear reattachment point. Thereby a secondary structure rolling up from the shear layer can be observed, which cuts the advection of fluid from the shear layer into the primary LEV. Both structures become less clearly defined as fluid from the trailing edge is transported upstream and cancels the vorticity production at the leading edge due to an interaction of layers of opposite sign vorticity These observations strengthen the hypothesis that flow phenomena at the leading edge ultimately lead to LEV detachment.

5 Reynolds number influence on the formation of secondary structures

In this chapter the effect of the viscosity on the formation of secondary structures and their impact on LEV growth and detachment was investigated for the simplest kinematic case. A flat plate of the chord length $c = 120$ mm with sharp leading and trailing edges is pitched down about the leading edge during a motion period of ΔT from an angle of attack of $\alpha_{geo} = 0°$ to $\alpha_{geo} = 30°$ and held fixed. With an infinitely small leading edge curvature, the shear layer separates at a well defined location and is not a function of the Reynolds number; the influence of the Reynolds number is limited to the formation of secondary structures. The stroke height at the trailing edge is $\Delta h = \frac{c}{2}$. By arresting the plate after the pitch-down motion the angle of attack is fixed at $\alpha_{geo} = 30°$, there is no influence of an unsteady pressure gradient $\frac{\partial p}{\partial x}(t)$. The angle of attack does not decrease during the second half of the motion cycle as observed during a typical plunging downstroke. The isolated evolution of the secondary structures can be investigated. The detachment of the LEV is defined according to Fage and Johanson (1928) as the instant in the stroke cycle, when the LEV reaches its peak value of circulation. LEV detachment can also be defined as the instant, when the normal force on the airfoil drops due to the convection of the LEV as explained in section 2.2. Therefore the LEV trajectory is used to determine the instant at which the LEV begins convect away from the plate. A kink in the LEV trajectory therefore indicates a change of the LEV position in chordwise direction and therefore marks this instant of incipient detachment.
It is hypothesized, that the formation of secondary vortical structures is associated with a topological change near the leading edge and eventually leads to the detachment of the LEV. The goal of this investigation is to experimentally connect the LEV detachment with the occurrence of the secondary structures. The formation of secondary structures can be attributed either to a viscous/inviscid interaction of the LEV and the

Table 5.1: Experimental parameters of the four test cases

Test case	Reduced frequency k	Motion period ΔT [ms]	Freestream velocity U_∞ $[\frac{\mathrm{m}}{\mathrm{s}}]$
$Re = 10000$	0.25	566	1.33
$Re = 35000$	0.25	162	4.66
$Re = 60000$	0.25	94	8.00
$Re = 80000$	0.25	71	10.66

boundary layer or to the global inviscid flow topology, represented by flow reversal at the trailing edge. Decreasing the Reynolds number sufficiently; hence emphasizing viscous effects, results in the formation of secondary structures due to the boundary-layer eruption. The Reynolds number is suspected to determine when the LEV detachment mechanism changes from being caused by the boundary-layer eruption or by the generation of a full saddle point at the trailing edge, i. e. by the global flow topology. The experimental parameters have been chosen to represent the LEV formation during efficient flapping forward flight. The reduced frequency was set to $k = \frac{\pi c}{2\Delta T U_\infty} = 0.25$, the Reynolds number was varied through the values from $10,000$ to $80,000$ (as shown in table 5.1) representing values typical for LEV formation during efficient forward flight. Table 5.1 summarizes the experimental parameters of the free stream velocity U_∞ and the pitching period ΔT for all experimental cases.

It is expected that for small Reynolds numbers distinct secondary structures emerge before a flow reversal at the trailing edge can occur. For large Reynolds numbers a boundary-layer separation and a subsequent interaction of the shear layer with secondary structures is expected to occur as a result of the flow reversal at the trailing edge and transport of fluid with opposite signed vorticity upstream to the leading edge.
The focus of this investigation lies on the formation of the secondary vortical structures near the leading edge and their influence on the LEV evolution and not on the separation behavior of the shear layer from the leading edge. While both effects are likely to depend on the Reynolds number, sharp leading edges are used to obtain a well defined location of the shear layer separation for all cases and make it independent of the Reynolds number. Possible effects of the separation behavior on the results are min-

imized.

5.1 Recording and data analysis

For the pure pitching experiments, two fields of view are recorded simultaneously, therefore the setup is extended by mirror and an additional camera. The global FOV is used to extract the circulation of the LEV Γ^{LEV} and the position of the rear reattachment point X_{SP}. The maximum in Γ^{LEV} indicates LEV detachment, a correlation with the position of the rear reattachment point X_{SP} at that instant shows if the LEV detachment can be attributed to flow reversal or viscous effects. The local FOV is used to extract the circulation of the secondary LEV rolling up from the shear layer Γ^{secLEV} and the circulation of the vortical structure $\Gamma^{Eruption}$ caused by the boundary-layer separation to estimate the effects of viscosity and to indicate the topological change leading to LEV detachment. Additionally, the Lyapunov-Exponent σ is calculated for the local field of view to identify self-contained regions in the flow field and determine the onset of boundary-layer separation. Figure 5.1 shows an example of the recorded and processed flow field from FOV 2 and the identified vortical structures.

The normalized vorticity $\frac{\omega c}{U_\infty}$ is shown as color-coded contours, with red as counter-clockwise and blue as clockwise rotating fluid. The abscissa is non-dimensionalized by the chord length $\frac{x}{c}$, the ordinate is non-dimensionalized by the stroke height $\frac{x}{\Delta h}$. The arrows indicate the flow direction. The black solid lines represent the contour of each identified vortex, with the nodal points N_1 in the center of the secondary LEV and N_2 in the center of the eruption vortex. The full saddle above both structures is denoted by S_2. The half saddle, indicating boundary-layer separation, is denoted by S_3'; the half saddles at the leading edge and between both secondary structures by S_1' and S_2'.

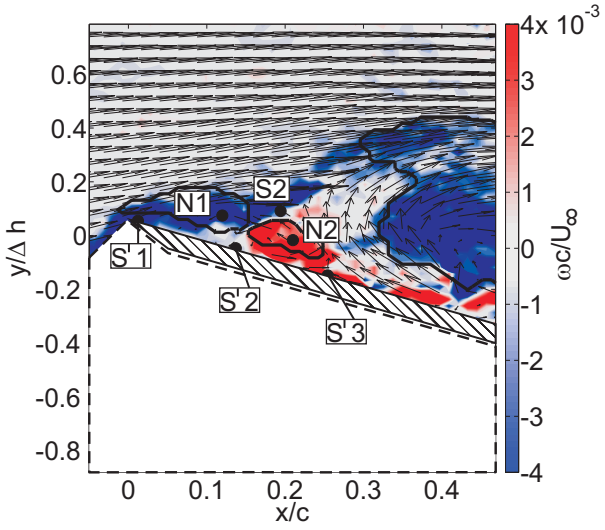

Figure 5.1: Example of the flow field, the identified vortical structures and the identified critical points in the local field of view *FOV* 2

5.2 Flow structures

The results of the four experimental test cases with the Reynolds numbers of $Re = 10,000$ $Re = 35,000$, $Re = 60,000$ and $Re = 80,000$ are shown in figures 5.2 for the global FOV and in figure 5.3 for the local FOV. The normalized vorticity $\omega^* = \frac{\omega c}{U_\infty}$ is color coded, with red as counter-clockwise (positive) vorticity and blue as clockwise (negative) vorticity. The velocity vectors calculated at each IA are superimposed in figure 5.3 and the streamlines are superimposed in figure 5.2.
The global evolution of the flow field shown in figure 5.2 is similar for the cases with the Reynolds numbers of $Re = 10,000$ $Re = 35,000$, $Re = 60,000$ and $Re = 80,000$. The LEV rolls up at similar instants in the stroke cycle t/T and grows with approximately the same rate, until it detaches and triggers the formation of a TEV. For $Re = 10,000$ the LEV evolution is shifted towards earlier stages. The secondary structures shown in figure 5.3 exhibit a different behavior. For $Re = 10,000$ distinct secondary vortices develop at the leading edge, already during LEV growth and prior to LEV detachment. These structures form before the rear stagnation point of the LEV exceeds the trailing edge, enabling reversed flow. With increasing Reynolds number these secondary vortical structures are less clearly defined.

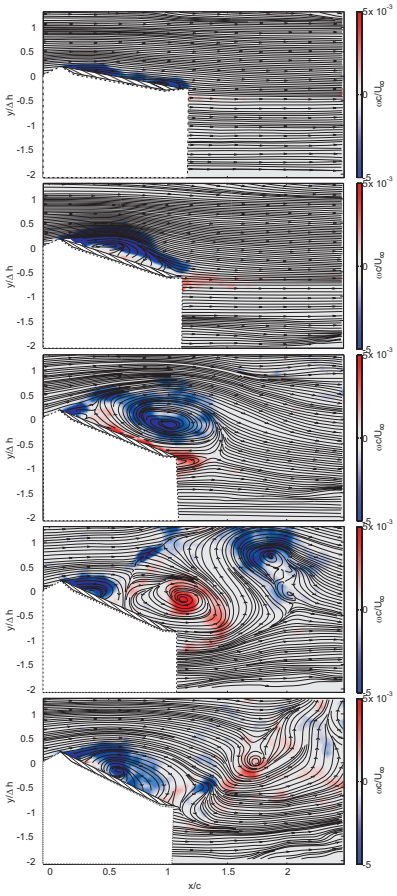

(a) $Re = 10000$

Figure 5.2: Time resolved global flow field (FOV 1) development in terms of normalized vorticity and streamlines for each experimental case at $t/T = [0.15\ 0.25\ 0.35\ 0.45\ 0.55]$

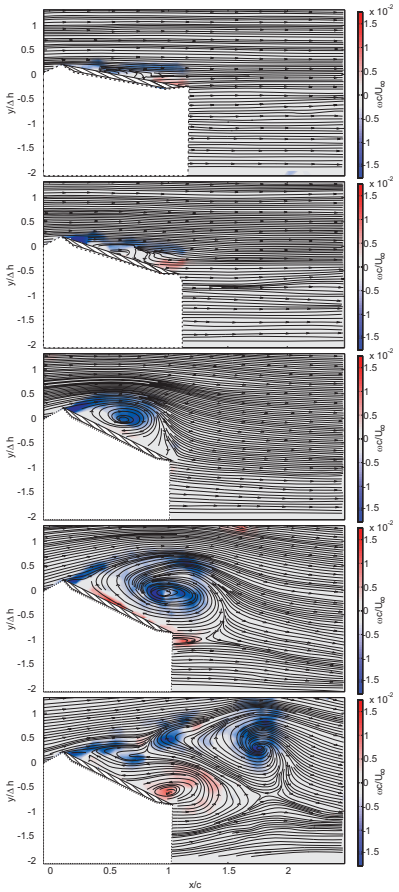

(b) $Re = 35000$

Figure 5.2: Time resolved global flow field (FOV 1) development in terms of normalized vorticity and streamlines for each experimental case at $t/T = [0.15\ 0.25\ 0.35\ 0.45\ 0.55]$

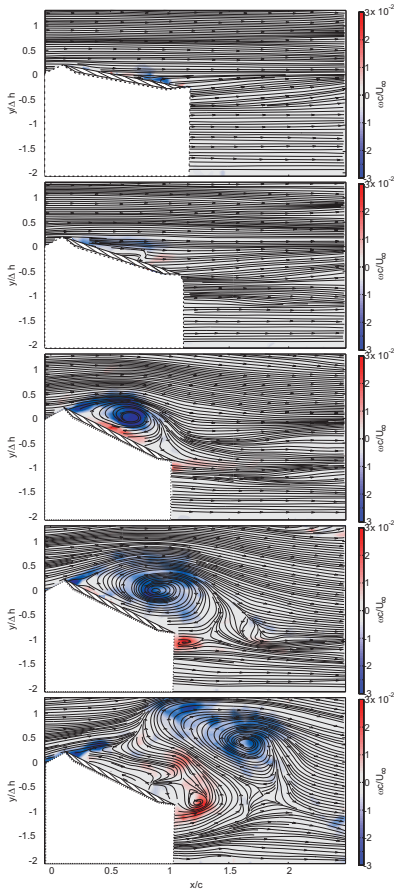

(c) $Re = 60000$

Figure 5.2: Time resolved global flow field (FOV 1) development in terms of normalized vorticity and streamlines for each experimental case at $t/T = [0.15\ 0.25\ 0.35\ 0.45\ 0.55]$

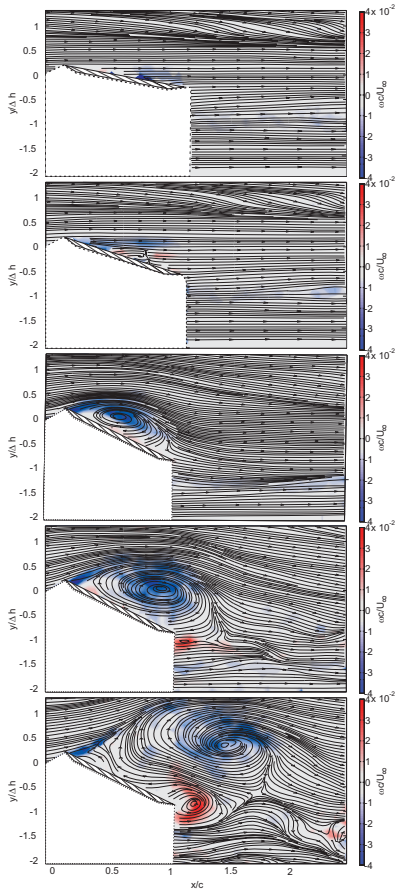

(d) $Re = 80000$

Figure 5.2: Time resolved global flow field (FOV 1) development in terms of normalized vorticity and streamlines for each experimental case at $t/T = [0.15\ 0.25\ 0.35\ 0.45\ 0.55]$

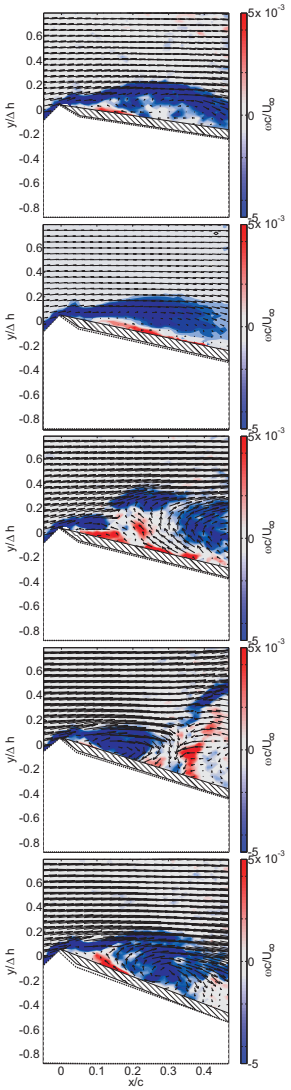

(a) $Re = 10000$

Figure 5.3: Time resolved development of the flow field in the leading edge region (FOV 2) in terms of normalized vorticity and velocity vectors for each experimental case at $t/T = [0.15\ 0.25\ 0.35\ 0.45\ 0.55]$

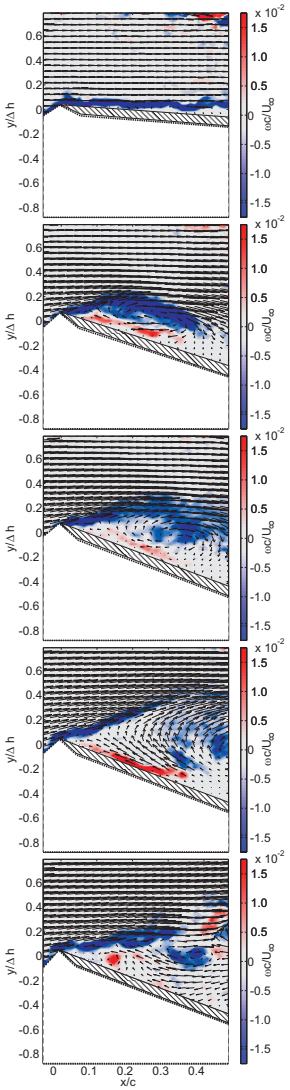

(b) $Re = 35000$

Figure 5.3: Time resolved development of the flow field in the leading edge region (FOV 2) in terms of normalized vorticity and velocity vectors for each experimental case at $t/T = [0.15\ 0.25\ 0.35\ 0.45\ 0.55]$

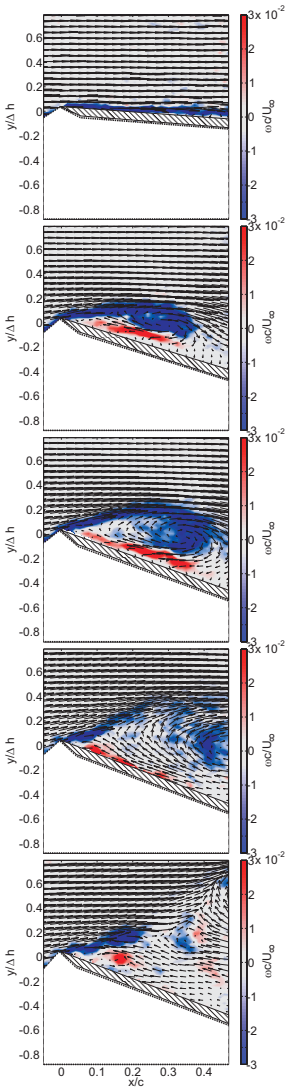

(c) $Re = 60000$

Figure 5.3: Time resolved development of the flow field in the leading edge region (FOV 2) in terms of normalized vorticity and velocity vectors for each experimental case at $t/T = [0.15\ 0.25\ 0.35\ 0.45\ 0.55]$

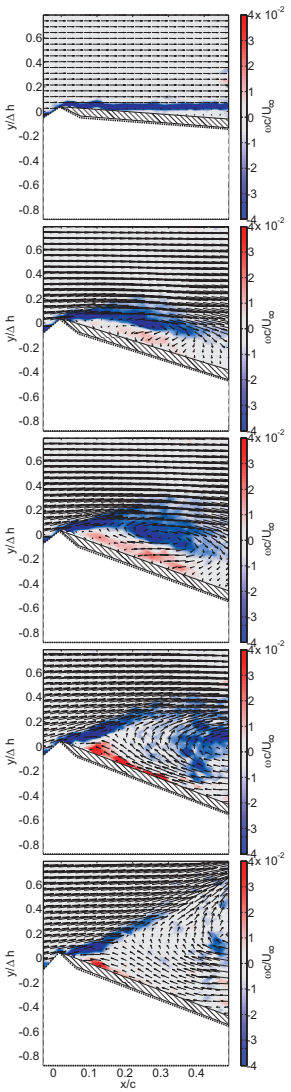

(d) $Re = 80000$

Figure 5.3: Time resolved development of the flow field in the leading edge region (FOV 2) in terms of normalized vorticity and velocity vectors for each experimental case at $t/T = [0.15\ 0.25\ 0.35\ 0.45\ 0.55]$

5.3 Lyapunov exponent and formation of secondary structures

The calculation of the Lyapunov index allows a more detailed view on the formation of secondary structures near the leading edge, by identifying self-contained zones in the flow field and the beginning of boundary-layer separation, as explained in section 3.6.3. Areas with a high Lyapunov exponent indicate boundaries of individual structures. The Lyapunov exponent σ is shown in figure 5.4 with the overlaid instantaneous streamlines of the interpolated velocity fields used for the calculation of σ. The instants in the stroke cycle shown in figure 5.4 have been chosen to show the onset of the formation of secondary structures.

For all Reynolds numbers, the Lyapunov exponent σ exhibits a strong ridge near the shear layer at the leading edge, which indicates a strong separation between the primary LEV and the outer flow. For $Re = 10,000$ early in the stroke cycle around $t/T = 0.26$, boundary-layer separation is indicated by a second ridge below the LEV, separating it from the leading edge region. This separation occurs well before flow reversal at the trailing edge and can therefore by attributed to a LEV induced viscous/inviscid interaction. After boundary-layer separation, around $t/T = 0.35$, two distinct secondary vortices have formed, altering the flow topology near the leading edge. All three structures are separated by ridges in σ. The secondary structure with clockwise rotation rolls up into a new LEV fed by the shear layer at $t/T = 0.44$, causing the primary LEV to detach.
A similar behavior can be observed for $Re = 35,000$, but boundary-layer separation occurs later in the stroke cycle, around $t/T = 0.40$. At this instant flow reversal at the trailing edge has already taken place and the boundary-layer separation cannot exclusively be attributed to the LEV induced effects. The secondary structures appear around $t/T = 0.50$; the secondary clockwise vortex is located above the counter clockwise secondary vortex and is very narrow. The Lyapunov exponent around the full saddle point is large, indicating three self-contained structures.
For the Reynolds numbers $60,000$ and $80,000$ the evolution of the secondary structures is different. The occurrence of secondary structures is postponed to later stages in the stroke cycle compared to smaller Reynolds numbers; small ridges in σ indicate that boundary-layer separation does not appear before $t/T = 0.50$, when the transport of fluid with counter-

clockwise rotating from the trailing edge has long been initiated. Although distinct structures of counter-clockwise rotation are formed, the structures of clockwise rotation become very narrow and are shifted towards the separated shear layer region around $t/T = 0.60$.
The Lyapunov exponent shows that the formation of secondary structures near the leading edge and, therefore, the LEV detachment mechanism, depends on the Reynolds number. For low Reynolds numbers, the secondary vortical structures develop independently of the flow reversal at the trailing edge and are induced by a viscous/inviscid interaction between the primary LEV and the boundary layer and a subsequent boundary-layer separation. The early occurrence of these secondary structures has an influence on the LEV formation and the LEV size. At higher Reynolds numbers, the boundary layers are thin and resistant against a viscous/inviscid interaction. Secondary structures do not form before the upstream transport of counter clockwise fluid as a result of the flow reversal at the trailing edge. Therefore the LEV formation and detachment is expected to be independent of the secondary structures. The mechanism, which initiates the LEV detachment and limits its growth is the transport of fluid with counter-clockwise from the trailing edge to the shear layer at the leading edge and a subsequent interaction. Only after such an interaction, secondary structures develop near the leading edge. This leads to the conclusion that for high Reynolds number the chord length is the appropriate characteristic length.

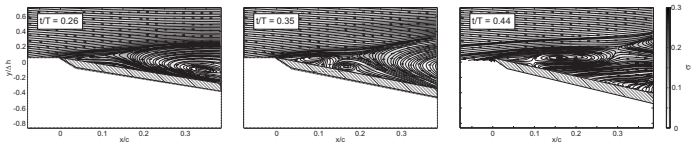

(a) $Re = 10000$

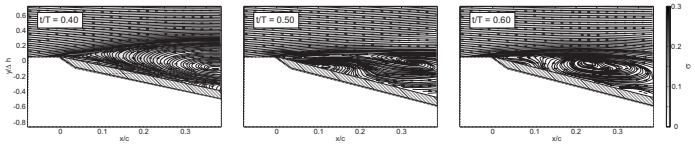

(b) $Re = 35000$

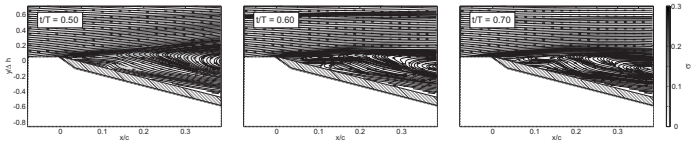

(c) $Re = 60000$

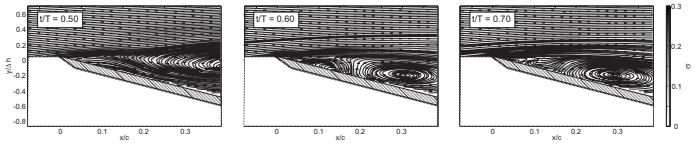

(d) $Re = 80000$

Figure 5.4: Development of the flow field in the leading edge region (FOV 2) indicated by the Lyapunov exponent σ and instantaneous streamlines

5.4 Results

To quantify these observations, the circulation of the LEV, the TEV, both secondary vortices and the LEV trajectories in chordwise direction are shown in the following section. Figure 5.5 shows the normalized LEV circulation $\frac{\Gamma^{LEV}}{cU_\infty}$. The evolution of the LEV circulation for $Re = 10,000$ is shifted towards earlier stages in the stroke cycle, while the evolution of the LEV at higher Reynolds numbers collapses, as apparent in the figures 5.3 and 5.2. Although all normalized circulation values exhibit similar peak values, the level of $\frac{\Gamma^{LEV}}{cU_\infty}$ for $Re = 10000$ is somewhat smaller than for the other cases, which can be explained by different LEV detachment mechanisms due to an earlier development of the secondary structures at the leading edge. The vertical dashed lines indicate the instants in time, when the rear reattachment point moves beyond the trailing edge, which happens in all cases before the peak value of $\frac{\Gamma^{LEV}}{cU_\infty}$ is reached. Analog to the circulation, the instants of flow reversal at the trailing edge are similar for $Re = [35,000\ 60,000\ 80,000]$, but advanced to a lower time t/T in the stroke cycle for $Re = 10,000$. The period of LEV circulation increase in non-dimensional terms is prolonged for higher Reynolds numbers. This effect can be explained by influence of the shear layer thickness on LEV growth. As described in section 2.3 the shear layer thickness determines the ratio of circulation and mass transported into the LEV. If it is assumed, that the shear layer develops form a stagnation point on the airfoil, Schlichting (2001) computes the shear layer thickness to be $\delta_{SL} = \sqrt{\frac{\nu}{a}}$, with a being a characteristic parameter of the flow in the stagnation point vicinity. a is then replaced by $a = a_0 U_\infty$, with a_0 as a constant shear layer curvature, ensured by the sharp leading edge. For lower Reynolds numbers, a larger shear layer thickness is assumed, because $\delta_{SL} \propto U_\infty^{-0.5}$. At lower Reynolds numbers the LEV has accumulated sufficient mass to facilitate the flow reversal earlier in the stroke cycle, but exhibits a lower circulation. Because the variation of the shear layer thickness with free stream velocity $\frac{\partial \delta_{SL}}{U_\infty} \propto U_\infty^{-1.5}$ decreases progressively, the largest effects may be observed for small Reynolds numbers.

Figure 5.6 shows the normalized chordwise position x/c of the LEV centers as solid lines over the stroke cycle t/T. For a better visibility of the temporal correlation between the LEV circulation and trajectory, $\frac{\Gamma^{LEV}}{cU_\infty}$

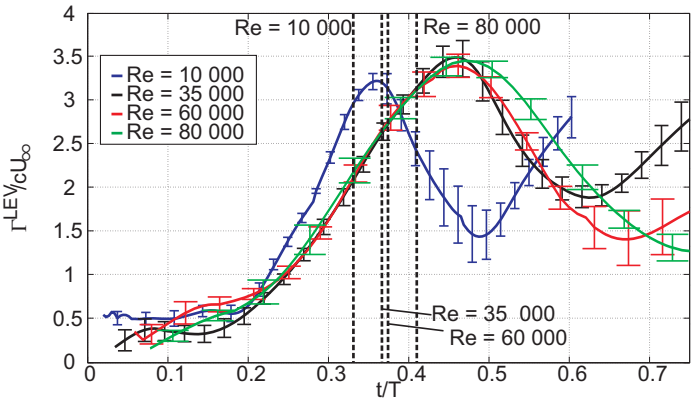

Figure 5.5: Normalized LEV circulation $\frac{\Gamma^{LEV}}{cU_\infty}$ for all four Reynolds numbers. The vertical dashed lines indicate the instants in the stroke cycle, when the rear LEV reattachment point has reached the trailing edge.

is added as dashed lines. The dots on the upper and lower side of the figure represent the instants for each Reynolds number, when the rear stagnation point moves beyond the trailing edge $x_{SP}/c = 1$ in its representative color. At first, the LEV trajectories remain close to the leading edge and exhibit a small slope, the LEVs move slowly over the airfoil as they grow. Again, in the case of $Re = 10,000$ the trajectory is shifted to earlier times. Subsequently, all trajectories exhibit a steep upward slope, which roughly coincides with the LEV circulation peak. Once the trajectory curves turn upwards the LEVs convect away at a much higher speed $\frac{u_{conv}}{U_\infty} \approx [0.37\ 0.39\ 0.39\ 0.38]$, indicating their detachment from the airfoil. Therefore the peak value of $\frac{\Gamma^{LEV}}{cU_\infty}$ (as suggested by Fage and Johansen (1928)) and the increased convection speed indicate detachment for the same instants in the airfoil motion cycle. It should be noted, that the acceleration in the LEV motion happens roughly at the same time, like the flow reversal at the trailing edge for higher Reynolds numbers, but happens independent of the trailing edge for the lowest Reynolds number.

The evolution of the TEV circulation is shown in figure 5.7. The maxi-

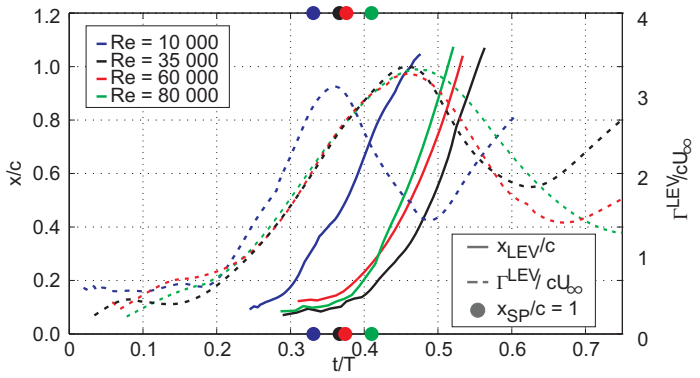

Figure 5.6: Normalized LEV trajectories x/c for all four Reynolds numbers as solid lines. The dashed lines represent the normalized circulation $\frac{\Gamma^{LEV}}{cU_\infty}$.

mal normalized circulation $\frac{\Gamma^{TEV}}{cU_\infty}$ decreases from the lowest to the highest Reynolds number. In all cases the TEV grows as a result of the rear LEV reattachment point moving beyond the trailing edge and allowing flow reversal there. The simultaneous growth of LEV and TEV during a period of $t/T = 0.3...0.5$ indicates, that the LEV detachment follows after the flow reversal at the trailing edge in all cases.

The evolution of the secondary vortical structures near the leading edge are shown in figure 5.8. Figure 5.8 shows the evolution of the structure with counter-clockwise rotation, which forms as a result of the topological change near the leading edge. It is either caused by the viscous/inviscid interaction or by the flow reversal at the trailing edge. In figure 5.8 the evolution of the normalized circulation of the secondary counter-clockwise vortex $\frac{\Gamma^{Erup}}{cU_\infty}$ develops independent of the flow reversal at the trailing edge for the Reynolds numbers $Re = 10,000$ and $Re = 35,000$, indicating the viscous/invisid interaction as the driving mechanism for detachment. At higher Reynolds number, when viscous effects are less predominant, these structures do not occur until counter-clockwise fluid from the trailing edge is transported upstream to the leading edge region. The circulation level decreases with increasing Reynolds number.

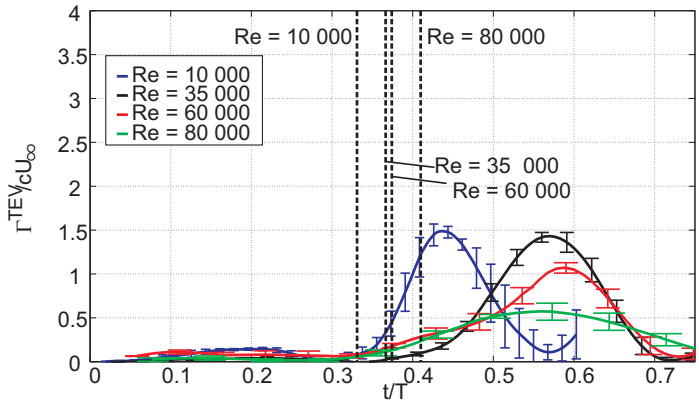

Figure 5.7: Normalized TEV circulation $\frac{\Gamma^{LEV}}{cU_\infty}$ for all four Reynolds numbers. The vertical dashed lines indicate the instants in the stroke cycle, when the rear reattachment point has reached the trailing edge.

The results correspond with the findings of Jones and Babinsky (2011), who find an accelerated LEV evolution for lower Reynolds numbers and a collapse of normalized circulation at higher Reynolds numbers. For the reduced frequency of $k = 0.25$ and the chord length limiting LEV growth (and thus neglecting viscous effects) the non-dimensional peak LEV circulation $\frac{\Gamma^{LEV}}{cU_\infty}$ is expected to correspond with to value predicted by optimal vortex formation $\frac{\Gamma^{LEV}}{cU_\infty} \approx 4$, which is true for all Reynolds numbers investigated. For $Re = 10,000$ the viscous effects are sufficiently strong to cause the LEV to detach earlier at a lower normalized circulation. At higher Reynolds numbers the boundary layers are thinner and much less susceptible against a LEV induced viscous/inviscid interaction. Viscous effects are damped and neither boundary-layer separation nor a formation of secondary structures can be observed until flow reversal at the trailing edge occurs. The circulation development and the peak values collapse for these Reynolds numbers and is unaffected by an altered flow topology at the leading edge. The formation of secondary structures can therefore be attributed to viscous effects. The Reynolds number primarily effects the evolution of secondary structures, which can ultimately lead to a transi-

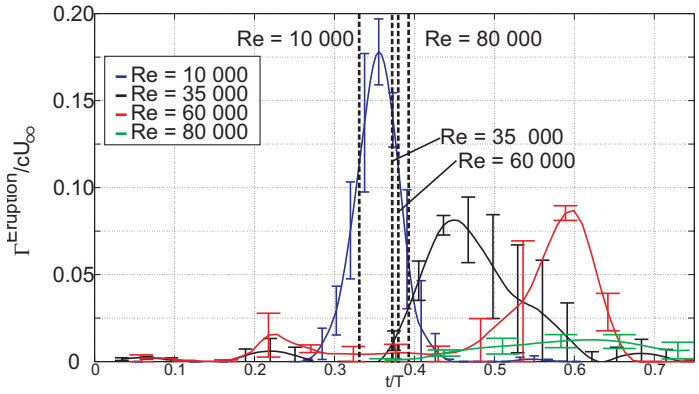

Figure 5.8: Development of the normalized circulation $\frac{\Gamma^{Erup}}{cU_\infty}$ of the secondary counter-clockwise rotating vortex for all four Reynolds numbers. The vertical dashed lines indicate the instants in the stroke cycle, when the rear reattachment point has reached the trailing edge.

tion in the LEV detachment mechanism. Secondary vortical structures can influence the growth of the primary LEV, a self-induced LEV detachment decreasing the maximal achievable LEV circulation is only possible at low Reynolds numbers. At sufficiently high Reynolds numbers the flow reversal at the trailing edge triggers the LEV detachment. The chord length is characteristic for the limitation of the LEV circulation. Additionally the peak circulation coincides with an acceleration in the LEV trajectory, indicating agreement between the observed LEV detachment and the definition presented by Fage and Johansen (1928). As proposed in the hypotheses given in section 2.7 the Reynolds number generally is a parameter to facilitate a transition between two fundamentally different LEV detachment mechanisms. These two mechanisms are independent of effects caused by the effective angle of attack history, since abstract airfoil kinematics with a fixed maximal angle of attack were investigated.

6 Influence of the leading edge shape on LEV formation

In this section the effect of the leading edge shape on the evolution of an LEV is investigated. The shear layer curvature a_0 is one of the parameters, which might influence the LEV growth and detachment, as presumed in section 2.7. Due to different leading edge shapes, the local pressure gradient in the boundary changes, which results in different shear layer parameters, which are directly linked to a_0. Therefore three aerodynamic profiles with different leading edge shapes and constant chord lengths $c = 50$ mm are investigated under the same unsteady aerodynamic conditions.
The experiments were carried out in the water tunnel at the University of Calgary, direct force measurements and PIV flow field measurements of plunging airfoils creating a distinct LEV have been conducted. The main features of the water tunnel and the measurements procedure are briefly described below.

6.1 Water tunnel and experimental rig

The experiments were carried out in a free surface water tunnel with a turbulence level of $Tu = 0.3$ % at a free stream velocity of $U_\infty = 0.2\frac{\mathrm{m}}{\mathrm{s}}$. The setup is shown in figure 6.1, taken from Rival *et al.* (2014). The airfoils were placed in the water tunnel at constant speed and executed a lateral plunging motion at the same time to facilitate a change in the effective angle of attack. A six degree-of-freedom hexapod was used to create a lateral plunging motion of the airfoil.

6.1.1 Airfoil shapes and kinematics

Figure 6.2 schematically shows the geometry of the three investigated airfoils. One flat plate with a sharp leading edge, one flat plate with a rounded

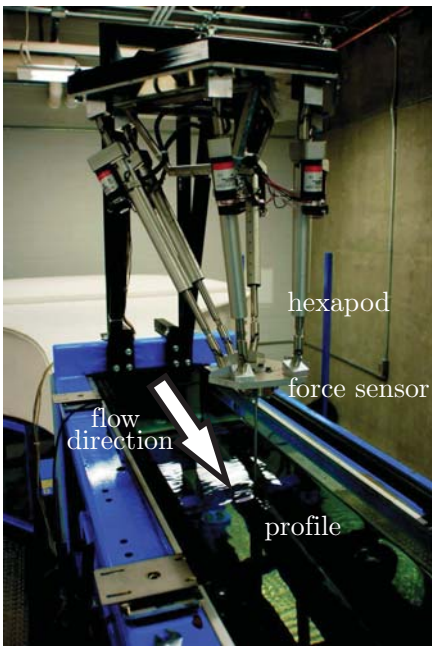

Figure 6.1: Experimental setup in the water tunnel, including the aerodynamic profile, the flow direction, the force sensor and the hexapod, adapted from Rival *et al.* (2014)

leading edge and a symmetric $NACA$ 0012 airfoil were used. The thickness of all airfoils was $d = 3$ mm.

The airfoils execute the first half of a pure sinusoidal plunging motion, driven by the custom made hexapod described in section 6.1. The plunging motion is less abstract than the pure pitch-and-hold motion described in section 5 and represents more realistic conditions. The geometrical angle of attack of $\alpha_{geo} = 0°$ is not varied. The plunging motion height was set to $h = c$, a maximum effective angle of attack of $\alpha_{eff} = 26°$ is reached a quarter of the motion period at $t/T = 0.25$. The motion period T has been selected in such a way, that a reduced frequency of $k = \frac{\pi c}{TU_\infty} = 0.25$ is obtained; the Strouhal number based on the trailing edge displacement

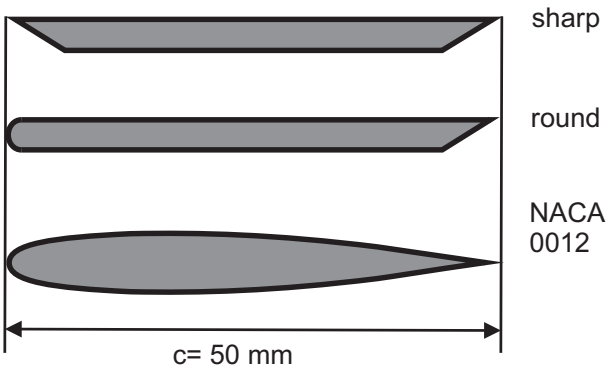

Figure 6.2: Schematical representation of the three different airfoil geometries.

during a full motion cycle reads $St = \frac{2h}{TU_\infty} = 0.16$. This parameter combination is representative for efficient forward flight and the formation of a distinct LEV in the flow field is expected. The motion kinematics were kept unchanged for all airfoil shapes.

6.1.2 Force measurements

A six-component *ATI Gamma* sensor flanged to the hexapod was used to record instantaneous force data at a sampling frequency of 1 kHz. Ten independent runs were executed per airfoil to collect the force data. The force data was post-processed by using a second order Savitzky-Golay filter with a span of 271 ms to smooth the raw signal using a least-squares fit. The force sensor records the overall acting forces during a plunging motion, including inertia, added mass and aerodynamic forces.

6.1.3 PIV

The flow field was recorded by using a two velocity component, time resolved PIV system, consisting of a Photonics Industries single-cavity laser with a wavelength of $\lambda = 527$ nm and a Photron APX-RS high-speed camera (12-bit monochrome image of 1024 x 1024 pixel resolution). The PIV

setup is schematically shown in figure 6.3, taken from Rival *et al.* (2014). The airfoil is illuminated with a laser sheet from above, the cameras view is in spanwise direction. The FOV is indicated by a dashed rectangle. The plunging direction is denoted by $\dot{h}$, the normalized chordwise coordinate is denoted by x/c and the normalized wall-normal coordinate is denoted by y/c, using the chord length c.

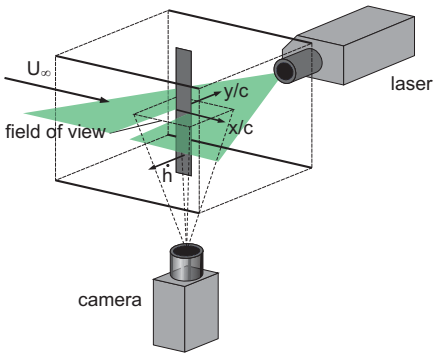

Figure 6.3: Schematic PIV setup in the water tunnel with laser light sheet, camera and airfoil, adapted from Rival *et al.* (2014)

For one plunging cycle, 786 snapshots were recorded at a repetition rate of 500 Hz in single-frame mode. The pulse duration was 350 ns. The raw data were correlated with a multi-grid algorithm with an initial interrogation area size of 128 x 128 pixels and a final interrogation area size of 16 x 16 pixels to obtain quantitative velocity fields. A 75 % overlap was chosen to retain velocity gradients. A moving average filter was used to remove outliers ($>$ 6 %) from a 3 x 3 neighborhood. To improve the salience of the coherent structures in the flow field, each interrogation was temporally smoothed using a Savitzky-Golay filter with 31 ms span. This field of view with a size of 100 mm x 100 mm resulted in approximately 100 datums per chord with an estimated velocity uncertainty of 2 % of free stream at each interrogation area.
For the analysis of the data, three independent runs were recorded and averaged. The measurement uncertainty of the lift coefficient c_l based on the standard deviation between the three independent runs is ± 0.2.
The overall negative circulation above the plate Γ is calculated by inte-

grating the negative vorticity in the integration area marked by the black dotted line in figure 6.4. The circulation of the secondary vortex caused by the boundary-layer eruption is calculated by integrating the positive vorticity in the near leading edge integration area, marked in figure 6.4 by the green triangle. Additionally, the position of the rear stagnation point has been tracked.

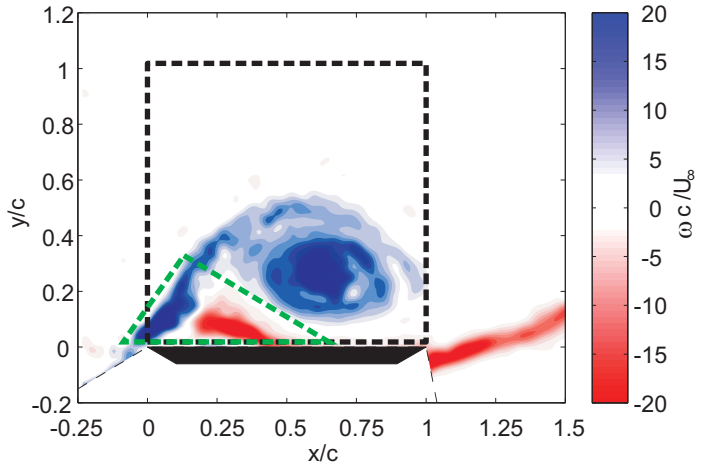

Figure 6.4: The instantaneous vorticity field at $t/T = 0.25$, overlaid with the integration areas. The black dashed line shows the region used to investigate the development of the LEV circulation above the profile, the green triangular area of integration is used to investigate the interaction between the erupting layer (red) and feeding shear layer (blue). The circulations of both structures are calculated in this area. (Adapted from Rival *et al.* (2014))

6.2 Experimental results

The impact of the various leading edge shapes is expected to be of second order, when the approximation introduced by Roshko (1954) is considered,

which states that the LEV circulation increase rate $\dot{\Gamma}^{LEV} \propto U_\infty^2$ is independent of the shear layer parameters, if a linear velocity distribution over the shear layer is assumed. The results of the PIV and direct force measurements are presented in the following paragraphs.

6.2.1 Force measurements

Figure 6.5 shows the measured time dependent lift history over one motion cycle $t/T = 0 - 0.5$ for the three leading edge types. The lift exceeds the

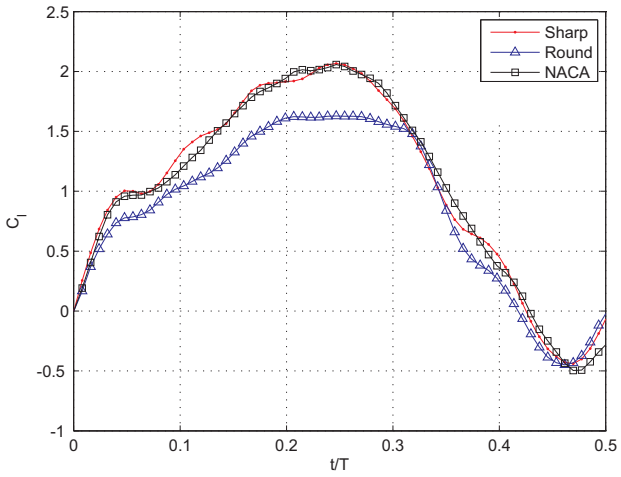

Figure 6.5: Lift history shown for the various leading-edge geometries. The peak lift is reduced for the round leading edge shape, but initial growth behavior and the decay are similar for all cases. (Adapted from Rival *et al.* (2014))

values achievable under steady conditions, indicating that dynamic stall is present on the airfoil during the motion. At $t/T \approx 0.25$ where the airfoil acceleration is negligible, high lift is achieved, which is presumably attributed to the presence of a large LEV on the airfoil. This peak in aerodynamic lift is followed by a strong decrease, which is characteristic for

deep dynamic stall and indicates LEV detachment. While the $NACA$ 0012 and the sharp edged profile exhibit strong similarity in the lift slope and the peak lift, the peak lift is reduced for the round edge. Especially around $t/T = 0.2-0.3$, when the forces are dominated by the LEV, clear differences between the three cases are visible. Therefore it can be concluded that the LEV development depends directly on the leading edge shape and thus on the shear layer parameters. More details describing the LEV dynamics cannot be derived from the lift history.

6.2.2 Flow field

PIV flow field measurements allow a more detailed insight to the LEV dynamics and their influence on the force history. The development of the LEV between all airfoil shapes can be compared by their circulation history, the development of the secondary counter-clockwise vortex near the leading edge and the position of its rear reattachment point. Figure 6.6 shows the growth of the LEV for all leading edge shapes and the development of the secondary structure below the LEV, which interacts with the feeding shear layer and may cause LEV detachment. In all cases the LEV reaches its maximum size between $t/T = 0.25$ and 0.3, when the peak lift values are observed and detaches afterwards.

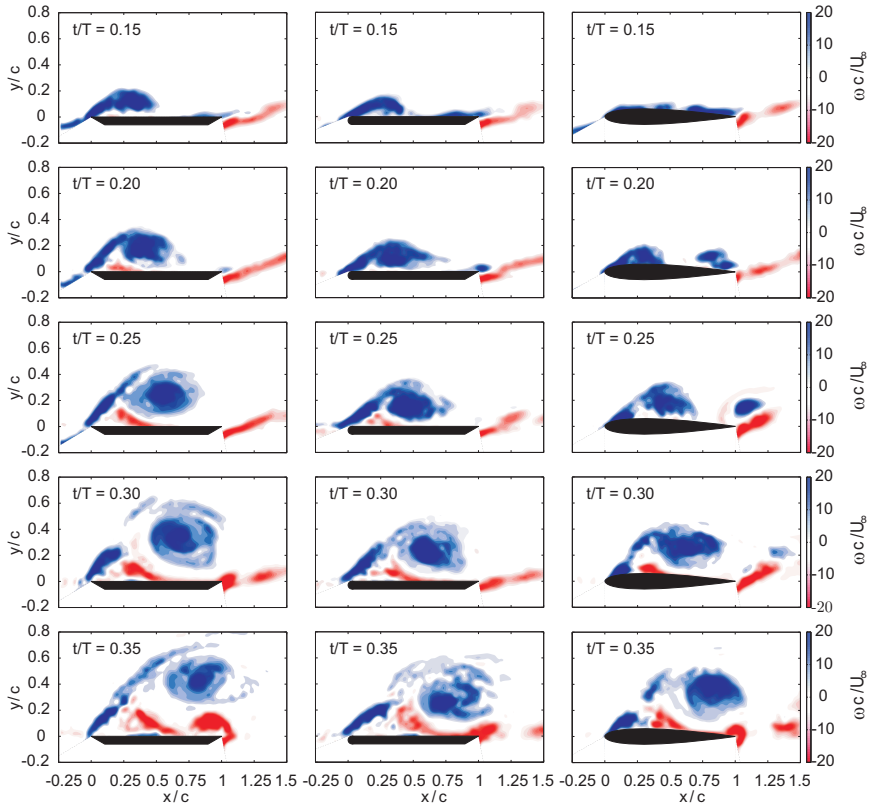

Figure 6.6: Normalized vorticity field $\omega^* = \frac{\omega c}{U_\infty}$ for sharp edged (left column), round edged (middle column) and $NACA$ 0012 (right column) profiles for $t/T = 0.15,\ 0.20,\ 0.25,\ 0.30,\ 0.35$. (adapted from Rival *et al.* (2014))

During that period, the developing boundary layer eruption and the subsequent formation of the secondary structures is clearly visible. Around $t/T = 0.25$, when the lift starts to drop, the smooth wake is replaced by the formation of a TEV. The general trends are similar for all airfoils, but the sharp edged profile seems to accelerate the flow field development compared to the other cases.
The circulation development for all three airfoil shapes is shown in figure 6.7. Again, the circulation is most advanced for the sharp edged profile, an initial lag between the onset of LEV formation is observed for the round edged and the $NACA$ 0012 profile.

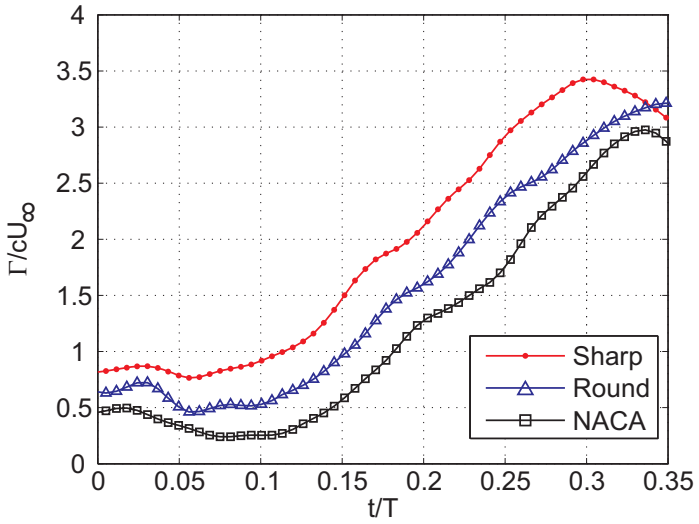

Figure 6.7: Non-dimensional LEV circulation development $\frac{\Gamma}{cU_\infty}$ for all different profiles. (adapted from Rival *et al.* (2013))

Figure 6.8 compares the normalized rates of circulation increase $\frac{T}{cU_\infty}\frac{\partial\Gamma}{\partial t}$. The initial lag is described by the distinct trough of $\frac{T}{cU_\infty}\frac{\partial\Gamma}{\partial t}$ around $t/T = 0.05$, especially for the round edged profile. After $t/T = 0.10$ an almost uniform growth rate prevails for all profiles until $t/T \approx 0.17$, when an approximately steady level is achieved. Therefore an influence of the leading edge shape on the LEV development; hence on the force history is observed.

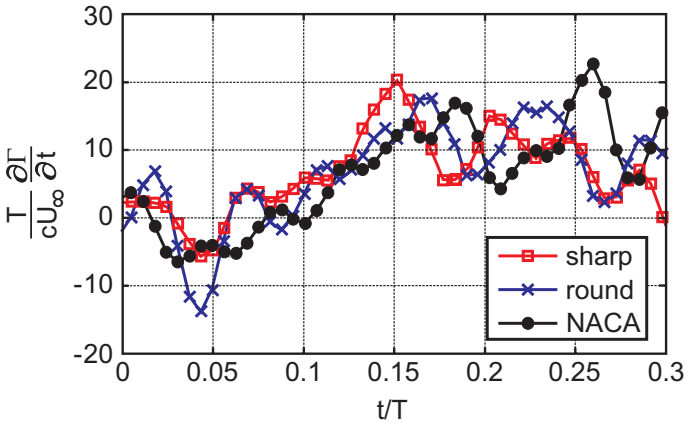

Figure 6.8: Non-dimensional growth rate of the LEV circulation $\frac{T}{cU_\infty}\frac{\partial\Gamma}{\partial t}$. (adapted from Rival *et al.* (2014))

The interaction of the secondary counter-clockwise structure and the LEV feeding layer causing detachment is illustrated in figure 6.9. It shows the evolution of clockwise and counter-clockwise circulation in the green integration triangle shown in figure 6.4. No eruption indicated by an increase in counter-clockwise circulation is detected until approximately $t/T = 0.15$. Although the clockwise circulation still continues to grow, the overall circulation stagnates and even decreases after $t/T \approx 0.22$, which shows the cross annihilation of the vorticity in both structures.

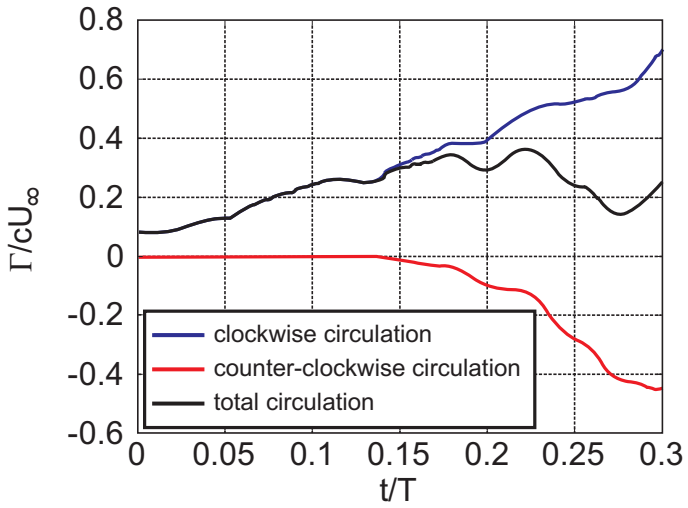

Figure 6.9: Development of the shear layer and the secondary counter-clockwise vortex near the leading edge. After $t/T = 0.15$ the boundary layer eruption takes place and cross annihilation of positive and negative circulation limiting the LEV is observed. (adapted from Rival *et al.* (2013))

6.2.3 Flow topology

Topological arguments (introduced in sections 2.6 and 2.5) are used to describe the role of the critical points on the airfoil with respect to the LEV detachment mechanism. The rear reattachment point of the LEV on the suction side of the airfoil moves towards the trailing edge edge as the vortex grows. Right at the trailing a half saddle remains constant during the LEV growth period. When the LEV reattachment point moves beyond the trailing edge, both half saddles merge and form a full saddle, which detaches from the airfoil. Their flow characteristics are combined, which allows flow reversal at the trailing edge, which causes a TEV to grow. A channel below the LEV opens and counter-clockwise is transported upstream. This detachment mechanism depends on the relative position of the rear reattachment with respect to the trailing edge, the chord length is characteristic. To support these arguments, the rear reattachment point has been tracked for the sharp and the round edged profile, and its position is compared to the lift and circulation history. Figure 6.10 shows the position of the rear reattachment point for a sharp edged and a round edged profile for one plunging motion. Again, the apparent phase lag in the trajectories corresponds to the delayed LEV circulation growth and the differences in the lift history.
Figure 6.10 shows, that the rear reattachment point reaches the trailing edge at approximately $t/T = 0.25$, merges with the half saddle and initiates flow reversal. Counter-clockwise fluid is transported upstream and connects with the secondary structure caused by the boundary-layer eruption. The LEV is separated from its feeding layer and lifts off the airfoil. This process coincides with the drop in lift at approximately $t/T = 0.25$. The chord length is the characteristic length scale for this detachment mechanism, since it determines, when an interplay of trailing-edge vorticity with the LEV feeding shear layer may occur. This statement is at least valid for the observed parameter space representing efficient forward flight. For different airfoil kinematics, angle of attack history or flow parameters k, St and Re other mechanisms may be crucial.
The airfoil shape has an impact on the LEV development. The leading edge shape is responsible for the local pressure gradient, which determines shear layer separation. For airfoils with higher leading edge curvature, the suction peak is higher and the shear layer separates earlier in the stroke cycle. The result is a phase lag in the rolling up of an LEV. During this

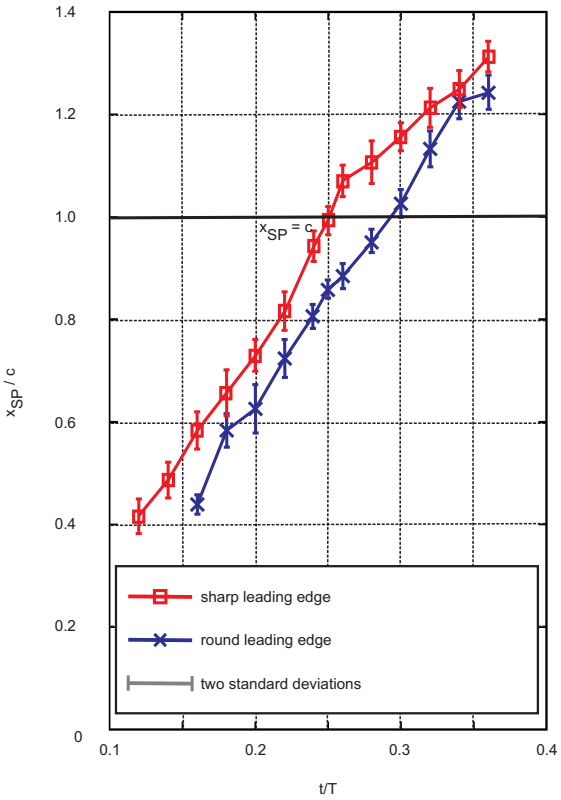

Figure 6.10: Averaged trajectories of the rear reattachment point for a sharp and a round leading edge. The observed phase lag for the round leading-edge case corresponds to the delayed LEV development and reduced lift. The error bars represent two standard deviations. (adapted from Rival *et al.* (2014))

lag, the LEV over a sharp edged airfoil can already accumulate vorticity created at the leading edge, while this vorticity is advected and does not contribute to the LEV circulation for the case of a rounded leading edge. During detachment, the LEV has the same geometrical size determined by the chord length, but a higher circulation for a sharp leading edge. The ratio of circulation to LEV changes for all airfoils. As described in section 2.3, the shear layer thickness determines the circulation-to-mass ratio of an LEV, which supports the idea, that the shear layer properties also depend on the pressure gradient determined by the leading edge shape.

7 Influence of the chord length on LEV detachment

In the following chapter the isolated influence of the chord length on the LEV detachment mechanisms is investigated. As conjectured in section 2.7 a change in the parameter κ, which depends on the airfoil kinematics leads to a transition in the LEV detachment mechanism. One non-dimensional group influencing κ is the ratio of shear layer curvature and airfoil chord length $\frac{a_0}{c}$ (see section 2.12). By increasing the chord length c, but keeping all non-dimensional parameters k, St, Re and α_{eff} constant, the bluff body detachment mechanism is presumed to be postponed to later stroke cycles. For a sufficiently low Reynolds number, the viscous effects leading to a boundary-layer eruption will occur before flow reversal at the trailing edge and the LEV will detach independently of the chord length. Its circulation is not supposed to collapse using the conventional normalization method based on the free stream velocity and the chord length.
The flow fields around four airfoils with sharp leading and trailing edges but different chord lengths $c = [90\ 120\ 15\ 180]$ mm have been investigated. A Strouhal number of $St = 0.25$ was chosen to represent high force production during a stroke cycle. The Reynolds number was adjusted to $Re = 17000$ to highlight viscous effects, and a large reduced frequency of $k = 0.5$ is chosen to underline unsteady effects. To keep the non-dimensional parameters k, St, Re and α_{eff} constant, the free stream velocity U_∞, the motion period T and the plunging height Δh have to be adjusted accordingly and summarized in table 7.1.

An attempt to keep the shear layer curvature independent of the flow conditions was made by choosing a sharp leading edge. Thus, the shear layer curvature does not appear as an additional influencing parameter. However, the shear layer thickness is presumed to change with the free stream velocity and thus alter the ratio of mass and circulation transported from the shear layer into the LEV. The four different airfoils are schematically show in figure 7.1, the angle of the leading edge is $\Theta = 30°$.

Chord length c [mm]	Free stream velocity U_∞ $[\frac{\text{m}}{\text{s}}]$	Motion period T [ms]	Plunging height Δh [mm]
$c = 90$	3.0	95	71
$c = 120$	2.25	167	94
$c = 150$	1.8	262	118
$c = 180$	1.5	377	141

Table 7.1: Dimensional experimental parameters for the four test cases with varying chord length. (Adapted from Widmann and Tropea (2015))

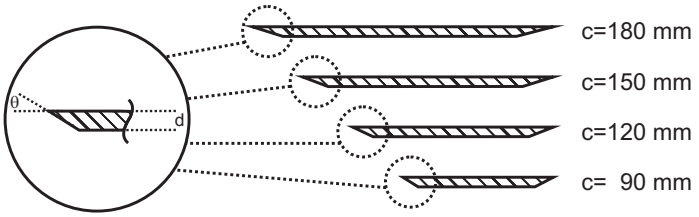

Figure 7.1: Geometry of the flat plates with different chord lengths (Adapted from Widmann and Tropea (2015))

At the instant of eruption caused LEV detachment, boundary-layer eruption depends only on the state of the LEV, which in turn is determined exclusively by the transport of fluid out of the shear layer, because the trailing edge does not influence the LEV development. Ultimately, this state of the LEV at detachment only depends on the shear layer properties and may be normalized by them. Therefore an alternative normalization method for the LEV circulation is proposed: $\frac{\Gamma^{LEV}}{\delta_{SL} U_\infty}$.

7.1 Flow fields

The instantaneous time resolved vorticity fields for the flow fields around each airfoil are shown in figure 7.2. The normalized vorticity $\omega^* = \frac{\omega c}{U_\infty}$ is color coded, with blue as clockwise oriented rotation and red as counter-clockwise oriented rotation. The instantaneous streamlines are superimposed onto the vorticity fields. Each row shows the LEV development for a constant chord length, each column shows the fixed time steps $t/T = [0.18\ 0.22\ 0.26\ 0.30]$. The regions below and upstream of the airfoil were masked out due to shadowed regions of the FOV. In all cases a distinct vortex develops from the leading edge, grows and detaches from the airfoil. With increasing time t/T a layer of counter-clockwise vorticity develops below the LEV due to the no-slip condition. Subsequently secondary vortical structures occur near the leading edge and a full saddle point above the leading edge appears, which initiates the LEV detachment by a redistribution of fluid emerging from the shear layer into the tertiary structure, as described in section 2.6. For the flow around an airfoil with $c = 90$ mm, secondary structures representing a topological change at the leading edge and leading to the LEV detachment do not develop, until flow reversal occurs around $t/T \approx 0.22$. The chord length seems to be limiting LEV growth for $c = 90$ mm. For all other cases with higher chord lengths, the secondary structures start to form independently of the trailing edge flow reversal; the chord length is not a characteristic length scale. The area covered by the LEV is increased with decreasing free stream velocity, which agrees with the theoretical considerations presented in section 2.3.

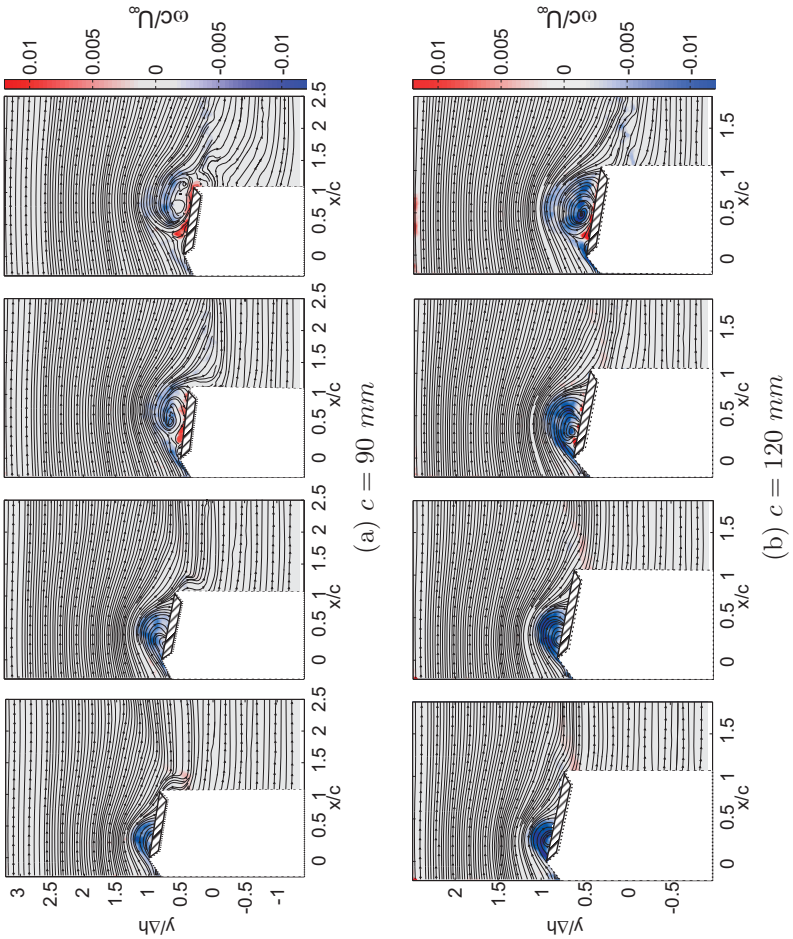

(a) $c = 90\ mm$

(b) $c = 120\ mm$

Figure 7.2: Time resolved development of the normalized vorticity field ω^* at $t/T = [0.18\ 0.22\ 0.26\ 0.30]$ for $c = [90\ 120]$ mm. (Adapted from Widmann and Tropea (2015))

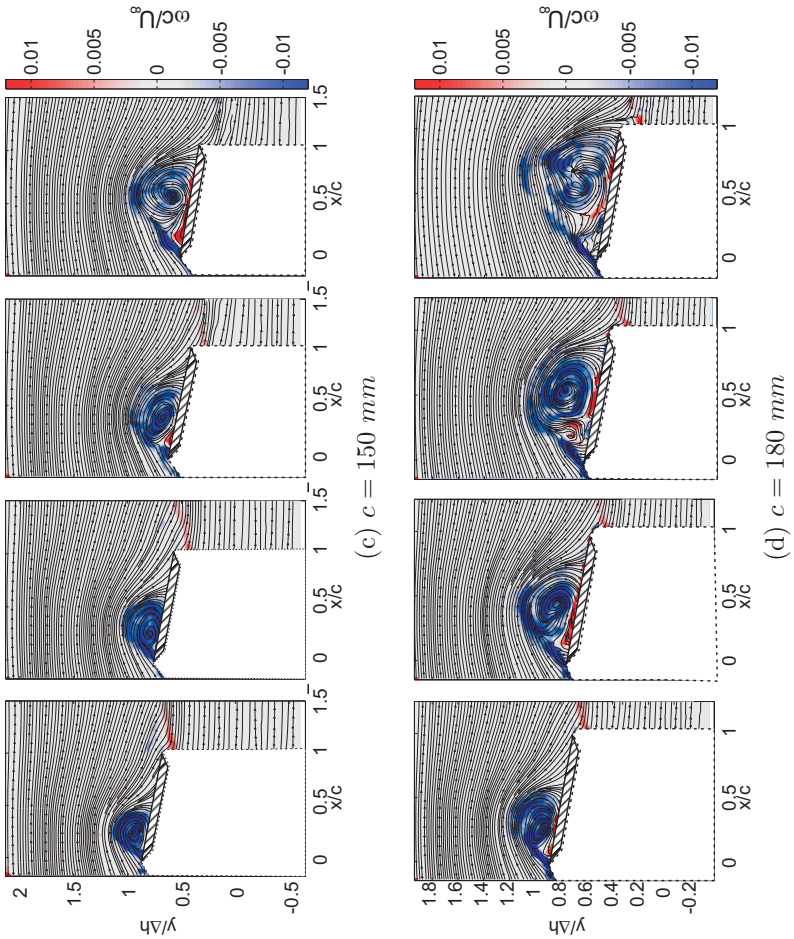

(c) $c = 150\ mm$

(d) $c = 180\ mm$

Figure 7.2: Time resolved development of the normalized vorticity field ω^* at $t/T = [0.18\ 0.22\ 0.26\ 0.30]$ for $c = [150\ 180]$ mm. (Adapted from Widmann and Tropea (2015))

7.2 Results: chord based normalization of the circulation

Figure 7.3 shows the normalized LEV circulation $\frac{\Gamma^{LEV}}{cU_\infty}$ for all cases. The error bars indicate the run-to-run standard deviation. The instants in the stroke cycle t/T when flow reversal occurs and the averaged rear LEV reattachment point X_{SP} reaches the trailing edge ($\frac{X_{SP}}{c} = 1$) are marked with vertical dashed lines. The position of the rear stagnation point X_{SP} at that instant is not greater than 5% of the chord length in all cases. The instant when $X_{SP} = c$ is shifted towards earlier time steps for shorter chord lengths, indicating smaller relative LEV sizes with an increasing free stream velocity, due to thinner shear layers, which correspond to the theoretical considerations in section 2.3. The circulation peaks are chosen as the instant of LEV detachment, since these instants agree with a sudden decrease of LEV convection speed (see section 5) and agree with the definition of Fage and Johansen (1928).

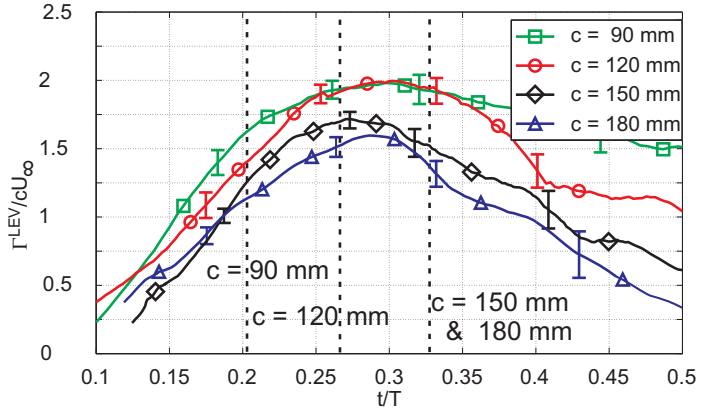

Figure 7.3: Chord-based normalized LEV circulation $\frac{\Gamma^{LEV}}{cU_\infty}$ (Adapted from Widmann and Tropea (2015))

The circulation curves exhibit the same trend and a similar slope during the LEV growth period. Despite these overall characteristics and the constant non-dimensional parameters for all airfoils, the curves do not col-

lapse. Their peak values exhibit a significant deviation from each other, which means that that the airfoil chord is not a characteristic length scale throughout all experimental cases. Although the normalized circulation peaks for $c = 90$ mm and $c = 120$ mm have the same level, lower peak values are found for $c = 150$ mm and $c = 180$ mm. The circulation peak for $c = 90$ mm is reached well after flow reversal at the trailing edge. For $c = 120$ mm the circulation peak roughly coincides with the flow reversal. The peak circulation for these cases corresponds with the peak circulation observed by Baik *et al.* (2012) for a similar reduced frequency. All three peak circulation values agree, because the LEV detachment can be assigned in all three cases to the bluff body detachment mechanism. For $c = 150$ mm and $c = 180$ mm the circulation peak occurs well before the flow reversal, which shows that the chord length is not characteristic under the conditions for these cases.

7.3 Results: secondary structures

More information about the detachment for all cases can be gathered by considering the development of the secondary vortical structures near the leading edge. Its normalized circulation evolution $\frac{\Gamma^{Eruption}}{cU_\infty}$ is shown in figure 7.4.

While the LEV behavior is similar for all chord lengths, the development of the secondary vortex is completely different. In case $c = 90$ mm a secondary vortex is found early in the stroke cycle, which directly follows $\frac{X_{SP}}{c} = 1$. For all other cases the onset of a secondary structure is observed before $\frac{X_{SP}}{c} = 1$, therefore for $c = 150$ mm and $c = 180$ mm these structures form independent of the chord length. For $c = 120$ mm the flow reversal and the onset of secondary vortex formation roughly coincides. These observations indicate bluff body vortex detachment in the case $c = 90$ mm on one hand and eruption caused vortex detachment in the cases $c = 150$ mm and $c = 180$ mm on the other. It is expected that the circulation curves for $c = 150$ mm and $c = 180$ mm collapse for the alternative normalization. Both events roughly coincide in the case $c = 120$ mm, therefore the LEV detachment may be a mixture of both mechanisms. The case $c = 120$ mm may indicate the flow conditions, under which a transition from one detach-

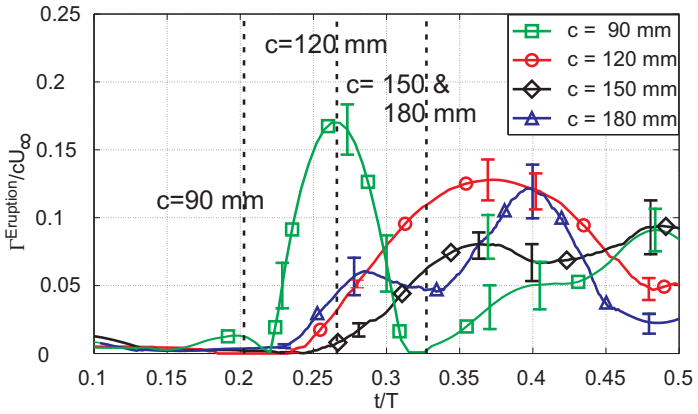

Figure 7.4: Chord-based normalized eruption circulation $\frac{\Gamma^{Eruption}}{cU_\infty}$ (Adapted from Widmann and Tropea (2015))

ment to the other takes place and a practical value for κ_{trans} (limited to the investigated kinematics) may be derived from this experimental case. The fractional convection rate $k^* = \frac{\Gamma^{LEV}}{4\pi y_{LEV} U_\infty}$ introduced by Doligalski *et al.* (1994) provides information about the onset of the boundary-layer eruption. It is estimated experimentally by tracking the wall-normal distance of the vortex center to the airfoil surface y_{LEV} and computing the LEV circulation Γ^{LEV}. According to Doligalski *et al.* (1994), the onset of the boundary-layer eruption is connected to the excess of a critical value in k^*. The fractional convection rate for all cases is shown in figure 7.5.

While k^* for $c = 90$ mm is low, larger values are found for the cases $c = 120$ mm, $c = 150$ mm and $c = 180$ mm. Again, the peak values occur independent of the flow reversal for $c = 150$ mm and $c = 180$ mm. These observations suggest, that the critical value of k^* is reached for higher chord lengths, but not for $c = 90$ mm. The lack of collapse of k^* between all cases may therefore be attributed to different detachment mechanisms and the chord length is not the proper scaling parameter for all cases. Instead of the chord based normalization, the next section describes a normalization approach based on the shear layer parameters.

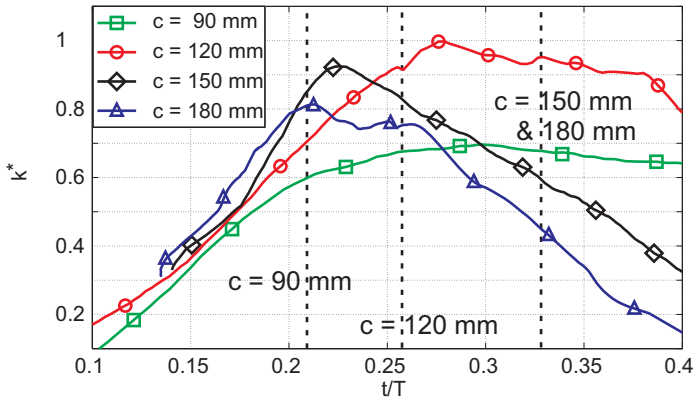

Figure 7.5: Vortex induced normalized velocity k^* causing the eruptive boundary layer response and formation of secondary structures according to Doligalski *et al.* (1994). (Adapted from Widmann and Tropea (2015))

7.4 Shear layer based normalization

The above hypothesis of a shear layer based normalization is tested in this section. The shear layer thickness δ_{SL} as a characteristic parameter characteristic is used to normalize the circulation curves presented in figure 7.3. At least those curves are expected to collapse, whose LEV detachment cannot be attributed to the flow reversal at the trailing edge. The shear layer thickness at the leading edge is not accessible experimentally, since this region was shadowed during the PIV measurements. In addition, the thin layer cannot be resolved by a large FOV. To estimate the shear layer thickness, it was assumed that the shear layer develops from a stagnation point ($m = 1$) and that the Falkner-Skan equation $\delta_{SL} = 2.4\sqrt{\frac{\nu}{a}}$ (Schlichting and Gersten (2001)) can be used to compute its thickness. The parameter a is determined by the local flow field in the vicinity of the stagnation point and reads $a = \frac{U(x,y)}{x} = \frac{-V(x,y)}{y}$ (with the origin of the coordinate system ([x y] = [0 0]) placed at the stagnation point). Again, this value cannot be estimated experimentally, therefore potential flow theory has been used instead. A flat plate inclined at the maximal effective angel of attack $\alpha_{eff,max} = 30°$ under the assumptions of steady inviscid

flow and neglecting the influence of the LEV attached to the airfoil suction side was computed for all four chord lengths and a is then replaced by the term $a = a_0 U_\infty$. The parameter a_0 is extracted from a circular region in the potential flow field with 10 % of the chord length around the stagnation point and yields $a_0 = [2.77\ 2.78\ 2.75\ 2.76]\ \frac{1}{\mathrm{m}}$ with a corresponding standard deviation of $\sigma(a_0) = [6.40\ 6.48\ 5.82\ 5.76]$ %. The assumptions seem to be correct since in all cases a_0 is uniform in the circular region around the stagnation point, implying prevailing stagnation point flow for the parameter $m = 1$. The mean value $\overline{a}_0 = 2.765\ \frac{1}{\mathrm{m}}$ is used to compute the shear layer thickness: $\delta_{SL} = 2.4\nu^{0.5}\overline{a}_0^{-0.5}U_\infty^{-0.5}$. The alternative LEV normalization is then given in equation 7.1.

$$\Gamma^* = \frac{\Gamma^{LEV}}{\delta_{SL} U_\infty} = \frac{\overline{a}_0^{0.5}}{2.4\nu^{0.5}} \frac{\Gamma^{LEV}}{U_\infty^{0.5}} \tag{7.1}$$

The alternative normalization of the LEV circulation is shown in figure 7.6. While the circulation curves collapse for the cases $c = 120$ mm, $c = 150$ mm and $c = 180$ mm, which detach due to the boundary-layer eruption, the normalization fails for the of $c = 90$ mm, when LEV detachment occurs due to the bluff body mechanism.

Taking the theoretical considerations into account, the collapse may be explained: The ratio of circulation to mass transport into the LEV decreases with higher chord lengths (from higher free stream velocities and thinner layer to lower free stream velocities and thicker shear layers). With an increasing shear layer thickness the vorticity fed to the LEV is lower and the LEV has to accumulate more mass to achieve the same circulation. The velocity gradients are smaller for lower higher chord lengths and the LEV is less compact. The role of the viscosity can be estimated, if a Reynolds number based on the LEV circulation $Re_{LEV} = \frac{\Gamma^{LEV}}{\nu}$ is defined. This Reynolds number decreases with increasing chord lengths, leading to an emphasis of viscous effects, including the boundary-layer eruption.
In summary, a combination of an interaction prone shear layer (at low free stream velocities and low vorticity for larger chord lengths) and the formation of secondary structures at the leading edge may lead to LEV detachment instead of the bluff body mechanism, if the flow conditions permit a sufficient viscous response. A dependency of the maximal LEV

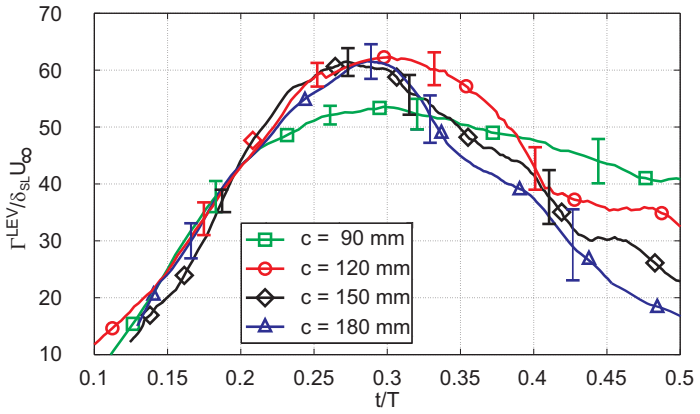

Figure 7.6: Normalized LEV circulation based on the shear layer properties according to equation 7.1 (Adapted from Widmann and Tropea (2015))

circulation on the shear layer properties has already been shown by Rival *et al.* (2008) and (2014). Additionally, Sattari *et al.* (2012) find vortex detachment from a shear layer in absence of any geometrical length scale and attribute the vortex growth and detachment to the instantaneous velocity profile of the shear layer.
These viscous effects are assumed to play only a role at low Reynolds number, since the change in the shear layer thickness quickly decreases ($\frac{\partial \delta_{SL}}{\partial U_\infty} \propto U_\infty^{-3/2}$) for increasing free stream velocities. The eruption caused LEV detachment mechanism is therefore then limited to certain parameters, with large reduced frequencies and low Reynolds numbers.

8 Influence of the reduced frequency on LEV detachment

This section deals with the last non-dimensional parameter influencing LEV detachment, which has been identified in section 2.12. Besides the Reynolds number, the shear layer curvature and chord length ratio investigated in sections 5, 6 and 7, the reduced frequency k affects the LEV detachment behavior and is examined in this section. This perspective is supported by the findings of Baik *et al.* (2012), who vary the Strouhal number and reduced frequency systematically and find that the reduced frequency is primarily responsible for the evolution of flow topology, while the Strouhal number primarily determines the force production. The reduced frequency determines the time scales of airfoil motion with respect to the free stream velocity. A variation of the reduced frequency leads to a change in the competing time scales of the airfoils motion and the LEV inherent formation time, which depends only on the free stream velocity (see equation 2.6). As a consequence the same LEV occurs for different reduced frequencies at different effective angles of attack, which determines the instantaneous shear layer properties. The shear layer is resistant against the interaction with structures of opposite rotating vorticity, when the velocity difference over the shear layer is large, as shown by Rival *et al.* (2008). This state occurs for a large plunging velocity and large instantaneous effective angles of attack around $t/T \approx 0.25$. At these instants the velocity component perpendicular to the airfoil, which determines the shear layer velocity gradient is large. For earlier time steps with $t/T < 0.25$ the maximum velocity difference over the shear layer has not been reached yet, for later time steps $t/T > 0.25$ the maximum effective angle of attack has been crossed already and decreases further. In both situations the shear layer is more and more unstable against an interaction, the further the instant of interaction digresses from $t/T \approx 0.25$. Therefore two extreme cases of LEV detachment related to the reduced frequency can be identified:

1. Low reduced frequencies: The LEV can grow for a long period (given by the comparatively large motion period of the airfoil), reaches the airfoil trailing edge well before the maximal angle of attack occurs in the stroke cycle and subsequently detaches due to the flow reversal at the trailing edge. As a consequence a TEV forms after LEV detachment, because the pressure difference at the trailing edge increases and strengthens the flow reversal. A low LEV circulation is expected due to the shear layers susceptibility at low angles of attack.

2. High reduced frequencies: At high reduced frequencies the LEV grows for a short period, limited by the rapid airfoil motion. The maximum angle of attack has long been exceeded before the LEV has grown enough to initiate flow reversal at the trailing edge. The pressure gradient at the leading edge rises, because the effective angle of attack and the resulting suction peak decrease. This pressure gradient provokes a boundary-layer eruption and together with the susceptible shear layer the LEV detachment is initiated. This perspective is in agreement with the findings of Ramesh *et al.* (2014). As a consequence, the airfoil kinematics determine the instant of LEV detachment at high reduced frequencies as a result of boundary-layer eruption due to a rise in the leading edge pressure gradient. The LEV detachment is independent of the flow reversal and the chord length and the pressure different at the trailing edge is small due to a small (and decreasing) angle of attack. Therefore no TEV growth is expected.

In a region between high and low reduced frequencies a certain reduced frequency needs to exist, which tunes into the LEV growth period in such a way, that the maximum effective angle of attack (resulting in the most resistent shear layer with the largest velocity difference) and the flow reversal at the trailing edge coincide. For this case the highest amount of circulation is presumed to be stored in the LEV. Because the LEV detachment is determined by the interaction between secondary structures and the feeding shear layer, a normalization based on the instantaneous velocity perpendicular to the airfoil surface (determining the shear layer parameters) compensates for the expectedly different LEV circulations for different reduced frequencies.

The flow fields around an airfoil with sharp leading and trailing edges and a chord length of $c = 120\ mm$ in combined pitching and plunging motion at four different reduced frequencies are investigated. The airfoil executes a sinusoidal plunging motion, the geometric angle of attack has been adjusted in a way that the effective angle of attack follows $\alpha_{eff}(t/T) = 30°sin(2\pi t/T)$. The Strouhal number based on the trailing edge displacement during one stroke cycle is $St = 0.20$, which is representative of efficient forward flight according to Triantafyllou *et al.* (2004). The Reynolds number is set to $Re = 24000$, representing realistic flight conditions. Four different reduced frequencies $k = [0.16\ 0.24\ 0.32\ 0.48]$ are investigated to identify the influence of the airfoil time scale on the LEV formation and detachment process. The highest reduced frequency $k = 0.48$ has been selected to provoke a transition in the LEV detachment mechanism, which is expected to occur above a certain reduced frequency. To vary the non-dimensional parameter k, but keep St, Re and α_{eff} constant, the free stream velocity U_∞, the motion period T and the plunging height Δh have to be adjusted accordingly and their dimensional values are summarized in table 8.1.

Test case	chord length c [mm]	Free stream velocity U_∞ $[\frac{\mathrm{m}}{\mathrm{s}}]$	Motion period T [ms]	Plunging height Δh [mm]
$k = 0.16$	120	3.2	736	236
$k = 0.24$	120	3.2	491	157
$k = 0.32$	120	3.2	368	118
$k = 0.48$	120	3.2	245	79

Table 8.1: Dimensional experimental parameters for the four test cases with varying reduced frequency. (Adapted from Widmann and Tropea (2015))

8.1 Flow fields

The time-resolved flow fields for all four reduced frequencies $k = 0.16$, $k = 0.24$, $k = 0.32$ and $k = 0.8$ are shown in figure 8.1. The normal-

ized vorticity field $\omega^* = \frac{\omega c}{U_\infty}$ is color coded (red as clockwise vorticity and blue as counter-clockwise vorticity). The local flow velocity is indicated by vectors at each every second IA. The constant time steps $t/T = [0.15\ 0.25\ 0.35\ 0.45]$ are shown in the single column in figure 8.1, the flow field development for each reduced frequency is shown in each row. A distinct LEV develops in all cases. As expected, its development compared to the airfoil motion period is faster for low reduced frequency and delayed for high reduced frequencies. In later stages of the airfoil motion a TEV starts to form for the cases $k = [0.16\ 0.24\ 0.32]$. For case $k = 0.48$ the LEV detaches late in the stroke cycle at small angles of attack before its rear reattachment reaches the trailing edge and no TEV forms. Instead a secondary at the leading edge forms around $t/T \approx 0.45$ and alters the flow topology.

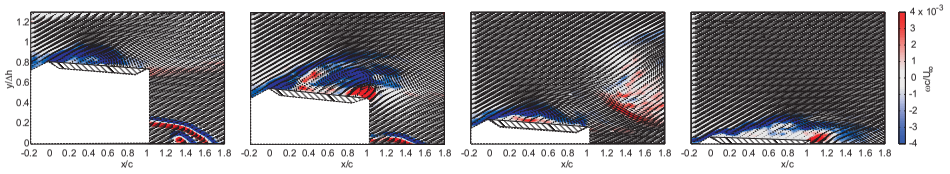

(a) $k = 0.16$

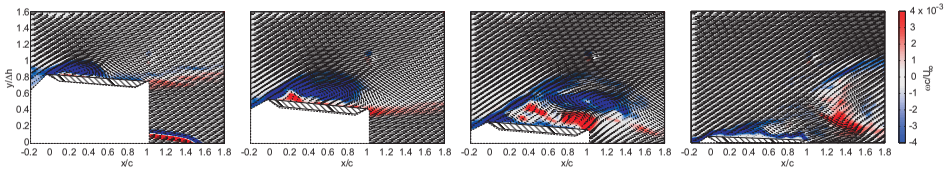

(b) $k = 0.24$

Figure 8.1: Flow field development in terms of normalized vorticity and velocity vectors for different reduced frequencies and $t/T = [0.15\ 0.25\ 0.35\ 0.45]$. (Adapted from Widmann and Tropea (2015))

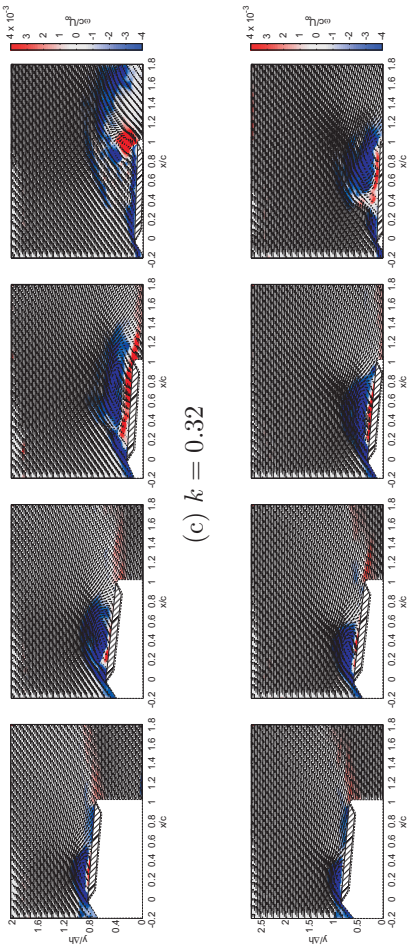

(c) $k = 0.32$

(d) $k = 0.48$

Figure 8.1: Flow field development in terms of normalized vorticity and velocity vectors for different reduced frequencies and $t/T = [0.15\ 0.25\ 0.35\ 0.45]$. (Adapted from Widmann and Tropea (2015))

8.2 Results: chord based normalization of the circulation

The LEV circulation Γ^{LEV} and all clockwise circulation stored in the identified vortical structures Γ^{-} is extracted from the velocity fields and shown in figure 8.2 in its normalized form for all cases. The divergence between Γ^{LEV} and Γ^{-} indicates the starting formation of a secondary clockwise oriented vortex near the leading edge. The instants in the airfoil motion period when the LEV rear reattachment point reaches the trailing edge $X_{SP} = c$ and initiates flow reversal are marked by vertical dashed lines. The maximum achievable circulation varies from case to case: For $k = 0.24$ it reaches a peak value of $\frac{\Gamma^{LEV}}{cU_\infty} = 3.3$, which corresponds to the level of circulation predicted by the concept of optimal vortex formation for airfoils in the range $k = 0.2 - 0.25$ and $St = 0.2 - 0.3$. The peak values for all other cases are significantly lower. With increasing reduced frequency, the peaks are shifted towards later stages in the airfoil motion cycle. The peak values correspond to the circulation peak values found Baik *et al.* (2012) by for comparable non-dimensional parameters.

Γ^{LEV} drops immediately after flow reversal at the trailing edge for case $k = 0.16$, which indicates LEV detachment due to an interaction of the weak shear layer (at a low angle of attack and a low plunging velocity) with the counter clockwise fluid transported upstream. The LEV behavior in case $k = 0.24$ is similar. The LEV detaches after $X_{SP} = c$, but the shear layer is much more resistent against an interaction and feeds the LEV for a longer period, increasing its circulation. Note the circulation for $k = 0.16$ and $k = 0.24$ reach the same level, when $X_{SP} = c$. The peak in LEV circulation roughly in cas $k = 0.32$ coincides with $X_{SP} = c$. Only the circulation peak $\frac{\Gamma^{LEV}}{cU_\infty}$ for $k = 0.48$ shows a different behavior. It reaches a plateau around $t/T \approx 0.3$ before $X_{SP} = c$ and starts to deviate from $\frac{\Gamma^{-}}{cU_\infty}$ well before the LEV rear reattachment reaches the trailing edge. Its limiting mechanism is not associated with the flow reversal.
To cross check the idea that the LEV detachment for case $k = 0.48$ is not linked to the bluff body mechanism, the TEV formation for all cases was observed. Figure 8.3 shows the normalized TEV circulation $\frac{\Gamma^{TEV}}{cU_\infty}$ for all reduced frequencies. For the cases $k = [0.16\ 0.24\ 0.32]$ the formation of a distinct TEV can be observed. For $k = 0.48$ only a wake forms behind the

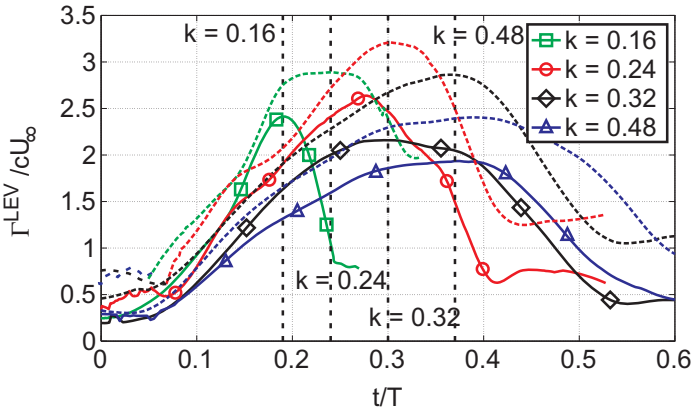

Figure 8.2: Comparison of the entire normalized circulation produced at the leading edge $\frac{\Gamma^{-}}{cU_\infty}$ (dashed lines) and the normalized circulation attributed to the LEV $\frac{\Gamma^{LEV}}{cU_\infty}$ (solid lines). (Adapted from Widmann and Tropea (2015))

airfoil. The decreasing magnitude for $\frac{\Gamma^{TEV}}{cU_\infty}$ increasing k may be an effect of reduced angles of attack during flow reversal.

8.3 Results: secondary structures

Additionally, figure 8.4 shows the evolution of the secondary vortical structures near the leading edge. For higher reduced frequencies ($k = 0.32$ and $k = 0.48$), distinct structures develop independently of the flow reversal at the trailing edge and reach a considerable strength even before counter clockwise fluid is transported upstream from the trailing edge. The peak values of the circulation of these secondary structures $\Gamma^{Eruption}$ coincide with the peaks in Γ^{LEV}, indicating their impact on the LEV limitation. Their occurrence may explain the different detachment behavior. For lower reduced frequecies ($k = 0.16$ and $k = 0.25$) the secondary structures exhibit significant levels of circulation only after $X_{SP} = c$. The magnitude of $\Gamma^{Eruption}$ is higher for $k = 0.24$, while for higher ($k = 0.32$ and $k = 0.48$)

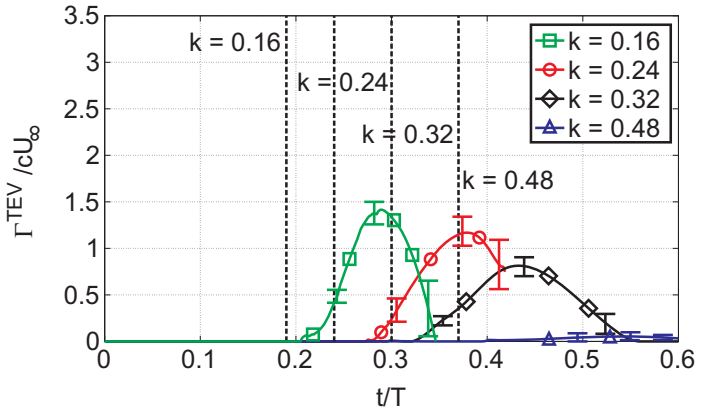

Figure 8.3: TEV circulation development for different reduced frequencies. (Adapted from Widmann and Tropea (2015))

and lower ($k = 0.16$) reduced frequencies smaller secondary structures are sufficient to cause detachment due to a weaker shear layer.

8.3.1 Results: LEV growth rate and airfoil motion period

To check the assumption, that the LEV growth is independent of the airfoil motion period, the growth in LEV circulation is plotted against the convective time $t^* = \frac{tU_\infty}{c}$ in figure 8.5. It can be seen, that the circulation growth rate is similar for all four cases, independent of the reduced frequency. Even the peak circulation values are reached around a similar convective of $t^* = 2.2 - 2.5$.

Since the LEV exhibits a constant growth rate, changing the reduced frequency causes a phase shift between LEV state and the effective angle of attack history $\alpha_{eff}(t/T)$. Therefore, an optimal reduced frequency exists, which leads to the maximum achievable LEV circulation. The achievable amount of LEV circulation decreases with a deviation of the reduced frequency from the optimal value. While at lower reduced frequencies the flow reversal is still characteristic for LEV detachment, at high reduced frequencies the increasing pressure gradient given by the low angles of attack provoke boundary-layer eruption and a subsequent LEV detachment,

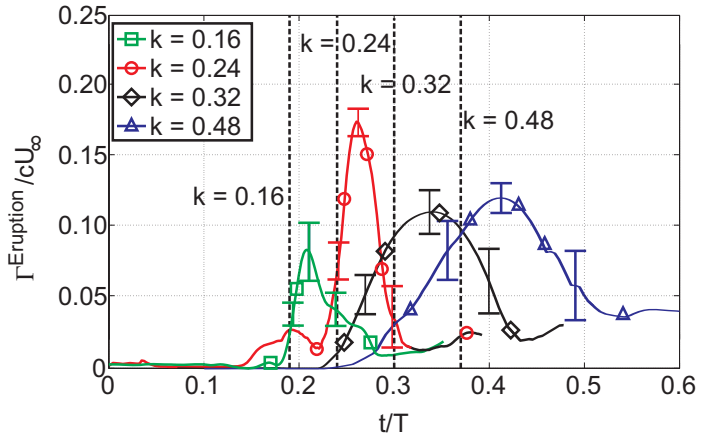

Figure 8.4: Development of the normalized circulation of the secondary vortex structure $\frac{\Gamma^{Eruption}}{cu_\infty}$ near the leading edge for different reduced frequencies. (Adapted from Widmann and Tropea (2015))

which depends only on the airfoil kinematics. Therefore a high reduced frequency exists, at a transition between both detachment mechanisms occurs, which is consistent with the implications of equation 2.12.

8.4 Results: Normalization based on the instantaneous velocity perpendicular to the airfoil

A normalization method of the LEV circulation, which accounts for the weaker shear layers has been addressed above. The peak LEV circulation is not normalized with free stream velocity, but with the velocity perpendicular to the airfoil $U_\perp$ (and therefore characteristic for the shear layer) at LEV detachment. The characteristic length of this normalization method is the chord, implying validity only for cases in which LEV detachment is caused by the flow reversal. $U_\perp(t/T) = U_{eff}(t/T)sin\alpha_{eff}(t/T)$ can be ex-

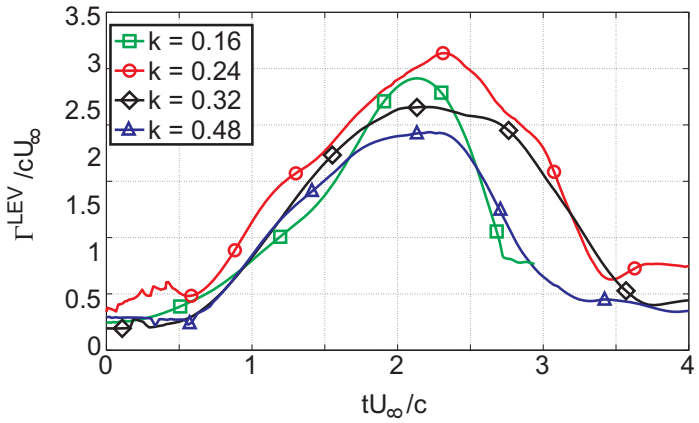

Figure 8.5: LEV circulation development for different reduced frequencies over the convective time scale $t^* = \frac{tU_\infty}{c}$. (Adapted from Widmann and Tropea (2015))

pressed by the effective velocity $U_{eff} = \sqrt{U_\infty^2 + \dot{h}(t/T)^2}$, which is the vectorial addition of the free stream velocity and the instantaneous plunging speed $\dot{h}(t/T)$ and the effective angle of attack $\alpha_{eff}(t/T) = 30°sin(2\pi t/T)$. The normalization then yields $\Gamma^* = \frac{\Gamma^{LEV}}{cU_\perp}$.

The conventionally normalized LEV circulation peak values are $\frac{\Gamma^{LEV}}{cU_\infty} = [2.42\ 2.65\ 2.27\ 1.93]$ and occur at $t/T = [0.18\ 0.27\ 0.33\ 0.34]$, just prior to LEV detachment or when a circulation plateau is reached. Figure 8.6 then compares both normalization methods. The normalization method using the free stream velocity as reference $U_{ref} = U_\infty$ is indicated by circles, the method using $U_{ref} = U_\perp$ as a reference is indicated by crosses. The non-dimensional circulation $\frac{\Gamma^{LEV}}{cU_{ref}}$ is de-normalized using $\Gamma^*_{ref} = \frac{1}{3}(\frac{\Gamma(k=0.16)}{cU_{ref}} + \frac{\Gamma(k=0.24)}{cU_{ref}} + \frac{\Gamma(k=0.32)}{cU_{ref}})$, which is defined as the mean value of the peak circulations for the reduced frequencies $k = 0.16$, 0.24 and 0.32, in order to highlight relative case to case variation for both normalization methods.

For $U_{ref} = U_\infty$ the normalized peak circulations exhibits a strong variation, while much more uniform values are obtained for $U_{ref} = U_\perp$, at least for the cases in which LEV detachment is determined by the chord

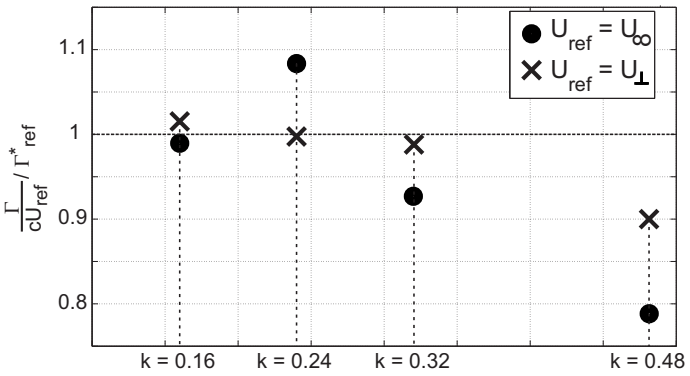

Figure 8.6: Comparison of the LEV circulation, normalized using $U_{ref} = U_\infty$ (indicated by circles) and using $U_{ref} = U_\perp$ at the LEV detachment instant (indicated by crosses). (Adapted from Widmann and Tropea (2015))

length. The peak circulation for $k = 0.48$ does not collapse for both methods. It can be seen that the normalized circulation peak values collapse, if the parameters determining the boundary-layer velocity difference at the instants of detachment are used. The conventional normalization based on the free stream velocity fails to incorporate the effects of the changed angle of attack history for different reduced frequencies.
In summary it can be said, that a transition in the LEV detachment mechanisms occurs at a high reduced frequency. Above that frequency the LEV detachment is driven by the boundary-layer eruption, which occurrence depends on airfoil kinematics. Below that critical reduced frequency, the LEV detaches as consequence of flow reversal. An optimal reduced frequency exists, which leads to the highest LEV circulation values due to a high velocity difference over the shear layer. The lower circulation peak values for reduced frequencies deviating from the optimal value can be compensated by considering the instantaneous velocity components perpendicular to the airfoil for an alternative normalization method.

9 Transition prediction of the LEV detachment mechanisms

As shown in section 2.7, in equation 2.12 the non-dimensional parameters Re, k and $a_0 c$ (for fixed airfoil kinematics) can be combined in a another non-dimensional parameter κ, which describes the geometrical ratio between the airfoil chord length and the LEV diameter (and hence to which extent the LEV covers airfoil suction side) as a function of mass transferred into the LEV during one stroke cycle. It is conjectured that the bluff body like mechanism causes the LEV to detach, if the mass transferred into the LEV during a stroke cycle is large and the LEV detaches independent of the chord length, if a boundary-layer eruption occurs before the LEV has accumulated sufficient mass to initiate the flow reversal at the trailing edge. Therefore a critical value κ_{trans} determines, for which covering ratio (for given kinematics) a transition between both LEV detachment mechanisms occurs. As seen in section 7, for the case of $c = 120$ mm both detachment mechanisms roughly coincide and therefore κ_{trans} can be computed by inserting the relevant parameters of that specific case, yielding $\kappa_{trans} = 0.358$. κ can now be calculated for each individual experimental case to predict the respective LEV detachment mechanism and then be compared with the experimental results to check for validity of the concept.

Figure 9.1 shows the computed covering ratios for experimental case presented in section 7 as dots. The horizontal dashed line represents the critical covering ratio $\kappa_{trans} = 0.358$. For the case of $c = 90$ mm the covering ratio is above the critical value, thus predicting bluff body like LEV detachment, which agrees with the results presented in section 7. The case of $c = 120$ mm represents per definition the transitional case, when both detachment mechanisms coincide. The covering ratios for $c = 150$ mm and $c = 180$ mm fall below the transitional value and their self-induced detachment behavior is predicted correctly.

This prediction method has extended uing the results presented in section 8 and again checked for validity. Figure 9.2 shows the computed κ values

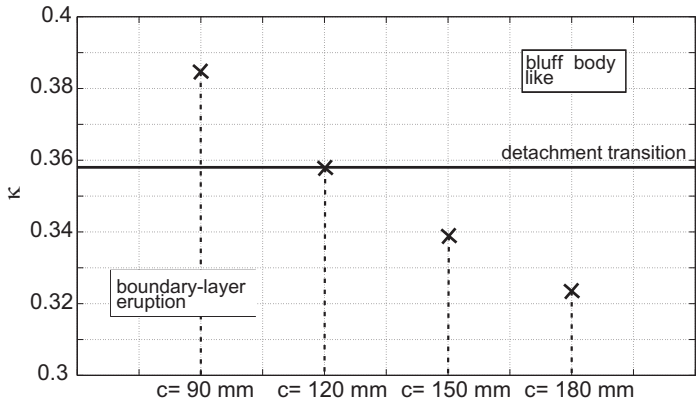

Figure 9.1: Estimated transitional conditions for the LEV detachment mechanisms at $\kappa_{trans} = 0.358$ and κ values for each set of parameters for different chord lengths, shown as dots. (Adapted from Widmann and Tropea (2015))

for the experimental cases with varying reduced frequency (shown as dots) and compares them to $\kappa_{trans} = 0.358$ (shown as a horizontal dashed line).

For the lower reduced frequencies $k = [0.16\ 0.24\ 0.32]$ κ is above the critical value, indicating correctly that flow reversal is characteristic for LEV detachment. For the high reduced frequency $k = 0.48$, a boundary-layer eruption is predicted as the mechanism responsible for LEV detachment. The prediction agrees in all cases with results presented in section 8.
Therefore, the detachment behavior of a set of certain dimensional parameters can be predicted, although their non-dimensional equivalents are constant. It should be mentioned, that the presented detachment prediction method might be only valid in strict limits given by low Reynolds numbers and certain airfoil kinematics.

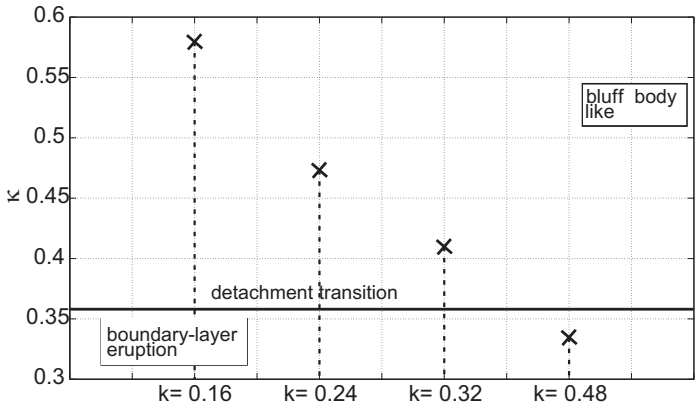

Figure 9.2: Estimated transitional conditions for the LEV detachment mechanisms at $\kappa_{trans} = 0.358$ and κ values for each set of parameters for different reduced frequencies, shown as dots. (Adapted from Widmann and Tropea (2015))

10 Conclusions

Experiments have been conducted to help understand the mechanisms leading to the detachment of a leading edge vortex from an unsteady airfoil. A covering ratio κ, describing the mass flow into the leading edge vortex during one motion period has been introduced and was conjectured to determine the LEV deatchment behavior. It consists of several non-dimensional parameters (Reynolds number Re, reduced frequency k and the shear layer to chord length ratio $a_0 c$, which have been varied in different experimental studies to identify their isolated influence on the vortex dynamics. Time resolved PIV measurements have been conducted and velocity fields have been acquired. The flow fields were analyzed using flow topology and the Finite Time Lyapunov exponent, critical points and single vortical structures were identified. The temporal circulation of leading edge vortices, trailing edge vortices and secondary vortical structures have been computed.
Two different mechanisms have been identified which can lead to LEV detachment: The first mechanism is analogous to the vortex shedding mechanism from bluff bodies, with the chord length as the characteristic length. The second mechanism is an LEV-induced eruption of the boundary layer, altering the flow topology near the leading edge, which may occur independent of the airfoil chord. A common feature of both mechanisms is the interaction of the clockwise-rotating shear layer feeding the LEV with fluid of opposite signed vorticity and the subsequent formation of a full saddle near the leading edge, which redistributes the fluid emerging from the shear layer: The growth of the primary LEV is inhibited. A transition between both mechanisms can be induced by forcing κ above or below a critical value.
The main results of the parametrical studies are summarized as follows.

1. Non-dimensional flow parameters: Usually in unsteady aerodynamics four non-dimensional parameters (Re, St, k and $\alpha_{eff}(t)$) are used to characterize the flow around an airfoil. These parameters do not take viscous effects or an interaction between the LEV and

the boundary-layer into account. Similarity of the flow fields can therefore not be expected for cases, when the LEV detaches due a boundary-layer eruption instead of a flow reversal at the trailing edge, although the conventional non-dimensional parameters have been kept constant. An additional parameter taking the vortex detachment mechanism into account has to be defined in order to explain a possible discrepancy between results of flow fields with constants non-dimensional parameters.

2. Role of the airfoil chord length: For short chord lengths and low reduced frequecies, the LEV detaches due to the flow reversal at the trailing edge. Initially, the chord length separates layers of opposite signed vorticity, analogous to bluff body vortex detachment and is therefore characteristic for LEV detachment. For an increased chord length or an increased reduced frequency, the LEV detaches due to a boundary-layer eruption. This phenomenon depends on the vortex size itself and the pressure gradient at the leading edge induced by the effective angle of attack history and thus the airfoil kinematics. The chord length is not a universal characteristic parameter for LEV detachment.

3. Secondary vortical structures: Secondary vortical structures may form near the leading edge independent of the flow reversal. The subsequently altered flow topology can lead to LEV detachment due to a boundary-layer eruption. The occurrence of these structures is caused by a viscous/inviscid interaction between the boundary layer on the airfoil the LEV, whose state only depends on the shear layer parameters. If the LEV detaches as a result of the formation of secondary structures, it can be normalized by using the shear layer parameters instead of the chord length as a characteristic length. The Reynolds number and the pressure gradient at the leading edge determine, whether the boundary layer separates and secondary structures subsequently form, before the bluff body mechanism initiates LEV detachment.

4. Airfoil kinematics: The airfoil kinematics determine the relationship between the LEV state and the angle of attack history, which determines the pressure gradient at the leading edge. Altering the reduced frequency results in a shift between both time scales. Therefore at

high reduced frequencies a boundary-layer eruption is provoked and the maximal achievable LEV circulation decreased. The airfoil chord length is not a characteristic length for LEV growth and detachment above a critical speed of airfoil motion. An optimal reduced frequency exists, which produces LEVs of maximal size.

5. Leading edge shape: The leading edge shapes alters the local pressure gradient on the forward-facing part of the airfoil. Although the effect on the LEV circulation and the lift history is measurable, it is only of second order, as expected. The leading edge shape determines the instant in the motion cycle, when a critical angle of attack is locally exceeded and a distinct LEV starts to form. Therefore a phase shift in the LEV evolution can be observed for different leading edge shapes. For sharp leading edges a constant shear layer curvature a_0 is expected. A variation of the leading edge shape alters the curvature and leads to a different LEV growth behavior.

6. Distinction between both LEV detachment mechanisms: Based on the statements above, it can be determined in which region of flow parameters bluff body LEV detachment and eruption caused LEV detachment can be expected. A boundary-layer separation or eruption can only be expected for low Reynolds numbers, since viscous effects are diminished for high Reynolds numbers. The influence of viscous effects, for which the the shear layer thickness is characteristic, decreases with increasing Reynolds number ($\frac{\partial \delta_{SL}}{\partial Re} \propto Re^{-1.5}$). Additionally, a boundary-layer eruption is expected for high reduced frequencies, which lead to a rising pressure gradient, before flow reversal may occur due to sufficient accumulated mass in the LEV. The LEV / chord covering ratio κ is indicative of the LEV detachment mechanism by incorporating the global flow parameters. Therefore, eruption caused LEV detachment is only expected in a region of flow parameters (high reduced frequencies and low Reynolds numbers), which are far away from the parameters observed in efficient flapping flight.

11 Outlook

The conclusions presented in section 10 are limited to a narrow set of parameters. To be able to identify distinct cause-and-effect relations, the experiments were knowingly carried out under simplified conditions: the flow was two-dimensional, the angle of attack histories were held constant and one-shot airfoil kinematics were used, neglecting periodic variations of the boundary layer due to cyclic motions. These conclusion need to be transferred to more realistic conditions: A periodic motion, three-dimensional flow fields including wing tip effects and altered airfoil kinematics need to be investigated in the future. The covering ratio κ needs to be checked for validity in a larger parametric space. Especially the influence of the shear layer growth, the airfoil kinematics and the maximal angle of attack on the critical value κ_{trans} for which a transition in the LEV detachment mechanisms needs to be determined. Since the shear layer parameters are supposed to be characteristic for eruption caused LEV detachment and these parameters are only accessible by certain assumptions, their evolution has to be measured and linked to the primary LEV growth. Additionally, measuring the flow field around the stagnation point region can provide more detailed information about the shear layer development and its role during LEV detachment.

To test the hypothesis that the secondary structures lead to LEV detachment, a manipulation of the LEV evolution history could be executed. If the boundary-layer separation below the LEV can be suppressed and the formation of the secondary structures be delayed to later stages in the stroke cycle, then the LEV can grow for a longer period and accumulate larger amounts of circulation. A DBD plasma-actuator is pre-destined to prevent the formation of a half-saddle leading to boundary-layer separation, since it should be able to change the global flow field by locally adding a small body force. If its ability for suppressing the secondary structures is proven, it could be coupled to sensors and an active control algorithm to increase the LEV induced high lift for arbitrary flight maneuvers instead of simplified one-shot kinematics.

Bibliography

Y. D. Afanasyev. Formation of vortex dipoles. *Physics of Fluids*, 18:037103, 2006.

J. M. Anderson, K. Streitlien, D. S. Barrett, and M. S. Triantafyllou. Oscillating foils of high propulsive efficiency. *Journal of Fluid Mechanics*, 360:41–72, 1998.

A. Azuma and T. Watanabe. Flight performance of a dragonfly. *Journal of Experimental Biology*, 137:221–252, 1988.

Y. S. Baik, L. P. Bernal, K. Granlund, and M. V. Ol. Unsteady force generation and vortex dynamics of pitching and plunging aerofoils. *Journal of Fluid Mechanics*, 709:1–32, 2012.

J. Bentley and J. Mudd. Vortex shedding mechanisms in single and dual bluff bodies. *Flow Measurement and Instrumentation*, 14:23–31, 2003.

A. Betz. Wie entsteht ein Wirbel in einer wenig zähen Flüssigkeit? *Die Naturwissenschaften*, 37:193–196, 1950.

E. Buckingham. On physically similar systems; illustrations of the use of dimensional equations. *Physical Review*, 4:345–376, 1914.

L. W. Carr. Progress in analysis and prediction of dynamic stall. *Journal of aircraft*, 25 (1):6–17, 1988.

L. W. Carr, K. McAlister, and W. McCroskey. Analysis of the development of dynamic stall based on oscillating airfoil experiments. Technical report, NASATechnicalNoteD-8382., 1977.

T. Cebeci, M. Platzer, H. Chen, K.-C. Chang, and S. J. P. *Analysis of Low-Speed Unsteady Airfoil Flows*. Springer, 2004.

M. S. Chong, A. E. Perry, and B. J. Cantwell. A general classification of three-dimensional flow fields. *Physics of Fluids A: Fluid Dynamics (1989-1993)*, 2:765–777, 1990.

J. O. Dabiri. Optimal vortex formation as a unifying principle in biological propulsion. *Annual Review of Fluid Mechanics*, 41:17–33, 2009.

J. O. Dabiri and M. Gharib. Starting flow through nozzles with temporally variable exit diameter. *Journal of Fluid Mechanics*, 538:111–136, 2005.

S. T. Davids. A computational and experimental investigation of a flutter generator. Master's thesis, United States Naval Postgraduate School, Monterey, California, 1999.

S. Depardon, J. J. Lasserre, L. E. Brizzi, and J. Boree. Instantaneous skin-friction pattern analysis using automated critical point detection on near-wall piv data. *Measurement Science and Technology*, 17:1659–1669, 2006.

A. C. DeVoria and M. J. Ringuette. Vortex formation and saturation for low-aspect-ratio rotating flat-plate fins. *Experiments in Fluids*, 52:441–462, 2012.

M. H. Dickinson and K. G. Götz. Unsteady performance of model wings at low reynolds-number. *Journal of Experimental Biology*, 174:45–64, 1993.

N. Didden. On the formation of vortex rings: Rolling-up and production of circulation. *Journal of Applied Mathematics and Physics*, 30:101–115, 1979.

T. L. Doligalski, C. R. Smith, and J. D. Walker. Vortex interactions with walls. *Annual Review of Fluid Mechanics*, 26:573–616, 1994.

F. Domenichini. Three-dimensional impulsive vortex formation from slender orifices. *Journal of Fluid Mechanics*, 666:506–520, 2011.

C. P. Ellington, C. van den Berg, A. P. Willmott, and T. A. L. R. Leading-edge vortices in insect flight. *Nature*, 384 (6610):626–630, 1996.

A. Fage and F. C. Johansen. Xlii. the structure of vortex sheets. *The London, Edinburgh, and Dublin Philosophical Magazine and Journal of Science*, 5:417–441, 1928.

H. G. Flegg. *From Geometry to Topology*. Dover Publications, 2001.

J. F. Foss. Surface selections and topological constraint evaluations for flow field analyses. *Experiments in Fluids*, 37:883–898, 2004.

C. P. Gendrich. *Dynamic stall of rapidly pitching airfoils: MTV experiments and Navier-Stokes simulations*. PhD thesis, Michigan State University, 1999.

J. H. Gerrard. The mechanics of the formation region of vortices behind bluff bodies. *Journal of Fluid Mechanics*, 25:401–413, 1966.

M. Gharib, E. Rambod, and K. Shariff. A universal time scale for vortex ring formation. *Journal of Fluid Mechanics*, 360:121–140, 1998.

L. Graftieaux, M. Michard, and N. Grosjean. Combining piv, pod and vortex identification algorithms for the study of unsteady turbulent swirling flows. *Measurement Science and Technology*, 12:1422–1429, 2001.

I. Gursul. Unsteady aspects of leading-edge vortices. Technical report, NATO RTO-TR-AVT-080, 2012.

I. Gursul, R. Gordnier, and M. Visbal. Unsteady aerodynamics of nonslender delta wings. *Progress in Aerospace Sciences*, 41:515–557, 2005.

G. Haller. Lagrangian coherent structures from approximate velocity data. *Physics of Fl*, 14:1851–1861, 2002.

J. L. Helman and L. Hesselink. Visualizing vector field topology in fluid flows. *IEEE Computer Graphics and Applications*, 11:36–46, 1991.

R. F. Huang, W. J. Y., J. H. Jeng, and R. C. Chen. Surface flow and vortex shedding of an impulsively started wing. *Journal of Fluid Mechanics*, 441:265 – 292, 2001.

J. Hunt, A. Wray, and P. Moin. Eddies, stream, and convergence zones in turbulent flows. Technical report, Center for Turbulence Research Report CTR-S88, pp. 193–208, 1988.

J. C. R. Hunt, C. J. Abell, J. A. Peterka, and H. Woo. Kinematical studies of the flows around free or surface-mounted obstacles; applying topology to flow visualization. *Journal of Fluid Mechanics*, 86:179–200, 1978.

J. Jeong and F. Hussain. On the identification of a vortex. *Journal of Fluid Mechanics*, 285:69–94, 1995.

A. R. Jones and H. Babinsky. Unsteady lift generation on rotating wings at low reynolds numbers. *Journal of Aircraft*, 47:1013–1021, 2010.

A. R. Jones and H. Babinsky. Reynolds number effects on leading edge vortex development on a waving wing. *Experiments in Fluids*, 51:197–210, 2011.

K. D. Jones and M. F. Platzer. Flapping wing propulsion for a micro air vehicle. In *38th Aerospace Sciences Meeting & Exhibit 10 - 13 January 2000 / Reno, NV*, 2001.

H. Kaden. Aufwicklung einer unstabilen Unstetigkeitsfläche. *Ingenieur Archiv*, 2:140–168, 1931.

J. Katz and A. Plotkin. *Low-Speed Aerodynamcs*. McGraw-Hill, 1991.

T. Kinsey and G. Dumas. Parametric ststudy an oscillating airfoil in a power extraction regime. *AIAA*, 46:1318–1330, 2008.

V. Kolar. Brief notes on vortex identification. In *Proceedings of the 8th WSEAS international conference on fluid mechanics, 8th WSEAS international conference on Heat and mass transfer. World Scientific and Engineering Academy and Society (WSEAS)*, 2011.

C. P. Kothandaraman and S. Subramanyan. *Heat and Mass Transfer Data Book*. New Age International, 2007.

J. Larsen, S. Nielsen, and S. Krenk. Dynamic stall model for wind turbine airfoils. *Journal of Fluids and Structures*, 23:959–982, 2007.

J. G. Leishman. Dynamic stall experiments on the naca 23012 aerofoil. *Experiments in Fluids*, 9:49–58, 1990.

J. G. Leishman. *Principles of Helicopter Aerodynamics*. Cambridge University Press, 2008.

J. G. Leishman and T. S. Beddoes. A semi-empirical model for dynamic stall. *Journal of the American Helicopter Society*, 34:3–17, 1989.

P. B. S. Lissaman. Low-Reynolds-number airfoils. *Annual Review of Fluid Mechanics*, 15:223–239, 1983.

R. L. Maltby. The development of the slender delta concept. *Aircraft Engineering and Aerospace Technology*, 40:12–17, 1968.

C. Maresca, D. Favier, and J. Rebont. Experiments on an aerofoil at high angle of incidence in longitudinal oscillations. *Journal of Fluid Mechanics*, 92:671–690, 1979.

W. J. Maybury and F.-O. Lehmann. The fluid dynamics of flight control by kinematic phase lag variation between two robotic insect wings. *Journal of Experimental Biology*, 207:4707–47026, 2004.

W. J. McCroskey. Unsteady airfoils. *Annual Review of Fluid Mechanics*, 14:285–311, 1982.

A. Michalke. Zur instabilität und nichtlinearen entwicklung einer gestörten scherschicht. *Ingenieur-Archiv*, 33:264–276, 1964.

M. Milano and M. Gharib. Uncovering the physics of flapping flat plates with artificial evolution. *Journal of Fluid Mechanics*, 534:403–409, 2005.

D. W. Moore. The rolling up of a semi-infinite vortex sheet. *Proceedings of the Royal Society A*, 345:417–430, 1975.

R. L. Nudds, G. K. Taylor, and A. L. R. Thomas. Tuning of strouhal number for high propulsive efficiency accurately predictes how wingbeat frequency and stroke amplitude relate and scale with size and flight speed in birds. *Proceedings of the Royal Society B*, 271:2071–2076, 2004.

M. V. Ol, L. P. Bernal, C.-K. Kang, and W. Shyy. Shallow and deep dynamic stall for flapping low reynolds number airfoils. *Experiments in Fluids*, 46:883–901, 2009.

G. Pedrizzetti. Vortex formation out of two-dimensional orifices. *Journal of Fluid Mechanics*, 655:198–216, 2010.

A. E. Perry and M. S. Chong. A description of eddying motions and flow patterns using critical-point concepts. *Annual Review of Fluid Mechanics*, 19:125–155, 1987.

A. E. Perry and M. S. Chong. Topology of flow patterns in vortex motions and turbulence. *Applied Scientific Research*, 53:357–374, 1994.

A. E. Perry and M. S. Chong. *Flow Visualization: Techniques and Examples*, chapter Interpretation of flow visualization, pages 1–26. Imperial College Press, 2000.

M. Platzer, K. D. Jones, J. Young, and J. C. S. Lai. Flapping-wing aerodynamics: Progress and challenges. *AIAA*, 46:2136–2149, 2008.

E. C. Polhamus. A concept of the vortex lift of sharp-edge delta wings based on a leading-edge-suction analogy. Technical report, NASA, 1966.

E. C. Polhamus. Predictions of vortex-lift characteristics by a leading-edge suction analogy. *Journal of Aircraft*, 8:193–199, 1971.

L. Prandtl. Die entstehung von wirbeln in einer flüssigkeit kleinster reibung. *Zeitschrift fuer Flugtechnik und Motorluftschiffahrt*, 18 (21):489 – 496, 1927.

T. Prangemeier, D. E. Rival, and C. Tropea. The manipulation of trailing-edge vortices for an airfoil in plunging motion. *Journal of Fluids and Structures*, 26:193–204, 2010.

M. Raffel, C. E. Willert, S. T. Wereley, and J. Kompenhans. *Particle Image Velocimetry*. Springer, 2007.

K. Ramesh, A. Gopalarathnam, K. Granlunad, M. V. Ol, and J. R. Edwards. Discrete-votex method with novel shedding criterion for unsteady aerofoil flows with inermittent leading-edge vortex shedding. *Journal of Fluid Mechanics*, 751:500–538, 2014.

D. Read, F. Hover, and M. Triantafyllou. Forces on oscillating foils for propulsion and maneuvering. *Journal of Fluid Mechanics*, 17:163–183, 2003.

A. D. Reeh. *Natural Laminar Flow Airfoil Behavior in Cruise Flight through Atmospheric Turbulence*. PhD thesis, Fachbereich Maschinenbau an der Technischen Universität Darmstadt, Fachgebiet Strömungslehre und Aerodynamik, 2014.

D. Rival, D. E.and Schönweitz and C. Tropea. Vortex interaction of tandem pitching and plunging plates: a two-dimensional model of hovering dragonfly-like flight 6.1 (2011): 016008. *Bioinspiration & biomimetics*, 6:1–13, 2011.

D. E. Rival. *Development, Control and Recovery of Leading- and Trailing-Edge Vortices in Tandem-Airfoil Configurations*. PhD thesis, Fachbereich Maschinenbau an der Technischen Universität Darmstadt, Fachgebiet Strömungslehre und Aerodynamik, 2009.

D. E. Rival and C. Tropea. Characteristics of pitching and plunging airfoils under dynamic-stall conditions. *Journal of Aircraft*, 47:80–86, 2010.

D. E. Rival, T. Prangemeier, and C. Tropea. The influence of airfoil kinematics on the formation of leading-edge vortices in bio-inspired flight. *Experiments in Fluids*, 46:823–833, 2008.

D. E. Rival, R. Manejev, and C. Tropea. Measurement of parallel blade-vortex interaction at low reynolds numbers. *Experiments in Fluids*, 49: 89–99, 2010.

D. E. Rival, J. Kriegseis, P. Schaub, A. Widmann, and C. Tropea. A criterion for vortex separation on unsteady aerodynamic profiles. In *51st AIAA Aerospace Sciences Meeting, AIAA, Grapevine, TX, AIAA Paper. Vol. 836*, 2013.

D. E. Rival, J. Kriegseis, P. Schaub, A. Widmann, and C. Tropea. Characteristic length scales for vortex detachment on plunging profiles with varying leading-edge geometry. *Experiments in Fluids*, 55:1–8, 2014.

A. Roshko. On the drag and shedding frequency of two-dimensional bluff bodies - technical note 3169. Technical report, National Advisory Committee for Aeronautics, 1954.

T. Ruiz, J. Borée, T. Tran, C. Sicot, and L. E. Brizzi. Finite time lagrangian analysis of an unsteady separation induced by a near wall wake. *Physics of Fluids*, 22:1–8, 2010.

S. Sarkar and K. Venkatraman. Influence of pitching angle of incidence on the dynamic stall behavior of a symmetric airfoil. *European Journal of Mechanics B/Fluids*, 27:219–238, 2008.

P. Sattari, D. E. Rival, R. J. Martinuzzi, and C. Tropea. Growth and separation of a start-up vortex from a two-dimensional shear layer. *Physics of Fluids*, 24:1–14, 2012.

H. Schlichting and K. Gersten. *Boundary Layer Theory*. Springer, 2001.

S. C. Shadden, F. Lekien, and J. E. Marsden. Definition and properties of lagrangian coherent structures from finite-time lyapunov exponents in two-dimensional aperiodic flows. *Physica D: Nonlinear Phenomena*, 212.3:271–304, 2005.

M. Shusser, M. Rosenfeld, J. Dabiri, and M. Gharib. Effect of time-dependent piston velocity program on vortex ring formation in a piston/cylinder arrangement. *Physics of Fluids*, 18:033601, 2006.

W. Shyy, Y. Lian, J. Tang, D. Viieru, and H. Liu. *Aerodynamics of Low Reynolds Number Flyers*. Cambridge University Press, 2008.

W. Shyy, H. Aono, S. K. Chimakurthi, P. Trizila, C.-K. Kang, C. E. S. Cesnik, and H. Liu. Recent progress in flapping wing aerodynamics and aeroelasticity. *Progress in Aerospace Sciences*, 46:284–327, 2010.

G. K. Taylor, R. L. Nudds, and T. A. L. R. Flying and swimming animals cruise at a strouhal number tuned for high power efficiency. *Nature*, 425: 707–711, 2003.

M. S. Triantafyllou, A. H. Techet, and F. S. Hover. Review of experimental work in biomimetic foils. *IEEE Journal of Oceanic Engineering*, 29 (3): 585–594, 2004.

C. Tropea, A. L. Yarin, and J. F. Foss, editors. *Springer Handbook of Experimental Fluid Mechanics*. Springer, 2007.

R. D. Whalley and K.-S. Choi. The starting vortex in quiescent air induced by dielectric-barrier-discharge plasma. *Journal of Fluid Mechanics*, 703: 192–203, 2012.

A. Widmann and C. Tropea. Parameters influencing vortex growth and detachment on unsteady aerodynamic profiles. *Journal of Fluid Mechanics*, 773:432–459, 2015.

C. H. K. Williamson. Vortex dynamics in the cylinder wake. *Annual Review of Fluid Mechanics*, 28:477–539, 1996.

J.-Z. Wu, H.-Y. Ma, and M.-D. Zhou. *Vorticity and Vortex Dynamics*. Springer, 2006.

S. Yarusevych, P. E. Sullivan, and J. G. Kawall. On vortex shedding from an airfoil in low-reynolds-number flows. *Journal of Fluid Mechanics*, 632: 245–271, 2009.

J. Young, J. C. S. Lai, and M. F. Platzer. A review of progress and challenges in flapping foil power generation. *Progress in Aerospace Sciences*, 67:2–28, 2014.